

Copyright Undertaking

This thesis is protected by copyright, with all rights reserved.

By reading and using the thesis, the reader understands and agrees to the following terms:

- 1. The reader will abide by the rules and legal ordinances governing copyright regarding the use of the thesis.
- 2. The reader will use the thesis for the purpose of research or private study only and not for distribution or further reproduction or any other purpose.
- 3. The reader agrees to indemnify and hold the University harmless from and against any loss, damage, cost, liability or expenses arising from copyright infringement or unauthorized usage.

IMPORTANT

If you have reasons to believe that any materials in this thesis are deemed not suitable to be distributed in this form, or a copyright owner having difficulty with the material being included in our database, please contact lbsys@polyu.edu.hk providing details. The Library will look into your claim and consider taking remedial action upon receipt of the written requests.

SYNTHESIS AND STABILIZATION OF 1T' PHASE TRANSITION METAL DICHALCOGENIDES AND HYDROGEN EVOLUTION REACTION ELECTROCATALYST APPLICATION

ZONGLIANG GUO

PhD

The Hong Kong Polytechnic University

2025

The Hong Kong Polytechnic University

Department of Applied Physics

Synthesis and Stabilization of 1T' Phase Transition

Metal Dichalcogenides and Hydrogen Evolution Reaction

Electrocatalyst Application

ZONGLIANG GUO

A thesis submitted in partial fulfillment of the requirements for the degree of Doctor of Philosophy

Certificate of originality

I hereby declare that this thesis is my own work and that, to the best of my knowledge
and belief, it reproduces no material previously published or written, nor material that has
been accepted for the award of any other degree or diploma, except where due
acknowledgement has been made in the text.
(Signature)
Zongliang Guo (Name of candidate)



Abstract

Research on transition metal dichalcogenides (TMDs) has gained significant attention in recent years, especially Group VI TMDs. The van der Waals gap, which lacks bonding between layers, provides opportunities for homo- or hetero-structure engineering by stacking in specific manners. Moreover, the multiple phases of TMDs represent various distinct structures and unique properties. While the well-known 2H phase is thermodynamically stable, the 1T' phase of TMDs often exhibits remarkable and distinct properties. However, many TMDs in the 1T' phase are metastable, which limits their practical applications and reliability. For example, 1T'-phase MoS₂, one of the most extensively studied TMDs, gradually transforms into the 2H phase over several months or instantly when exposed to temperatures above 97 °C. This critical drawback has greatly hindered the applications of 1T' TMDs, as it leads to performance degeneration and low phase purity in synthesis process. In addition to the inherent disadvantage originating from metastable 1T' phase structure, the synthesis of phase-pure 1T' TMDs remains a huge challenge due to the low stability. Therefore, there is a pressing need for a technique to prepare 1T' TMDs with high phase purity and stabilize them.

This thesis introduces a simple, mass-production-capable method for directly synthesizing 1T' **TMDs** with alkali chalcogenides phase-pure metal intercalation. The alkali-metal-chalcogenide-intercalated 1T' TMDs have been directly grown at carefully controlled temperature, employing a proposed self-intercalation method which involves a strategy of utilizing the structure similarity between intercalated 1T' TMDs and alkali metal molybdate. Experimental characterizations have confirmed that the as-synthesized 1T' TMDs possessed nearly 100 % 1T' phase purity and high crystal quality. This method only requires cheap precursors and a simple tube furnace with few-hour process, making this



technique available for mass production. Moreover, various TMDs with multiple kinds of alkali metal chalcogenides intercalation have been successfully synthesized via this self-intercalation method, confirming the versatility of this technique.

Notably, this is the first demonstration of stabilizing the 1T' phase of TMDs through alkali metal chalcogenide intercalation. This method provides stability against high temperature (750 °C) and aging exposed to air for more than one year. The intercalated 1T' MoS2 represents stability against strong acid and usual solvents. Thanks to this stabilization and advanced synthesis process, the synthesized MoS2 is 1T' phase pure, avoiding the phase mixture issues common in other synthesis methods. The stabilization mechanism was investigated through theoretical calculations. It has been found that K2S intercalation reduces the formation energy of 1T' MoS2, making it stable without altering the in-plane structure. The calculation results indicate that the N-doping and bonding formation in interlayer are two significant reasons for lowered formation energy.

The 1T' MoS₂ possess hydrogen evolution reaction (HER) electrocatalytically active sites at edge sites and basal planes, while 2H phase only has active sites at edge. Enhancing performance of 2H-MoS₂-based HER electrocatalysts typically requires doping or exposing more edge sites. However, employing 1T' MoS₂ would inherently and significantly increases the active sites density for HER electrocatalysis, making it promising candidate for HER electrocatalytic application. The K₂S-intercalated 1T' MoS₂, prepared by proposed self-intercalation method, exhibits excellent HER electrocatalytic performance, with a Tafel slope of 39.3 mV/dec and an overpotential of -73 mV at 10 mA/cm². It also demonstrates exceptional HER long-term stability, maintaining performance at 50 mA/cm² for 1000 hours and enduring 30000 cycles, outperforming many other TMD-based electrocatalysts.

Self-intercalation method demonstrated in this thesis has proven versatile, enabling the synthesis of various 1T' TMDs and fostering the exploration of their novel properties and



the development of new applications. By eliminating the major disadvantage of the 1T' phase's instability, this synthesis and stabilization method opens up new avenues for the use of 1T' TMDs in various advanced technologies.



List of Publications

Journal Publications Related to Thesis

1. **Z. L. Guo**, H. Cheng, M. Yang, C. H. Wong, T. I. Alam, S. P. Lau, Y. H. Tsang*, "Phase-pure 1T' Molybdenum Disulfide Synthesis and Stabilization" (ready for submission)

Other Collaborative Journal Publications:

- M. Saleque, S. Ahmed, M. N. A. Ivan, M. I. Hossain, W. Qarony, P. K. Cheng, J. P. Qiao, Z. L. Guo, L. H. Zeng, Y. H. Tsang, "High-temperature solar steam generation by MWCNT-HfTe₂ van der Waals heterostructure for low-cost sterilization", *Nano Energy* 2022, 94, 13, 106916.
- S. Ahmed, P. K. Cheng, J. P. Qiao, W. Gao, A. M. Saleque, M. N. A. Ivan, T. Wang, T. I. Alam, S. U. Hani, <u>Z. L. Guo</u>, S. F. Yu, Y. H. Tsang, "Nonlinear Optical Activities in Two-Dimensional Gallium Sulfide: A Comprehensive Study", *ACS Nano* 2022, 13.
- M. N. A. Ivan, A. M. Saleque, S. Ahmed, <u>Z. L. Guo</u>, D. Zu, L. L. Xu, T. I. Alam, S. U. Hani, Y. H. Tsang, "Jute stick derived self-regenerating sustainable solar evaporators with different salt mitigation mechanisms for highly efficient solar desalination", *J. Mater. Chem. A* 2023, 11, 3961.
- 4. X. C. Huang, L. F. Deng, **Z. L. Guo**, N. Q. Luo, J. Liu, Y. Zhao, Z. Liu, A. X. Wei, "Layer-dependent electrical transport property of two-dimensional ReS₂ thin films", *J. Mater. Sci.-Mater. Electron.* **2021**, *32*, 24342.



Acknowledgments

The completion of this thesis marks the end of an enriching and transformative journey, one that would not have been possible without the support, guidance, and encouragement of many exceptional individuals. I would like to express my deepest gratitude to everyone who has played a part in my academic and personal growth during this time.

First and foremost, I am profoundly grateful to my supervisor, Professor TSANG Yuen Hong, for his invaluable mentorship and constant support throughout my research. I truly appreciate the freedom he gave me to explore my ideas, combined with his thoughtful feedback that kept me on track. His dedication to both my progress and the quality of my work has been instrumental in shaping this thesis.

I would also like to extend my sincere thanks to Professor LAU Shu Ping and Dr. YANG Ming, whose insights and suggestions were critical in refining my research. Their expertise in the field and willingness to offer guidance made a significant impact on my work and understanding of the subject matter.

My heartfelt gratitude goes to my colleagues and research team members, particularly Mr. Tawsif Ibne Alam and Dr. Cheng Ping Kwong. I am fortunate to have worked alongside such a talented and supportive group of individuals. The intellectual discussions, collaborative efforts, and shared experiences have greatly enriched my research and made the journey enjoyable. And I am grateful for their support.

Special thanks are due to Dr. WONG Hon Fai, who provided essential technical and logistical support, ensuring that all aspects of the research ran smoothly. Their hard work behind the scenes has been invaluable to the success of this project.

Lastly, I want to express my deepest appreciation to my family. Thank you for your unwavering love and encouragement. Your belief in me has been a constant source of motivation. To my parents, your understanding, patience, and support have made all the



difference. Your presence has kept me grounded and focused, and I am truly grateful to have you by my side.

This thesis is as much a reflection of the collective effort and support I have received as it is a result of my own work. I am truly blessed to have such an incredible network of people who have contributed to this achievement in countless ways. To all of you, I extend my heartfelt thanks.



Table of Contents

Certificate of originality	•••••
Abstract	I
List of Publications	IV
Acknowledgments	V
Table of Contents	VII
List of Figures	XI
List of Tables	XVII
List of Symbols and Acronyms	XVIII
Chapter 1	1
Introduction	1
1.1 Background	2
1.2 Significance of Study	6
1.2.1 Synthesis of 1T' TMDs	6
1.2.2 Stabilization of 1T' TMDs	8
1.2.3 Stabilized K ₂ S-intercalated 1T' MoS ₂ Used as Hydrogen	n Evolution Reaction
Electrocatalyst	9
1.3 Accomplished Milestones	11
1.4 Thesis Outline	12
Chapter 2	15
Fundamentals	15
2.1 Introduction	16
2.2 Structure of Transition Metal Dichalcogenides	17
2.3 Important Characterization Methods	21



2.4 Properties and Applications	24
2.5 1T' TMDs Preparation Methods	31
2.5.1 Preparation through Phase Transition	32
2.5.2 Direct Synthesis Methods	35
2.6 Intercalation, Self-intercalation, and Stabilization	36
2.6.1 Intercalation methods	38
2.6.2 Intercalation and Stabilization	41
2.7 Summary	44
Chapter 3	45
Synthesis of Intercalated Phase-pure 1T' Transition Metal Dichalcog	genides by
Self-intercalation Method	45
3.1 Introduction	46
3.2 Characterization Equipment	48
3.3 Synthesis and Characterization of K ₂ S-intercalated 1T' MoS ₂	48
3.3.1 Synthesis Process	48
3.3.2 Characterization Results	50
3.4 Synthesis and Characterization of Na ₂ S, Li ₂ S-intercalated 1T' MoS ₂	59
3.4.1 Synthesis Process	59
3.4.2 Characterization Results	61
3.5 Synthesis and Characterization of Na ₂ Se, K ₂ Se-intercalated 1T' MoSe ₂	65
3.5.1 Synthesis Process	65
3.5.2 Characterization Results	66
3.6 Synthesis and Characterization of K ₂ Te-intercalated 1T' MoTe ₂	68
3.6.1 Synthesis Process	68
3.6.2 Characterization Results	68
3.7 Self-intercalation Method	70



3.8 Summary	74
Chapter 4	76
Stability and Stabilization Mechanism	76
4.1 Introduction	77
4.2 Stability	78
4.2.1 Temperature	78
4.2.2 Solvents and aging in air	79
4.2.3 Thickness	81
4.3 Theoretical calculation	84
4.4 Summary	90
Chapter 5	92
Durable K2S-intercalated 1T' MoS2 Electrocatalyst for Efficient Hydrogen	Evolution
Reaction	92
5.1 Introduction	93
5.2 K ₂ S-intercalated 1T' MoS ₂ HER Catalysts Preparation and Setup	94
5.3 HER Performance	99
5.4 Summary	108
Chapter 6	110
Summary and Future Works	110
6.1 Introduction错误!未	定义书签。
6.2 Summary	112
6.2.1 Self-intercalation Method	112
6.2.2 Stabilization by Self-intercalation	112
6.2.3 Durable K ₂ S-intercalated 1T' MoS ₂ Electrocatalyst for Efficient	t Hydrogen
Evolution Reaction.	113
6.3 Future Works	114



References	110
	11



List of Figures

Figure 2.1: Atomic structure of 1H, 2H _a , 2H _c , and 3R phase. ¹⁹
Figure 2.2: The atomic structure of 1T phase of TMDs. ¹⁹
Figure 2.3: Schematic illustration of structures of 2H-WS ₂ and 1T' WS ₂ . ²⁰ 20
Figure 2.4: XPS Mo 3d spectra of 1T'-MoS ₂ (with 2H phase impurity) and 2H-MoS ₂ . ³⁵ 22
Figure 2.5: Simulated HAADF STEM images of ideal (a) 2H and (b) 1T phases. The bright
spots correspond to Mo atoms. In the 2H phase, S atoms are visible as less bright spots. ⁵⁶ 24
Figure 2.6: Theoretically and experimentally determined band structures of (a) 1H, (b) 1T,
and (c) 1T'-phase monolayer-MoS ₂ . ¹
Figure 2.7: Schematic of the topological field effect transistor. ⁵⁷ 30
Figure 2.8: Concentration and process time required for phase transition from 2H to 1T'
phase for different thickness. ²⁷
Figure 2.9: Energy difference between 2H-phase MoS ₂ and 1T'-phase MoS ₂ as a function of
electron concentration within monolayer or bilayer. ⁸¹
Figure 3.1: Schematic of K ₂ S-intercalated 1T' MoS ₂ synthesis setup49
Figure 3.2: Characterization of K ₂ S-intercalated 1T' MoS ₂ powder and Na ₂ S-intercalated
1T' MoS ₂ nanosheets. (a) Optical and (b) SEM images of K ₂ S-intercalated 1T' MoS ₂ powder,
respectively. Inset of (a), Photo of K ₂ S-intercalated 1T' MoS ₂ powder on the sapphire
substrate51



Figure 3.3: (a) Raman spectra of K ₂ S-intercalated 1T' MoS ₂ powder and 1T' MoS ₂ obtained
by n-butyllithium treatment. XRD results of (b) as-synthesized and (c) fully stirred
K ₂ S-intercalated 1T' MoS ₂ powder, respectively
Figure 3.4: Lattice model of K ₂ S-intercalated 1T' MoS ₂ . Lattice constant <i>a</i> , <i>b</i> , <i>c</i> is along the
direction of x, y, z axis, respectively
direction of x, y, z axis, respectively.
Figure 3.5: Experimental and fitted XPS (a) Mo 3d and S 2s, (b) K 2p, and (c) S 2p spectra of
K ₂ S-intercalated 1T' MoS ₂ powder, respectively
Figure 3.6: Another three XPS results of K ₂ S-intercalted 1T' MoS ₂ in random sampling55
Figure 3.7: TEM characterization of K ₂ S-intercalated 1T' MoS ₂ . (a) TEM and (b) HRTEM
images of K ₂ S-intercalated 1T' MoS ₂ , respectively. (c) Fast Fourier transform (FFT) filtered
images of (b). Inset of (c), FFT pattern of (b). (d) SAED pattern of K ₂ S-intercalated 1T'
MoS ₂ 56
Figure 3.8: (a) Dark-field STEM image of K ₂ S-intercalated 1T' MoS ₂ . (b-d) Elemental
mapping images of Mo, S, and K, respectively, acquired from pink rectangular box in a57
Figure 3.9: In-plane lattice structure of 1T' MoS ₂ showing distinct Mo zigzag chains58
Figure 3.10: (a) High-resolution cross-sectional TEM image. (b) Brightness profile along the
white line in a
Figure 3.11: HAADF-STEM image and EDS mapping of Mo, S, and K
Figure 3.12: An additional SAED test result of K ₂ S-intercalated 1T' MoS ₂ . (a) TEM image
of a piece of K ₂ S-intercalated 1T' MoS ₂ flake. (b) SAED pattern acquired from red circle area
shown in a
Figure 3.13: Raman spectrum of Na ₂ S-intercalated MoS ₂
Figure 3.14: Raman spectrum of Li ₂ S-intercalated MoS ₂ .



Figure 3.15: TEM characterization of Na ₂ S-intercalated 1T' MoS ₂ . (a) TEM and (b)
HRTEM images of Na ₂ S-intercalated 1T' MoS ₂ , respectively. Inset in b: SAED pattern of
Na ₂ S-intercalated 1T' MoS ₂ . (c) FFT filtered images of b. (d) Dark-field STEM image of
Na ₂ S-intercalated 1T' MoS ₂ . Elemental mapping images of (e) Mo, (f) S, and (g) Na,
respectively, acquired from rectangular dot box in d63
Figure 3.16: XPS spectra of Na ₂ S-intercalated 1T' MoS ₂ . Experimental and fitted XPS (a)
Mo 3d and S 2s, (b) S 2p, and (c) Na 1s spectra of Na ₂ S-intercalated 1T' MoS ₂ , respectively.
Figure 3.17: (a) Optical image of Na ₂ S-intercalated 1T' MoS ₂ nanosheets. (b) AFM image of
Na ₂ S-intercalated 1T' MoS ₂ nanosheets and height profile along white dot line. (c) Raman
spectra of Na ₂ S-intercalated 1T' MoS ₂ nanosheets
Figure 3.18: Raman spectrum of K ₂ Se-intercalated MoSe ₂ . Inset: optical image of
K ₂ Se-intercalated MoSe ₂ 66
Figure 3.19: Raman spectrum of Na ₂ Se-intercalated MoSe ₂ . Inset: optical image of
Na ₂ Se-intercalated MoSe ₂ 67
Figure 3.20: TEM characterization of K ₂ Se-intercalated 1T' MoSe ₂ . (a) TEM and (b)
HRTEM images of K ₂ Se-intercalated 1T' MoSe ₂ , respectively. Inset in b: SAED pattern of
K ₂ Se-intercalated 1T' MoSe ₂ . (c) FFT filtered images of b. (d) Dark-field STEM image of
K ₂ Se-intercalated 1T' MoSe ₂ . Elemental mapping images of (e) Mo, (f) Se, and (g) K,
respectively, acquired from rectangular dot box in d
Figure 3.21: Raman spectrum of K ₂ Te-intercalated MoTe ₂ . Inset: optical image of
K ₂ Te-intercalated MoTe ₂ 69
Figure 3.22: TEM characterization of K ₂ Te-intercalated 1T' MoTe ₂ . (a) TEM and (b)
HRTEM images of K ₂ Te-intercalated 1T' MoTe ₂ , respectively. Inset in b: SAED pattern of

ZONGLIANG GUO PAGE | XIII



K ₂ Te-intercalated 1T' MoTe ₂ . (c) FFT filtered images of b. (d) Dark-field STEM image of
K ₂ Te-intercalated 1T' MoTe ₂ . Elemental mapping images of (e) Mo, (f) Te, and (g) K,
respectively, acquired from rectangular dot box in d
Figure 3.23: (a) Schematic of self-intercalation and synthesis. (b) Atomic model of
K ₂ S-intercalated 1T' MoS ₂ 72
Figure 3.24: Raman spectra of samples with growth temperature from 550 °C to 950 °C72
Figure 3.25: (a) Optical image of K ₂ S intercalated 1T' MoS ₂ transferred on gold electrodes.
(b) Output characteristic curve of K2S intercalated 1T' MoS2. (c) Transfer characteristic
curve of K ₂ S intercalated 1T' MoS ₂ 74
Figure 4.1: Thermal stability of K ₂ S-intercalated 1T' MoS ₂ . (a) TGA and DSC curves of
K ₂ S-intercalated 1T' MoS ₂ powder. (b) Raman spectra of as-synthesized K ₂ S-intercalated
1T' MoS ₂ before and after annealed at 750 °C, and 2H MoS ₂ . (c) Experimental and fitted XPS
Mo 3d and S 2s spectra of K ₂ S-intercalated 1T' MoS ₂ powder after annealing at 750 °C79
Figure 4.2: Raman spectra of as-synthesized K ₂ S-intercalated 1T' MoS ₂ , K ₂ S-intercalated
1T' MoS ₂ washed with ethanol, washed with DI water, exposed to air for one year, and 2H
MoS ₂ 80
Figure 4.3: SEM images and EDS mapping results of as-synthesized K ₂ S-intercalated 1T'
MoS ₂ and K ₂ S-intercalated 1T' MoS ₂ after washed with DI water and ethanol81
Figure 4.4: Optical image of 10-nm-thick K ₂ S-intercalated 1T' MoS ₂ flake obtained by tape
exfoliation and height profile along white dot line measured by AFM82
Figure 4.5: Raman spectra of 10-nm-thick K ₂ S-intercalated 1T' MoS ₂ flake obtained by tape
exfoliation. (a) Before 100 °C annealing. (b) After 100 °C annealing



Figure 4.6: Optical image of 34-nm-thick K ₂ S-intercalated 1T' MoS ₂ flake obtained by tape
exfoliation and height profile along white dot line measured by AFM83
Figure 4.7: Raman spectra of 34-nm-thick K ₂ S-intercalated 1T' MoS ₂ flake obtained by tape
exfoliation. (a) Before 100 °C annealing. (b) After 100 °C annealing
Figure 4.8: The K_2S -intercalated MoS_2 models. (a) $1T'-(K_2S)_{x=0.22}MoS_2$ and (b)
$2H-(K_2S)_{x=0.17}MoS_2$ models.
Figure 4.9: Isosurface plots of charge density differences for the $1T'$ - $(K_2S)_{x=0.22}MoS_2$
models. The isosurface densities for the charge accumulation region (red color) and
depletion region (bule color) are 0.15 e/Bohr ³ and 0.01 e/Bohr ³ , respectively87
Figure 4.10: Energy difference between the pristine 1T'- and 2H-MoS ₂ models as a
function of increasing electron doping concentration88
Figure 5.1: Schematic of K ₂ S-intercalated 1T' MoS ₂ /carbon cloth synthesis setup95
Figure 5.2: Photo of the electrochemical setup
Figure 5.3: (a) Photo of blank carbon cloth and carbon cloth with K ₂ S-intercalated 1T' MoS ₂
grown on. (b) SEM image of K ₂ S-intercalated 1T' MoS ₂ grown on carbon cloth. (c) Zoom-in
SEM image of K ₂ S-intercalated 1T' MoS ₂ flakes grown on carbon cloth. (d) Raman spectrum
of K ₂ S-intercalated 1T' MoS ₂ grown on carbon cloth
Figure 5.4: (a) The polarization curves (iR corrected) of K ₂ S-intercalated 1T' MoS ₂ HER
electrocatalyst before and after 30000 cycles, and commercial Pt/C HER electrocatalyst. (b)
The corresponding Tafel slopes of K ₂ S-intercalated 1T' MoS ₂ and commercial Pt/C HER
electrocatalysts derived from a. (c) Overpotential vs. time curve of K2S-intercalated 1T'
MoS ₂ HER electrocatalyst with constant current density of 50 mA/cm ² . (d) Nyquist plot of
K ₂ S-intercalated 1T' MoS ₂ electrocatalyst99



Figure 5.5: SEM image of K ₂ S-intercalated 1T' MoS ₂ /CC after 30000 cycles, used as HER
electrocatalyst100
Figure 5.6: Raman spectrum of K ₂ S-intercalated 1T' MoS ₂ /CC after 30000 cycles, used as
HER electrocatalyst
Figure 5.7: Comparison with best TMDs-based HER electrocatalysts in three perspectives
(Tafel slope, overpotential, and stability). The details of all compared cases shown, including
phase purity, electrode type, literature source, are listed in Table 5.1



List of Tables

Table 4.1: Average bond length of Mo-Mo and Mo-S of MoS ₂ before and after K ₂	2S
intercalation acquired by theoretical calculation.	.86
Table 4.2: Bader charge analysis of the K ₂ S-intercalated 1T' MoS ₂ model	.89
Table 4.3: Bader charge analysis of the K2S-intercalated 2H MoS2 model.	.89
Table 5.1: The best TMDs-based HER electrocatalysts via phase engineering.	103
Table 5.2: Representative non-precious HER electrocatalysts. 1	106

ZONGLIANG GUO PAGE | XVII



List of Symbols and Acronyms

2D Two-dimensional

AFM Atomic Force Microscopy

ANN Artificial Neural Network

CC Carbon Cloth

CCD Charge-coupled Device

CTAB Cetyl-trimethylammonium Bromide

CVD Chemical Vapor Deposition

CV Cyclic Voltammetry

DFT Density Functional Theory

DSC Differential Scanning Calorimetry

EDS Energy-dispersive X-ray Spectroscopy

FFT Fast Fourier Transform

FET Field-effect Transistor

HAADF High-angle Annular Dark-field

HER Hydrogen Evolution Reaction

HRTEM High-resolution Transmission Electron Microscopy

ZONGLIANG GUO PAGE | XVIII



HMA Ammonium Heptamolybdate

LIB Lithium-ion Battery

MBE Molecular Beam Epitaxy

PDOS Partial Density of States

PL photoluminescence

PIC Photonic Integrated Circuits

QSH Quantum Spin Hall

RHE Reversible Hydrogen Electrode

RRAM Resistive Random Access Memory

SAED Selected Area Electron Diffraction

SEM Scanning Electron Microscope

SERS Surface-enhanced Raman Scattering

SPE Single Photo Emitter

TEM Transmission Electron Microscopy

TFET Topological Field-effect Transistor

TGA Thermogravimetric Analysis



TMD Transition Metal Dichalcogenide

XPS X-ray Photoelectron Spectroscopy

XRD X-ray Diffraction



Chapter 1

Introduction



1.1 Background

The exfoliation of graphene has ignited curiosity in layered materials. Among these, transition metal dichalcogenides (TMDs) form a large family of approximately 60 compounds with a layered structure, characterized by van der Waals gaps between layers, akin to graphene. Although these materials have been studied in their bulk form for over fifty years, particularly for their catalytic activity, lubricity, and superconductivity, it is only in recent years that TMDs have been successfully exfoliated into few-layer forms or synthesized with few-layer thicknesses. This breakthrough has unveiled a range of novel properties and underscored their immense potential for various applications.

Among the members of TMDs, Group VI TMDs, such as MoSe₂, MoS₂, WSe₂, and WS₂, have garnered significant attention. These materials are relatively abundant in the Earth's crust and exhibit unique properties, including mechanical flexibility, electrostatic coupling, high carrier mobility, gate tunability, and piezoelectricity. Typically, they are found in the 2H phase, which is stable in air at room temperature, making them more accessible for research and applications. The thickness-dependent properties of Group VI TMDs have drawn widespread interest in recent years. One notable discovery is the transition from an indirect bandgap to a direct bandgap, observed through the emergence of a photoluminescence (PL) peak when the material is reduced to monolayer thickness. 19 This finding opens up avenues for valley-based electronic and optoelectronic applications. Additionally, the ability to tune the bandgap by adjusting thickness positions TMDs as promising candidates for optical applications. Due to their unique optoelectronic properties, TMDs hold great potential in electronics, optoelectronics, and valleytronics. 10,15,16,20-27 Their combination of chemical stability, mechanical flexibility, and a non-zero bandgap makes them suitable for applications such as field-effect transistors (FETs) and flexible devices. Furthermore, the Mo-terminated edges of 2H MoS₂ exhibit localized metallic states that are catalytically active for the hydrogen evolution reaction (HER).²⁸ This has fueled interest in



TMD-based HER catalysts, which offer excellent performance and abundance compared to the expensive and scarce Pt-based alternatives.

With the increase of interest in TMDs materials, the metastable phases of TMDs have emerged and drawn more and more attention. For most typical Group VI TMDs, there are various phases except for thermodynamically stable 2H phase with the trigonal-prismatic coordination of transition metal atoms. 1T phase shows an octahedral coordination of the transition metal atoms, while 1T', 1T", or 1T" phases represent distorted octahedral coordination. 1T, 1T', 1T", and 1T" can be broadly defined as 1T phase. Some reports even did not strictly distinguish them. Although their structures and properties are similar in some degree, it is not suitable to lump them together. It is worthy to note that the reports about synthesis of 1T" and 1T" phases TMDs are very rare, and there are some theory predictions suggest that these structures could exist. Most reports about metastable phases of TMDs are 1T or 1T' phase. The variation of transition metal coordination leads to different d-orbital splitting, which greatly affects the band structure of TMDs and their properties. 1T phases (including octahedral or distorted octahedral coordination) usually features metallic or semi-metallic behaviors, while 2H phase often is semiconducting. The various electronic behaviors (including metallic, semi-metallic, or semiconducting) are the results of different transition metal atoms coordination. It is interesting that quite a lot of TMDs family members represent several phases with distinct properties sparking widespread interests to synthesize and study metastable phases which are rarely known.

The basal planes of 1T' MoS₂ as well as edge sites have been found electrocatalytically active, which significantly increases the active sites density, while 2H MoS₂ only shows active sites at edge.²⁹⁻³⁶ This enables 1T' MoS₂, possessing excellent HER performance, a promising potential to replace expensive and rare Pt-based catalysts. Several 1T' polymorphs have been identified and demonstrated over time. Among these, the 1T' phases of single-layer WSe₂ and WTe₂ have been reported as large-gap quantum spin Hall (QSH)



insulators, making them highly suitable for spintronic device applications. Notably, WSe₂ is operable even at ambient temperature, further enhancing its practicality. Their relatively high chemical stability offers a distinct advantage over other currently known large-gap QSH insulators, such as stanene³⁷⁻⁴² and two-dimensional In-Sb compounds, which can only be used in inert atmospheres⁴³. Additionally, predictions suggest that breaking of spontaneous symmetry in the undistorted metallic 1T phase could open a bandgap, leading to unique 1T" phase structure and the robust ferroelectricity.⁴⁴ This discovery could pave the way for new functionalities in electronic and spintronic applications. The metastable 1T and 1T' phases exhibit higher electrical conductivity than their semiconducting 2H counterparts, making them promising candidates for energy storage applications. As a result, the combination of their improved conductivity and large surface area makes metallic TMDs nanosheets promising materials for electrochemical double-layer capacitors application. 45-50 The metastable 1T' Group VI TMDs are also considered highly suitable for biosensor applications, such as the indirect enzymatic detection of fenitrothion. The biosensor, using these metastable TMDs as a conductive platform, demonstrated excellent linearity across a wide concentration range and a very low detection limit.⁵¹ Additionally, molecular detection based on surface-enhanced Raman scattering (SERS) has been successfully developed using 1T' MoTe₂ and WTe₂.⁵² The metastable phases of TMDs also show significant potential in electronic applications. For example, the high conductivity of 1T' MoS₂ has been leveraged to construct 2H/1T' homojunctions, which effectively reduce contact resistance and lead to improved performance of field-effect transistors.⁵³⁻⁵⁸ Moreover, there is prediction indicating that the 1T' monolayer TMDs could exhibit anisotropic transport characteristics, which is also confirmed in 1T' MoS₂ by experiments⁵⁹. This anisotropic conductance makes 1T' MoS₂ an excellent candidate for synaptic devices application. Interestingly, it has been found that the 1T' MoTe₂ has a superconducting phase transition at 8.2 K under the pressure as high as 11.8 GPa. 60 This suggests that the metallic or semi-metallic 1T phase TMDs are possibly potential superconductors. Beside the



applications arise from the special properties of 1T phase, the reversible phase transition between semiconducting 2H phase and conducting 1T phase has been explored for non-volatile memory devices. Recently, a resistive random access memory (RRAM) device based on few-layered MoTe₂ and W_xMo_{1-x}Te₂ with tunable high- or low-resistance states controlled by applied electric field has been demonstrated.⁶¹ The applications of 1T and 1T' phases of TMDs mentioned above provide just a brief overview, highlighting the significant potential of these unique properties for both basic research and engineering. However, the synthesis is a critical and essential step, as it is necessary to enable the detailed study and exploration of the 1T and 1T' phases of TMDs.

The synthesis of TMDs in 1T phases family (including 1T, 1T', 1T", 1T" phase, which are also generally named as 1T phases), especially Group VI TMDs, remains a huge challenge, as 1T phases usually have higher system energy and are metastable. In contrast, the 2H phase of Group VI TMDs is stable and has lowest system energy, this is also the reason why most well-known and well-studied phase is 2H phase. The stable 2H phase TMDs even can exist in Earth naturally, such as 2H MoS₂. The stable 2H phase also allows easier synthesis compared with metastable 1T phases. Therefore, the first barrier to study of metastable 1T phases TMDs is the high difficulty of synthesis. The most commonly used and historically first strategy for preparing 1T' phases is the conversion of the 2H phase. This is typically accomplished by increasing the electron density through exposure to alkali metals.⁶² While this approach has been widely used, the development of direct synthesis methods for 1T (or 1T') phases remains in its early stages of exploration. To achieve the mass application of 1T' TMDs, not only the synthesis, but also the low-cost efficient production is required. The current preparation methods via conversion of 2H phase or direct synthesis still cannot satisfy industrial production requirements. The critical drawbacks of current preparation methodology are low phase purity and crystal quality, as well as low productivity.



1.2 Significance of Study

1.2.1 Synthesis of 1T' TMDs

TMDs have garnered considerable attention recently due to their unique layered structures and exceptional physicochemical properties, akin to graphene. The TMD family includes a diverse range of compounds, each capable of existing in multiple phases, each with distinct characteristics. 1,63-71 Among these, the thermodynamically stable 2H phase of MoS₂ is the most extensively studied. In contrast, other phases, which are generally higher in energy and less stable, tend to transition gradually into the stable phase. This phase transformation poses a significant challenge in the synthesis of high-purity, metastable-phase TMDs with superior crystal quality. 66,72-77 The 1T' phase, among the metastable phases, has attracted significant interest due to its unique electronic, optical, and electrochemical properties, which differ from those of their stable-phase counterparts. These distinct characteristics open up a wide range of potential applications, including superconductivity^{58,78-83}, device contacts⁸⁴, SERS^{52,76,85-89}, energy storage^{48,64,65,90-95}, electrochemical catalysis^{96,97}, supercapacitors⁴⁵, and synaptic transistors⁹⁸⁻¹⁰⁶. To fully harness these promising applications, it is essential to synthesize metastable-phase TMDs with high phase purity and achieve stabilization. Phase transitions in group VI TMDs from the stable 2H phase to the 1T or 1T' phases have been achieved through methods such as chemical treatment 107, electrostatic gating¹⁰⁸, and mechanical strain¹⁰⁹. However, these approaches often result in low phase purities up to around 80%, which can compromise performance. Additionally, the conditions required for these methods are often too stringent for large-scale production. Alternatively, direct synthesis of metastable-phase TMDs via colloidal reactions 110,111 and solvothermal processes^{112,113} has also been investigated. Unfortunately, these techniques also face challenges related to low phase purity and suboptimal crystal quality. A recently reported approach involves the chemical oxidation of alkali atom-intercalated TMDs, which



have a structure similar to the stable 2H phase¹¹⁴, to produce the 1T or 1T' phases of group VI TMDs. These alkali-intercalated TMDs are mainly synthesized by annealing A₂MS₄ compounds (where A = Na or K, and M = Mo or W) in hydrogen at 850 °C^{62,115}, or by reacting A₂S, MS₂, and M (where A = Li, Na, or K, and M = Mo, Nb, Ta, or Ti) at 800 °C¹¹⁶. This method can achieve around 90% phase purity, but the resulting chemical processes often introduce crystal defects. Additionally, 1T or 1T' phase TMDs are not stable at room temperature and tend to revert to the more stable 2H phase^{117,118}, which limits their long-term performance. Stabilizing metastable-phase TMDs without altering their intrinsic properties continues to be a significant challenge. One approach to stabilize the 1T' phase thermodynamically is through alkali atom intercalation. However, alkali atoms are highly reactive and susceptible to oxidation in air, which can degrade the TMDs materials.^{58,119,120} To achieve high purity in the 1T' phase, a high alkali metal atom intercalation ratio is required, but this can lead to the reduction of TMDs and the formation of transition metals.¹²¹ As a result, synthesizing 1T' TMDs with both high phase purity and long-term stability remains a persistent challenge.

In this thesis, a novel self-intercalation method has been developed to synthesize and stabilize phase-pure 1T' MoS₂ with K₂S intercalation. This approach results in a material that is thermodynamically stable and inert to air, ethanol, and water. Characterization techniques such as Raman spectroscopy and transmission electron microscopy (TEM) have confirmed the high crystal quality of the 1T' phase, while X-ray photoelectron spectroscopy (XPS) has showed nearly 100% phase purity. Thermal analysis via thermogravimetric analysis (TGA), differential scanning calorimetry (DSC), and annealing tests have demonstrated exceptional thermal stability, with the material remaining stable up to 750 °C, in contrast to the intrinsic 1T' MoS₂, which transitions to the more stable 2H phase at just 97 °C¹¹⁵. The method has been further extended to produce Na₂S-intercalated 1T' MoS₂, Li₂S-intercalated 1T' MoS₂, k₂Se-intercalated 1T' MoSe₂, Na₂Se-intercalated 1T' MoSe₂, and K₂Te-intercalated 1T' MoTe₂, illustrating the versatility of this technique for



synthesizing a range of 1T' phase TMDs.

1.2.2 Stabilization of 1T' TMDs

The properties of TMDs are strongly influenced by their crystalline structure. The most well-known Group VI TMDs, such as MoSe₂, are typically thermodynamically stable in the 2H phase. Whereas, the 1T, 1T', 1T", and 1T" polymorphs represent distinct structural phases with unique properties, making them promising candidates for a wide range of applications. Despite their potential, the formation energy of these phases is higher than that of the 2H phase, which makes them metastable and prone to gradual transformation into the 2H phase. Additionally, they tend to convert to the stable 2H phase at relatively low temperatures; for example, 1T' MoS₂ undergoes a phase transition to 2H above 97 °C. This inherent metastability of the 1T' phase has been partially addressed through doping and strain engineering, but these methods often introduce defects and are not suitable for large-scale production. In contrast, stabilization via intercalation engineering has gained increasing attention, as it can reduce the system's energy while preserving the intrinsic in-plane 1T' phase structure. A molten-metal-assisted intercalation method has been proposed by Park et al. 122 to stabilize 1T' TMDs. While the intercalated 1T MoS₂ remains stable up to 350 °C, the synthesized samples exhibit low phase purity. Another approach involves directly depositing lithium on 2H MoS₂, followed by heating in hydrogen, which has resulted in the formation of LiH-intercalated 1T' MoS₂. 123 This structure has demonstrated three months of stability in air and five hours in water, but surface degradation cannot be prevented. To unlock the full potential of 1T' TMDs, it is essential to synthesize metastable-phase TMDs with high phase purity and achieve stabilization.

The stabilization of 1T' TMDs is highly sought after. The synthesis and characterization of various 1T' TMDs with alkali metal chalcogenides as intercalants have been demonstrated,



with particular emphasis on K₂S-intercalated 1T' MoS₂. The high crystal quality and phase purity of these samples have been confirmed through characterization. The stability of 1T' TMDs has garnered more attention due to its significant impact on the performance of potential applications, as many 1T' TMDs are inherently metastable. The stability of K₂S-intercalated 1T' MoS₂ under various conditions, such as temperature, solvents, thickness, and aging, has been tested. These synthesized K₂S-intercalated 1T' MoS₂ samples demonstrate excellent stability when compared to those prepared in previous studies. The as-synthesized K₂S-intercalated 1T' MoS₂ can withstand temperatures exceeding 750 °C and remains stable in air, water, and ethanol, preserving its stability even after one year of aging. The theoretical calculations have been performed using a K₂S-intercalated 1T' MoS₂ model. The results indicate that K₂S intercalation reduces the formation energy by both N-doping and forming bonds with the 1T' MoS₂ structure, thereby stabilizing the 1T' phase. The band diagram further shows that the K₂S intercalation does not alter the metallic behavior of 1T' MoS₂.

1.2.3 Stabilized K₂S-intercalated 1T' MoS₂ Used as Hydrogen Evolution Reaction Electrocatalyst

Hydrogen is considered one of the most promising clean energy sources for the future, with the potential to replace fossil fuels, which are major contributors to carbon emissions and environmental pollution. The HER is an essential manner for hydrogen production, and developing low-cost, earth-abundant, and efficient HER electrocatalysts is essential. Currently, Pt-based catalysts are widely used, but their reliance on expensive and scarce platinum significantly limits their large-scale application. Recently, TMDs have garnered significant attention in HER catalysis. For example, the edge sites of 2H MoS₂ flakes have been found to be active in HER catalysis, prompting efforts to expose these edge sites as



much as possible in the past. However, 2H MoS₂ is semiconducting, which limits electron transport and results in low HER catalytic efficiency, compared with 1T' phase.

In contrast, 1T' MoS₂ exhibits significantly better HER catalytic performance due to its metallic nature, with both in-plane and edge sites being active for catalysis. As a result, issues related to edge site exposure or the need for doping to introduce additional active sites are eliminated, which are tricky problems, and must be considered for 2H-MoS₂-based electrocatalysts. However, it is important to note that synthesizing 1T' MoS₂ with high phase purity and stability remains a major challenge. The structure of 1T' MoS₂ is completely different from that of the 2H phase, which accounts for its superior HER catalytic performance but also its low stability. 1T' MoS2 is metastable and has higher system energy than the 2H phase, leading it to gradually transition to the 2H phase at room temperature or rapidly at temperatures above 97 °C. This inherent instability complicates the synthesis of 1T' MoS₂ and limits its reliability in applications. As a result, previous reports of as-synthesized 1T' MoS2 often showed low phase purity and poor long-term HER stability. Nonetheless, 1T' MoS2 has been recognized as an excellent, earth-abundant electrocatalyst for HER due to its metallic nature, which facilitates electron transport, and its high density of active catalytic sites. Theoretical calculations have demonstrated that pure 1T' MoS₂ exhibits outstanding electrochemical HER performance. 124 If the stabilization of 1T' MoS₂ without changing in-plane structure and properties can be realized, the HER performance and HER long-term stability will be significantly improved.

In this study, a self-intercalation method has been developed to synthesize pure 1T' MoS₂ with K₂S as the intercalant. The K₂S intercalation effectively adjusts the system's energy, stabilizing the 1T' MoS₂ and addressing its intrinsic stability issues. As a result, the low stability of 1T' MoS₂ has been overcome, and the as-synthesized K₂S-intercalated 1T' MoS₂ demonstrates excellent HER long-term stability, making it a viable candidate for HER electrocatalysis. Additionally, the 100% phase purity of the material enhances its HER



performance compared to mixed-phase electrocatalysts. The sample exhibits exceptional HER electrocatalytic performance, with a low onset potential of -73 mV at a current density of 10 mA/cm² and a low Tafel slope of 39.3 mV/dec. Furthermore, its long-term HER stability, over 30000 cycles and 1000 hours at a constant current density of 50 mA/cm², significantly outperforms other electrocatalysts.

1.3 Accomplished Milestones

- First demonstration of self-intercalation method for the synthesis and stabilization of intercalated 1T' TMDs
 - a) Nearly 100% 1T' phase purity and high crystal quality
 - b) Mass production available
 - c) Versatility (successful synthesis of various TMDs with different alkali metal chalcogenides intercalation)
- 2. First demonstration of stabilization of 1T' phase by alkali metal chalcogenides intercalation
 - a) Sustaining over 750 °C
 - b) Stability in air, water, solvents, and even strong acid
 - c) Maintaining stability after one-year aging
 - d) Demonstration of stabilization mechanism with theoretical calculations
- 3. Excellent hydrogen evolution reaction electrocatalyst of K₂S-intercalated 1T' MoS₂
 - a) Exceptional HER performance (Low onset potential of -73 mV at a current density of 10 mA/cm² and a low Tafel slope of 39.3 mV/dec)



b) Superior long-term HER stability (over 30,000 cycles and 1,000 hours at a constant current density of 50 mA/cm²)

1.4 Thesis Outline

Chapter 1 "Introduction"

The research background and the motivation are introduced. A summary of the achievements accomplished in this thesis is also provided in the Chapter 1.

Chapter 2 "Fundamentals"

This chapter lays the foundation for understanding the synthesis, properties, stabilization, and applications of 1T' TMDs, while highlighting the current challenges and advancements in the field.

Chapter 3 "Synthesis of Intercalated Phase-pure 1T' Transition Metal Dichalcogenides by Self-intercalation Method"

Chapter 3 demonstrates a novel self-intercalation method for synthesizing intercalated 1T' TMDs. K₂S-intercalated 1T' MoS₂ has been successfully synthesized using this technique, achieving nearly 100% phase purity and excellent crystal quality, as confirmed by characterization. The resulting material preserves the same in-plane structure as the intrinsic 1T' MoS₂, with K₂S intercalation within the van der Waals gap. This unique structure not only preserves the original properties of 1T' MoS₂ but also stabilizes it by reducing formation energy through intercalation. Significantly, the process utilizes low-cost reagents, a simple tube furnace, and requires only a few hours of processing time, without additional



post-treatment. These factors make the method highly scalable and suitable for industrial and commercial applications. Furthermore, the technique is versatile to a range of TMDs. In addition to K₂S-intercalated 1T' MoS₂, other intercalated materials, including Li₂S- and Na₂S-intercalated 1T' MoS₂, as well as K₂Se-intercalated 1T' MoSe₂, Na₂Se-intercalated 1T' MoSe₂, and K₂Te-intercalated 1T' MoTe₂, have also been successfully synthesized, highlighting the versatility of the method.

Chapter 4 "Stability and Stabilization Mechanism"

In chapter 4, the stability of 1T' MoS₂ with K₂S intercalation has been characterized and the stabilization mechanism has been demonstrated with the help of theoretical calculations. Notably, the stability of 1T' TMDs has gained increasing attention, as their reliability is critical for the performance of potential applications, especially considering the inherent metastability of many 1T' TMDs. The characterization results confirm the high crystal quality and phase purity of the synthesized material. The stability of K₂S-intercalated 1T' MoS₂ has been tested under various conditions, including temperature, solvent exposure, thickness variations, and aging. The synthesized K₂S-intercalated 1T' MoS₂ exhibits exceptional stability compared to previously reported samples. It demonstrates the ability to withstand temperatures exceeding 750 °C and remain stable in air, water, and ethanol, maintaining its integrity even after one year of aging. Additionally, theoretical calculations have been performed using a K₂S-intercalated 1T' MoS₂ model. The results indicate that K₂S intercalation reduces the formation energy by N-doping and bonding with the 1T' MoS₂, thereby stabilizing the 1T' phase. The band diagram analysis shows that K₂S intercalation does not alter the metallic nature of 1T' MoS₂.

Chapter 5 "Durable K₂S-intercalated 1T' MoS₂ Electrocatalyst for Efficient Hydrogen Evolution Reaction"



In Chapter 5, K₂S-intercalated 1T' MoS₂ has been directly grown on carbon cloth for hydrogen evolution reaction (HER) electrocatalyst applications. The synthesis follows the same self-intercalation method outlined in Chapter 3, offering a simple, low-cost, one-step reaction process that is well-suited for large-scale production. The resulting samples demonstrate exceptional HER electrocatalytic performance, with a low onset potential of -73 mV at a current density of 10 mA/cm² and a Tafel slope of 39.3 mV/dec, comparable to the best non-precious HER electrocatalysts, including TMDs, due to their high phase purity. Notably, the K₂S intercalation significantly enhances HER stability, with the material sustaining 30000 cycles and 1000 hours at a constant current density of 50 mA/cm², outperforming other electrocatalysts. The remarkable HER performance and long-term stability confirm that the 1T' MoS₂, prepared by the proposed self-intercalation method, retains its intrinsic catalytic activity due to the preservation of the in-plane structure of 1T' MoS₂, while the intercalation substantially boosts system stability. This self-intercalation method provides a promising approach for stabilizing the system while preserving its inherent properties, representing an effective strategy for structural engineering in HER catalysis.

Chapter 6 "Summary and Future Works"

This chapter offers a comprehensive overview of the self-intercalation method for the synthesis and stabilization of 1T' TMDs, along with their application HER. It also outlines a range of potential research opportunities that could arise from the proposed self-intercalation technique. Furthermore, a detailed research plan, inspired by the findings of this thesis, has been presented, laying the groundwork for future investigations and advancements in this area.



Chapter 2

Fundamentals



2.1 Introduction

The study of 1T' TMDs materials starts from the synthesis. The first part of this thesis is the synthesis of 1T' TMDs via proposed self-intercalation method, and the characterization. Then, the stabilization mechanism by intercalation has been studied and verified in experiments. Finally, the application of hydrogen evolution reaction (HER) electrocatalyst based on K₂S-intercalated 1T' MoS₂ has been demonstrated. So, the outline of this thesis is very clear - materials synthesis, characterization, and applications. To understand the study shown in this thesis, it is necessary to give a full picture of this research topic. This chapter demonstrates the TMDs structures of each polymorphs, their unique properties, and promising applications arising from these properties. As the 1T' TMDs synthesis is an essential role of this study, the previous synthesis methods and their advantages and drawbacks are summarized in this chapter. To evaluate the quality of sample prepared by various synthesis methods, including structure and phase purity, several vital characterization methods are commonly used which are demonstrated too. In addition to the synthesis and characterization, the stabilization of 1T' TMDs is another significant issue, as intrinsically metastable 1T' phase usually leads to difficulty and unreliability of applications. This chapter gives a summary of current stabilization methods, especially the stabilization by intercalation. The intercalation is a special feature of TMDs and other two-dimensional (2D) materials, which also plays an important role in stabilization of 1T' phase TMDs. Therefore, the issues about stabilization and intercalation are put in a section to discuss in detail. The last section of this chapter is about HER electrocatalyst. The high active sites density and earth-abundance of 1T' TMDs makes them promising candidates for HER application. The background of HER and previous reports about TMDs-based HER electrocatalysts are summarized too. In short, this chapter provides the basic knowledge about 1T' TMDs and summarizes the current techniques and challenges.



2.2 Structure of Transition Metal Dichalcogenides

TMDs represent various structures and corresponding novel properties. Even with the same composition, TMDs could be formed in several phases under different conditions. For example, the typical MoS₂ has 2H, 1T', and other phases. Although the TMDs present various phases, the layered structure is kept. Within a layer, the transition metal atoms are sandwiched by two layers of chalcogen atoms, forming a triatomic layered structure. The discussion of various phases of TMDs typically starts from the well-known 2H phase. However, the 2H phase is a general name. There are several phases with same in-plane structure with trigonal-prismatic coordination but with different layers stacking manners, resulting in 1H, 2Ha, 2Hc, and 3R. 1H phase is the monolayer form of TMDs with trigonal-prismatic coordination. The AbA BaB and AcA BcB stacking sequences lead to the formation of the 2Ha and 2Hc polytypes, respectively, as shown in Figure 2.1. In contrast, the 3R phase consists of three layers with same orientation but shifting with respect to others. The letters H or R represent the hexagonal or rhombohedral lattice system, respectively, while the integer indicates the number of layers in a unit cell. For most Group VI TMDs, the thermodynamically stable phase is 2H_c phase.¹²⁵ So, the 2H phase usually denotes 2H_c phase for Group VI TMDs. Under the high pressure, semiconducting 2H_c phase MoS₂ transforms to metallic 2H_a phase. 126 This is due to the overlap of valence and conduction bands caused by a collapse in c parameter under high pressure. 2Ha phase usually is the stable phase in Group V TMDs, which is metastable for Group VI TMDs. The structure of 2H phase can be understood as the second layer rotating around the c axis by 60° and stacking on first layer. The 3R phase Group VI TMDs is also semiconducting and represents spin-valley coupled physics, which makes them promising for spin- and valleytronic devices and nonlinear optical devices. 127 However, there are few reports about the synthesis of 3R MoS₂, among them mainly via chemical vapor transport method. 128,129 In the triatomic layer, the atomic planes gliding could transform to 1H' and 1T phases. The



transverse displacement of the transition metal plane can result in a distorted 2H phase, known as the 2H' phase, which is regarded as a 60° rotational variant of the 2H structure. ¹³⁰ It was reported that the distorted 2H phase of MoTe₂ was found under applied electric field. ⁶¹ However, this phase is unstable and is a transitional structural state between 2H_c and 1T' phases.

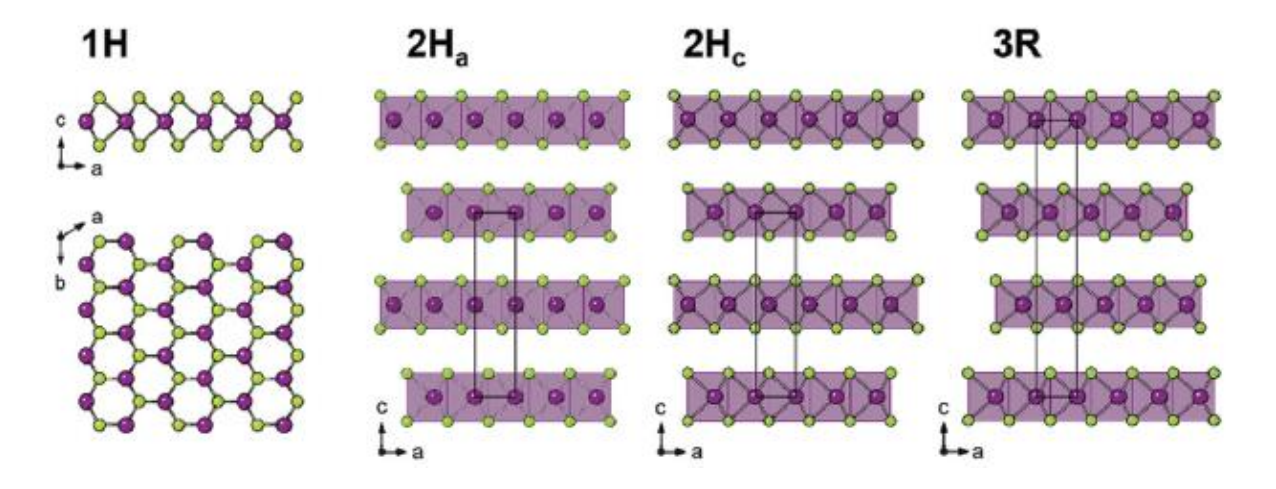


Figure 2.1: Atomic structure of 1H, 2H_a, 2H_c, and 3R phase.⁷²

In addition to the trigonal-prismatic coordination represented in 1H, 2H_a, 2H_c, and 3R phase triatomic layer, there is an octahedral coordination leading to 1T phase with the metal centers of two layers in unit cell position above each other, as shown in Figure 2.2. However, the system energy of 1T phase Group VI TMDs is usually higher than 2H phase with trigonal-prismatic coordination, so it is not thermodynamically stable. The structure distortions in 1T phase could result in clustering of transition metal atoms and corresponding buckling of chalcogen planes, which leads to the formation of distorted 1T phase. It has been found that there is zigzag chain formation (1T"), tetramerization (1T"), and trimerization (1T"") of transition metal atoms in the basal plane, forming different phases respectively. Among these distorted octahedral structures, the 1T' phase represents lowest formation energy, indicating by first-principles calculation results.¹³¹ Recently, the 1T" MoS₂ were obtained by deintercalation of KMoS₂ crystal. Bulk 1T" MoS₂ presents



semiconducting behavior with an indirect bandgap of 0.65 eV. The calculation results suggested the energy difference between 1T' and 1T" phase is quite small¹³², so the synthesis of these phases is possible. It is interesting that the energy difference between 2H and 1T' phase MoTe₂ is much smaller than other Group VI TMDs. The bulk MoTe₂ is often found in 2H phase, but it shows 1T' phase over 900 °C.¹³³

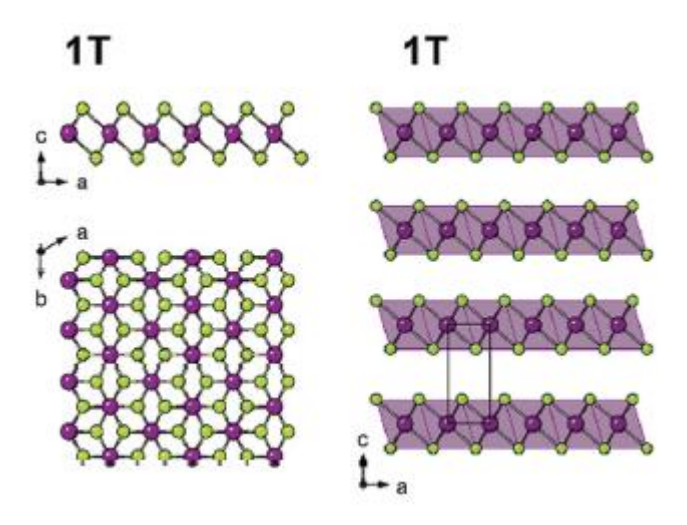


Figure 2.2: The atomic structure of 1T phase of TMDs.⁷²

Recently, the highly pure 1T' Group VI TMDs were synthesized and characterized, and the lattice structure was obtained by single crystal XRD characterization.⁷⁸ The result indicates the 1T' Group VI TMDs, including MoS₂, MoSe₂, WS₂, and WSe₂, belong to monoclinic crystal system and C2/m space group. It is worthy to note that the lattice axes definition of 2H and 1T' phase is different. Take WS₂ as example as shown in Figure 2.3, the *c* axis is the direction perpendicular to the triatomic layer in 2H phase, while *a* axis goes through the layers in 1T' phase. This point is essential when studying the interlayer distance extension by intercalation. In the past, the synthesis of pure crystal 1T' TMDs was difficult, the lattice structure of 1T' phase was not very clear and lacked sufficient crystallographic data. As a result, some papers used the same crystal system to discuss the 2H and 1T' phase which is not suitable.



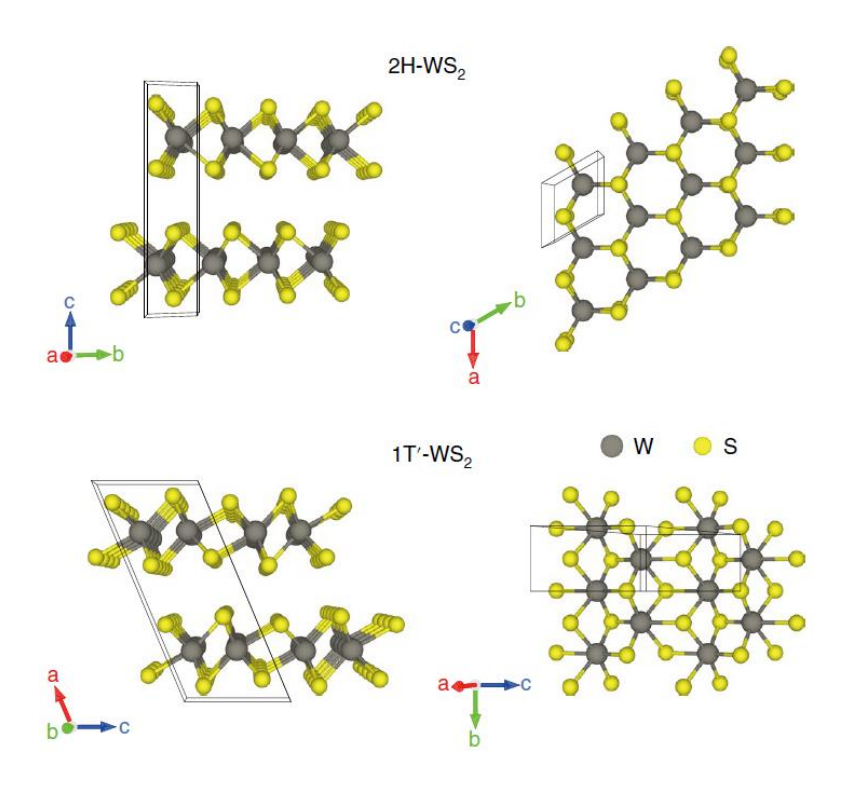


Figure 2.3: Schematic illustration of structures of 2H-WS₂ and 1T' WS₂.⁷⁸

In addition to the intrinsic structures of TMDs, the van der Waals gap in interlayer without bonding allows to restack them in specific sequences, enabling the creation of novel heterostructures, which represent unique properties compared with inherent structure. The stacking of TMDs leads to the break of inversion symmetry and tunes the optical, electronic and spintronic properties.

The TMDs family not only consists of a large number of members, but also possesses multiple phases with distinct structures and properties. The layered structure with van der Waals gap also opens up the opportunity to stack TMDs in various manners to create many special heterostructures. These special features of TMDs make them a promising platform for research and engineering.



2.3 Important Characterization Methods

The various phases of TMDs sometimes make characterization difficult, the 1T phase is similar with 1T' phases and was reported as 1T' phase in some cases.⁷² To distinguish the different phases of TMDs, some characterization methods have been commonly used. One of them is Raman spectroscopy, offering an accurate and quick method to characterize the polymorphs of TMDs. Raman spectroscopy measurement utilizes Raman scattering to detect the vibrational modes of materials involving the inelastic scattering of photons. The monochromatic light source and sensitive photo-detector are two important parts of Raman spectroscopy equipment. The laser light is applied on the materials and interacts with excitations such as molecular vibrations, phonons, and so on. The inelastic scattering causes the energy shift of the photons which represents the characteristic vibrational modes of materials. The 2H MoS₂ shows E_{2g}^{1} and A_{1g} Raman peaks, and the E_{2g}^{1} peak is the characteristic Raman peak of 2H phase. It was reported that the 1T phase of MoS₂ represented two Raman peaks, Eg (at 287 cm⁻¹) and A_{1g} (at 408 cm⁻¹)¹³⁴, and the 1T'-MoS₂ showed additional J₁, J₂, and J₃ peaks, at around 156, 226, and 333 cm⁻¹, respectively. 115 The more Raman peaks shown by 1T' phase indicate the lower symmetry compared with 2H phase. It is interesting that the J₁ mode usually presents highest intensity in Raman spectra of 1T' Group VI TMDs. 123 And it is worthy to note that Raman signal of 1T' phase is often lower than 2H phase, with same layer thickness. For 1T' MoS₂, J₂ Raman peak is related to the defects which indicates the existence of defects in 1T'-MoS₂ crystal usually caused by liquid-phase synthesis method.⁵⁹



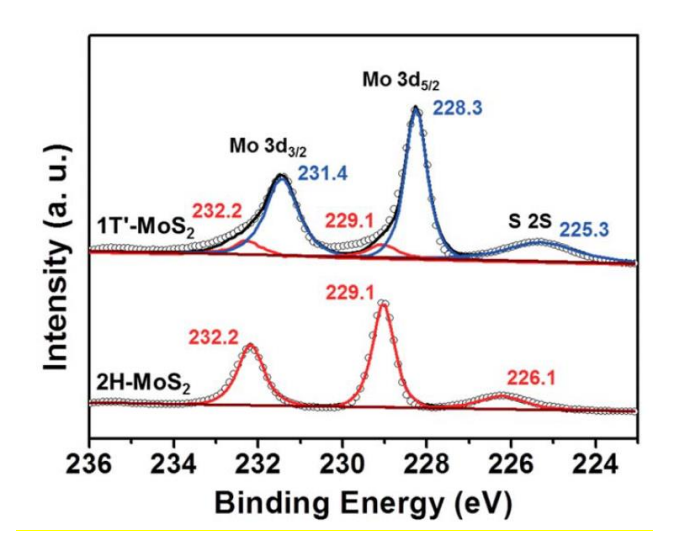


Figure 2.4: XPS Mo 3d spectra of 1T'-MoS₂ (with 2H phase impurity) and 2H-MoS₂. 115

X-ray photoemission spectroscopy (XPS) is able to evaluate the phase purity of samples. XPS is a surface-sensitive, quantitative analytical technique that probes the topmost 200 atoms (approximately 0.01 µm or 10 nm) of a material's surface. As a member of the photoemission spectroscopy family, XPS gathers electron spectra by applying X-rays on a material. The technique identifies the elements of a material via mechanism of photoelectric effect—both those on its surface and within it—along with their chemical states. XPS also provides detailed information about the material's overall electronic structure and the density of electronic states. One of its key advantages is that it not only reveals the elements in a material, but also shows how these elements are bonded to one another. The synthesis of metastable 1T' phase TMDs remains a huge challenge, as the formation of 1T' phase is higher than 2H phase. As a result, the prepared 1T'-TMDs samples usually were a mixture of 1T' and 2H phase. To evaluate the phase purity of sample, the XPS characterization is a common and reliable method. The binding energy of transition metal atoms and chalcogen atoms in 1T' phase is lower than those in 2H phase. 115 This energy difference is enough large to be detected by XPS. By comparing the ratio of XPS peaks arisen from 1T' and 2H phase, it is able to obtain the information of phase purity of samples. Figure 2.4 gives the XPS spectra of 1T'-MoS₂ sample with 2H phase impurity and 2H-MoS₂, in which the



binding energy of 1T' phase shifts to lower value than 2H phase and the phase purity can be obtained.

The transmission electron microscopy (TEM) is a direct and essential structure characterization method. During the TEM measurement, the electron beam is focused and transmits the sample, with a thickness lower than 10 nm to obtain high-resolution TEM image. The electron beam transmits the specimen and interacts with lattice structure of material, then projecting on the screen with the structure information. The wavelength of electron beam is much shorter than light, so the resolution of TEM is higher than optical microscopy, typically 0.1-0.2 nm. The 1T' phase presents distinct zigzag-transition-metal chains which can be used to distinguish from other phases. However, the 1T and 2H phases, both exhibiting three-fold symmetry in the basal plane, are nearly indistinguishable in high-resolution TEM (HRTEM) images. Recent studies have shown that the intensity of chalcogen columns in high-angle annular dark-field (HAADF) STEM images is different in 1T and 2H phase structure, therefore they are distinguishable via this technique, as shown in Figure 2.5¹³⁵. Because the chalcogen atoms in trigonal prismatic 2H structure stack along the incident direction of electron beam during TEM measurement, resulting in high-intensity spots in TEM image and formation of honeycomb shape pattern. However, the chalcogen atoms in octahedral 1T structure creates much lower intensity compared with transition metal atoms, which leads to a hexagonal pattern in HRTEM image. It is worthy to note that the residual aberrations may lead to the quasi-atomic columns which are possible to appear in Fourier-filtered images. By acquiring the selected area electron diffraction (SAED) patterns along the [001] zone axis, the 2H and 3R phase can be distinguished by comparing the intensity of (100) and (110) diffraction spots, which differs greatly in 3R phase but are equal in 2H phase.



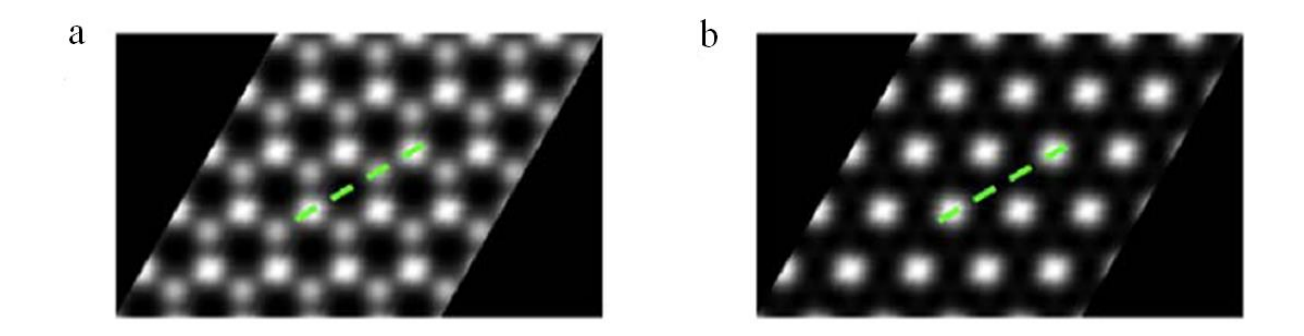


Figure 2.5: Simulated HAADF STEM images of ideal (a) 2H and (b) 1T phases. The bright spots correspond to Mo atoms. In the 2H phase, S atoms are visible as less bright spots. ¹³⁵

2.4 Properties and Applications

The band structures of single-layer MoS₂ with 1H, 1T, and 1T' phase acquired by theory calculations are represented in Figure 2.6.¹ The K–K transitions are closely associated with the transition metal d-orbitals (Mo) which indicates a direct bandgap in 1H MoS₂. The transition metal d-orbitals contain 2 electrons, which are typically paired and fully occupied in the lowest d₂₂ state, owing to the hexagonal symmetry of the 1H-phase. As a result, the semiconducting structure of the 1H-phase is stabilized by the electron configuration of the transition metal d-orbitals.¹³⁶ If the 1H MoS₂ layer stacks to form 2H phase MoS₂, the bandgap presents a decrease with the increase of thickness along with the transition to indirect bandgap. The direct bandgap of semiconducting monolayer MoS₂ makes it a promising candidate for optoelectronic applications, such as photodetectors. The semiconducting behavior of 1H or 2H MoS₂ also allows it to be available for field effect transistor application, showing high carrier mobility and on/off ratio.



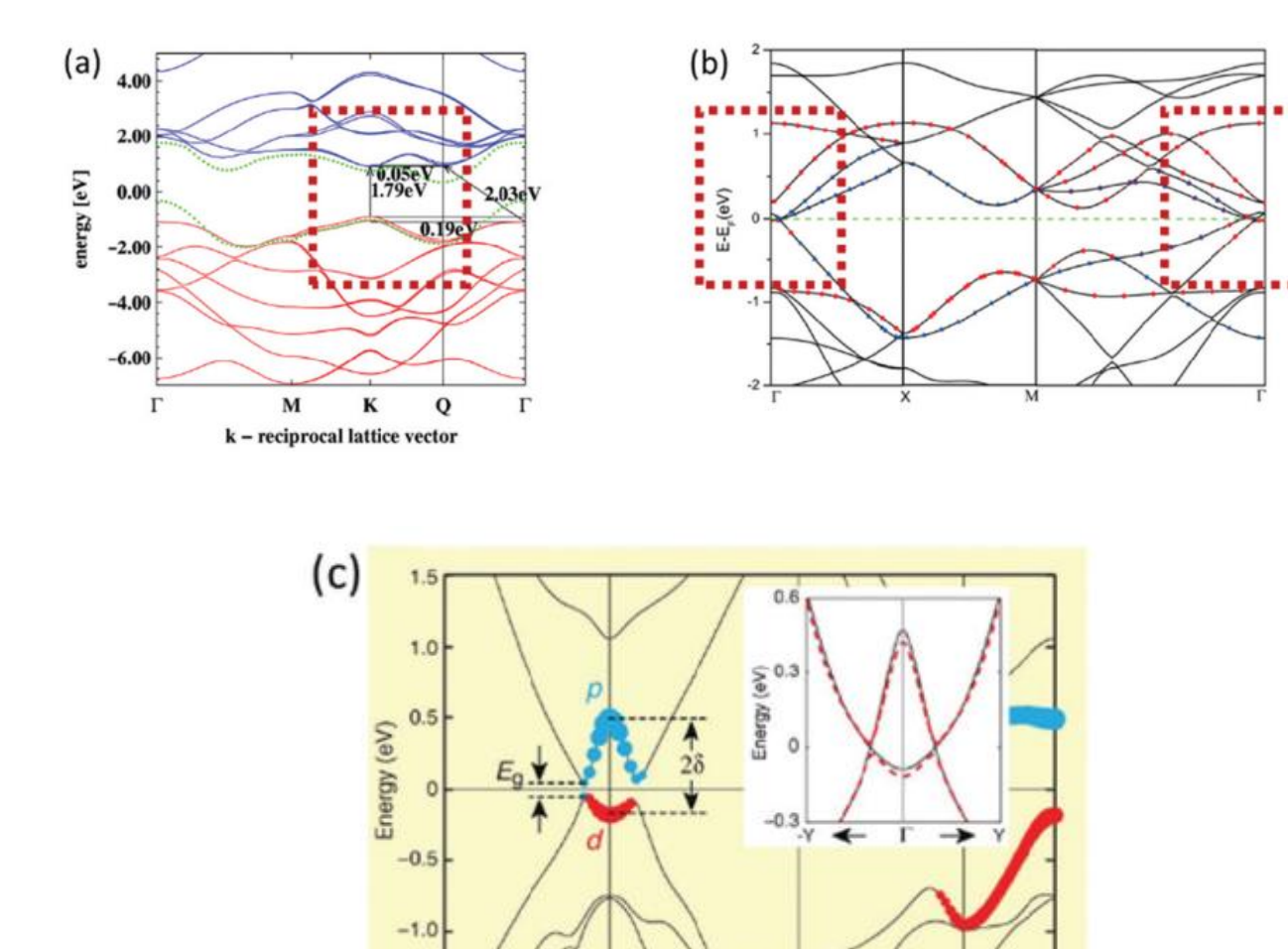


Figure 2.6: Theoretically and experimentally determined band structures of (a) 1H, (b) 1T, and (c) 1T'-phase monolayer-MoS₂.¹

In the 1T-phase, the degeneracy of the electronic structure—caused by the tetragonal symmetry—leads to partially occupied d-orbitals (specifically the lowest degenerate $d_{xy,yz,xz}$ orbitals). This partial occupancy is responsible for the metallic character of the phase. Near the Γ -point, the Fermi level intersects both the Mo d-orbitals and the S p-orbitals, further contributing to its metallic nature.¹³⁷ Because the 1H phase TMDs are stabilized by the electron configuration of the transition metal d-orbitals, N-doping caused by intercalation,



doping, gating could change the electron configuration in d-orbitals, thus leading to the transition to 1T phase. In addition to the N-doping, the applied strain was also found able to cause phase transition.

The zigzag chains in the 1T'-phase of 2D TMDs causes the shift of transition metal d-orbitals, below the chalcogen p-orbitals, which leads to a band inversion and inverted gap at the Γ -point, while there are two Dirac cones around the Γ -point. When spin-orbit coupling is introduced, a fundamental gap (E_g) opens at the Dirac points. It is confirmed that the inverted and fundamental gaps exist in experiments, among various 1T' TMDs with different gap energy.

The unique properties of 2D transition metal dichalcogenides (TMDs) have made them a focal point of research, especially in the fields of semiconducting and metallic phases. In the semiconducting phase, TMDs exhibit desirable characteristics such as direct bandgap, high charge carrier mobility, and excellent on/off current ratios, making them ideal candidates for applications in transistors and optoelectronics. However, the discovery of metallic or semi-metallic phases, such as the 1T and 1T' configurations, has expanded the potential applications of these materials. The metallic phases offer enhanced conductivity and the ability to tap into new electronic functionalities, such as spin- and valleytronics. This has led to increased interest in developing TMD-based heterostructures, which combine the benefits of both semiconducting and metallic phases. These heterostructures could enable novel devices that leverage both charge and spin degrees of freedom, providing a pathway to advanced technologies in quantum computing, low-power electronics, and optoelectronic devices. As the versatility of TMDs continues to grow, the challenge remains in harnessing the properties of these materials across different phases and integrating them into practical, scalable devices. While the development of TMD-based electronics is still in its early stages, it holds significant promise for advancing beyond traditional field-effect transistors to create innovative logic circuitry systems. Recent reports have highlighted the fabrication of



microdevices such as integrated transistors, logic inverters, and prototype microprocessors based on various TMD materials. 139-141 These early-stage demonstrations underscore the potential of TMDs to revolutionize electronic devices, offering advantages in scalability, energy efficiency, and performance.

Silicon photonics is promising technology to enhance the interconnects response speed and reduce power consumption, while the conventional metal interconnects are limited by Joule heating and parasitic capacitance. Some 2D materials have direct band gap, suitable for light emission and detection, thus they have the potential to build optical to electrical interconnects devices. Juan et al.¹⁴² reported MoS₂ photodetectors integrated with Si₃N₄ waveguide which can propagate the TE mode of incident light and make MoS₂ layer's absorption of light easier, thus enhancing the photoresponsivity. Moreover, an isolation layer of h-BN between MoS₂ and Si₃N₄ was used to prevent the charge transfer to Si₃N₄, which could change the threshold voltage, to increase the response speed. In addition, a graphene top gate with h-BN dielectric layer can adjust the working state of device.

Peyskens et al. ¹⁴³ also did a work in the similar field. They built a single photo emitter (SPE) by transferring WSe₂ flake on silicon nitride photonic integrated circuits (PICs). By interfacing the 2D-SPE with an integrated dielectric cavity, single photon extraction enhancement was achieved with the integration of SPEs with the guided mode of a SiN waveguide. Besides, there is no requirement of additional processing of SPE host materials, thus this method is more efficient and low-cost. Combining with the wafer-scale 2D materials synthesis technology, it allows the fabrication of integrated circuits with low-power-consumption and fast photo-electricity interconnects.

The integration of graphene and conventional silicon IC was reported by Stijn et al.¹⁴⁴ To overcome the problem of small detection bandwidth of conventional silicon-based image sensor IC, graphene film was transferred on CMOS IC with readout circuit array and then



patterned to form separate components compose the detectors array. This structure utilizes the excellent broadband detection ability of graphene and well-developed silicon IC process to build a broadband camera.

The artificial neural network (ANN) is an efficient structure for image sensing. Because the data processing of input signals requires fast processing and low power consumption, this structure can conduct the image sensing, data storage, and processing simultaneously. Lukas et al. 145 built an ANN based on WSe2 film with external data processing circuit. The ambipolar conduction behavior of WSe2 enables the tunability of photoresponsivity by adjusting gate voltage with double gate structure. Moreover, the dark current of double-gate WSe2 photodetector does not change with the vibration of photoresponsivity and has a linear photoresponsivity-gate voltage relationship, not like photonic mixing and metal–semiconductor–metal detectors which are nonlinear relationship and have not fixed dark current. Therefore, the WSe2 based ANN is suitable for machine learning to eliminate the noise, and obtain clear and accurate output of image sensing.

In addition to above mentioned devices, some interesting inventions are also worthy of notice. Kamarauskas et al. 146 combined light energy harvest based on MoS₂ with other circuits to achieve self-powered system. The fabrication of array of plasmonic photodetector using plasmon enhancement to increase the photoresponsivity was also reported. 147 The device showed a photoresponsivity of 9 A W⁻¹ and a detectivity of 5 × 10¹¹ Jones when applying 660 nm laser with an intensity of 0.5 mW cm⁻². Besides, the use of paper substrates resulted in mechanically flexibility.

TMDs have served as hydrogen evolution reaction (HER) catalyst for a long time. It's known the edge sites of TMDs with layer structure are catalysis active, but the basic panels of TMDs usually are inactive for HER. Unfortunately, the 2H phase group VI TMDs are semiconductors and bare low electric conductance, leading to the poor carrier transport



efficiency, thus not suitable for electrochemical hydrogen generation. Thanks to the semimetal or metallic 1T/1T' phase group VI TMDs' small resistance, these materials possess superior HER performance with low cost due to the earth abundant element composition. An electrochemically active electrode was developed, using a solvothermal method to grow piezoelectric 1T MoSe₂ nanosheets on carbon cloth. As the metallic 1T MoSe₂ was used to build the electrode, as a result, the large interlayer distance, improved hydrophilicity, and increased conductivity significantly enhance the reduction of the Zn²⁺ diffusion barrier.⁵⁹ The metallic or semi-metallic 1T group VI TMDs can also serve as contact materials to reduce the contact resistance and greatly improve the field effect transistors performance. It was reported that the 2H and 1T' phase MoTe₂ homojunction was fabricated by phase transition via applying laser on materials. By using this technique, the carrier mobility of the MoTe₂ transistor was increased by a factor of about 50, while the on/off current ratio was kept as high as $10^{6.148}$ The intrinsic hydrophilicity and improved conductivity of 1T MoS₂ were confirmed and made it a promising candidate as supercapacitor electrode material. 149 The supercapacitor based on 1T MoS₂ with excellent electrochemical properties allows various cations intercalation into the interlayer of MoS₂, significantly enhancing the storage ability.

A novel topological field effect transistor with heterostructures of 1T' TMDs and 2D dielectric layers were proposed by Xiaofeng Qian et al., as shown in Figure 2.7, which can turn on or off in extreme high speed compared with conventional transistor. This demonstrated device can switch the states through topological phase transition induced by external electric field. In contrast, the conventional field effect transistor utilizes the carrier depletion to turn on/off, with inherently low speed.⁷² The first-principles calculations indicated that the a branch of 1T' phase TMDs are large-gap quantum spin hall insulators, with an band inversion between p band of chalcogen atoms and d band of transition metal atoms induced by structural distortion.



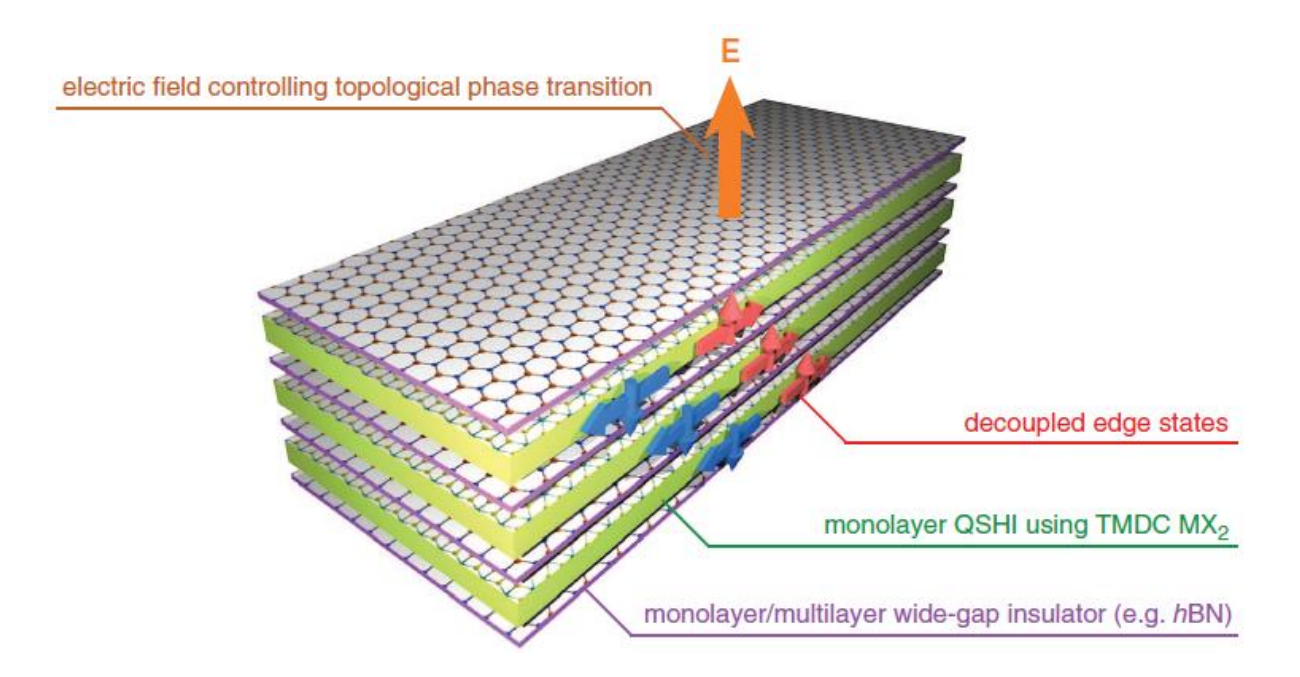


Figure 2.7: Schematic of the topological field effect transistor. 136

The mass application of 2D materials requires the development of 2D-materials-based integrated circuits fabrication technology, consist of two issue, namely synthesis and device structure design. The current wafer-scale 2D materials synthesis technology is mainly based on the use of single-crystalline substrate and epitaxial growth. The selection of specific substrate for each kind of 2D materials makes this method not efficient and flexible. Further study is still needed to develop a low-cost synthesis method. The integrated circuits based on or combined with 2D materials can utilize the excellent physical and opto-electronic properties of 2D materials to achieve an advanced function with the structure of systematically connected numerous components. This can be achieved either by integration with current well-developed silicon IC or by ingenious device structure design.



2.5 1T' TMDs Preparation Methods

The study of 2D TMDs has been a popular topic in recent years, as they possess unique physical and chemical properties and atomic-thin thickness, similar to graphene. Thanks to TMDs' novel properties, they show great potential in electronic, optoelectronic devices, as well as catalysis. Many TMDs (such as MoS₂, MoSe₂, WS₂, WSe₂, and so on) are polyphase materials which generally present trigonal prismatic or octahedral phase, referring to the 1H and 1T phase with D_{3h} and D_{3d} symmetry, respectively. The distorted structures of 1T phase result in 1T', 1T" or 1T" phase, and 2H or 3R phases can be obtained by stacking of 1H layers in different ways. Though not all the TMDs are polyphase materials, quite a large proportion of TMDs have 1T and 1H phases, and usually one phase is thermally stable and the other is metastable. More importantly, the different phases refer to different structures, thus showing different properties. Molybdenum disulfide, the one of the most typical TMDs, has stable semiconducting 2H phase and metastable metallic 1T' phase. Semiconducting 2H phase MoS₂ shows layer-dependent band gap which makes it suitable for electronic and optoelectronic applications, while 1T'-MoS2 show good electrons transport ability, and superconductivity at low temperature. In addition, magnetism and ferroelectricity are also observed in 1T' MoS₂. Owing to these special properties, MoS₂ of 1T' phase has promising future in electronics, catalysis and batteries. Other TMDs also present similar phenomena and other novel features.

The synthesis of thermally stable phase of 2D TMDs has been well studied and developed, but the preparation of metastable phase TMDs is still a huge challenge. Take MoS₂ as an example; there are many reports about the synthesis of 2H phase MoS₂ flakes and large-area film by top-down or bottom-up methods. However, the preparation of wafer-scale 1T' MoS₂ film with high phase purity has not been achieved yet. Although there are reports of preparing 1T' MoS₂ flakes or powder by alkali atom intercalation, the low phase purity and



low crystallinity remains problems. Actually, all the problems originate from the metastability of 1T' phase of MoS₂, the energy barrier between the 2H phase and 1T' phase makes MoS₂ prefer to 2H phase structure. Though 1T' MoS₂ does can exist in atmosphere at room temperature for a period, annealing over 100 °C transforms 1T' phase to 2H phase completely and gradual transformation can be observed in few months. Not only does it lead to the difficulty of phase purity improvement, it also makes the preparation of 1T' MoS₂ tricky, as special processes are required to overcome the energy barrier. This section will give a review of the preparation of 1T' phase TMDs.

2.5.1 Preparation through Phase Transition

Generally, there are two means to obtain 1T' phase TMDs, phase transition and direct synthesis. The phase transition methods mostly involve phase transformation from 2H to 1T', as 2H phase TMDs, especially Group VI TMDs, usually are thermodynamically stable, thus easy to be obtained. Although there are various methods involving the strategy of phase transition, the fundamental mechanism behind these methods is that the energy barrier between 2H and 1T' phase can be lowered by electron transfer. The direct synthesis of 1T' TMDs also usually involves the electron transfer mechanism.

Many phase transition methods involve the intercalation of alkali atoms, in some cases, the vacancy, trap, stress in crystal would also cause phase transition. Because it can tune the system energy and overcome the energy barrier between trigonal prismatic and octahedral phase. The intercalation of alkali atoms in TMDs has been already studied in the last century. This has been a popular topic as the transformed 1T' phase TMDs usually are good catalysts and show superconductivity at low temperature.

The chemical treatment method, one of the preparation techniques via phase transition, has



a long history, dating back to 60s in last century. By immersing TMDs powders into n-butyllithium, t-butyllithium, or LiBH4, the lithium intercalation compounds of TMDs were obtained. The later hydrolysis forms hydrogen gas in the interlayer and separates the flakes of TMDs into single or few layers. It is accompanied by the transfer of electrons from lithium to transition metal d-orbitals, which leads to the decrease of formation energy difference between 1T' and 2H phase, thus causing the phase transition from 2H to 1T' phase. Typically, these methods require immersing TMDs into n-butyllithium solution for few days at room temperature or elevated temperature (up to ~ 100 °C). It is interesting that the necessary amount of intercalated lithium for phase transition is influenced by thickness. With the increase of thickness, the required number of induced charges per volume reduces, thus easier to transform to 1T' phase. As a result, the thinner MoS₂ flakes need longer process time and higher n-butyllithium solution concentration, as shown in Figure 2.8.¹⁰⁷

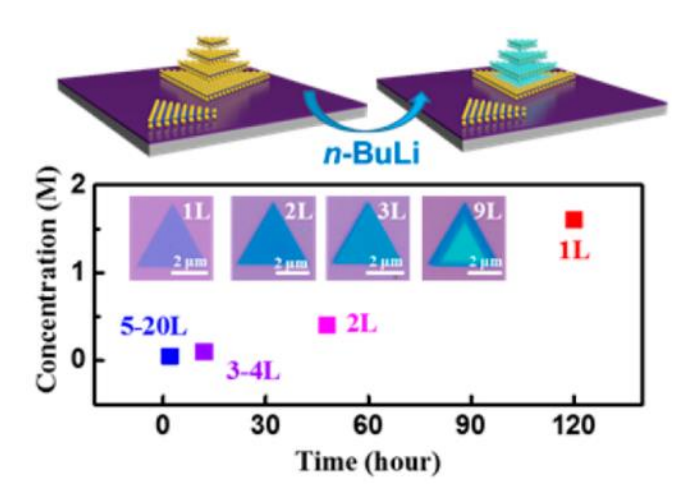


Figure 2.8: Concentration and process time required for phase transition from 2H to 1T' phase for different thickness. 107

Although it's reported that 2H WSe₂ flakes¹⁵⁰ or powder was transformed to 1T' phase, the ratio of 1T' phase was not enough high. It is worth noticing that the conducting 1T' WSe₂ as electrodes of field effect transistor greatly improves the performance. This method is simple and easy, but it's not effective when it comes to polycrystalline TMDs film. It's proved that



the n-butyllithium treatment cannot achieve the phase transition of polycrystalline MoS_2 grown by sputtering of Mo and sulfurization. The grain boundaries in polycrystalline MoS_2 may trap electrons transferred from n-butyllithium, thus preventing phase transition via charge transfer mechanism. Despite this method is simple, the products suffer from small flake size and low phase purity (typically $70\%\sim80\%$). What's worse, the metastable 1T' phase TMDs transform back to 2H phase gradually, and this would be more serious when the intercalated ions are removed and the nanoflakes restack again. The phase transition from 1T' phase to 2H phase also happens instantly at an elevated temperature, for example, as low as ~100 °C for 1T' MoS_2 and ~200 °C for 1T' WS_2 .

With the help of electrochemical intercalation of lithium, it is also able to prepare 1T' TMDs, similar to the chemical treatment methods. During the electrochemical intercalation process, the lithium metal foil and TMDs are employed as anode and cathode, respectively. The lithium insertion was achieved under an applied external potential, which led to uniform intercalation. Then the intercalated samples were sonicated in water to separate into monolayer 1T'-phase TMDs flakes with size up to 1 µm. 151

It was reported that the 2H phase TMDs were transformed to 1T' phase TMDs by annealing the mixture of 2H phase TMDs and metal salts, such as K_2CO_3 , $K_2C_2O_4 \cdot H_2O$, KHCO₃ and so on, which is also available for 1T' phase TMDs alloys synthesis. ¹⁴⁸ $A_{0.5}XS_2$ (with A = Li, Na, K, Rb, or Cs, and X = Ti, or Nb) could be obtained by the reaction of XS_2 and alkali halide with H_2S gas environment at 800 - 1000 °C. However, if without H_2S gas, in inert gas instead, the alkali metal intercalated tantalum sulfide could be formed. ¹⁵²

Electrostatic gating is another phase transition method to obtain metastable phase TMDs. It was reported that excess charge induced by external electric field can lead to the phase transition of TMDs. However, for lighter TMDs monolayer (such as MoS₂, WS₂), a quite large amount of charge should be transferred to trigger the phase transition, namely a large



gate voltage, making it not feasible. However, it's found that tuning the chemical composition via alloying could greatly decrease the required gate voltages for MoTe₂ phase transition.⁶²

Based on the charge transfer mechanism, the most direct phase transition manner would be electron irradiation. It was reported that the electron beam scanning on 2H-phase Re-doped MoS₂ for a period could cause the build-up of negative charges, thus leading to phase transition.¹³⁰ However, this method can only produce an extremely tiny domain of 1T' phase TMDs.

An interesting phase transition method is via applying mechanical strain to TMDs. MoTe₂ experienced the 2H-to-1T' phase transition after applying a tensile strain using AFM tip. As MoTe₂ has smaller energy difference between 1T' and 2H phase, it's easier to be transformed compared with other TMDs. Besides, there are microwave plasma treatment and the supercritical CO₂ treatment to achieve phase transition. These methods are controllable and versatile, enabling phase engineering in liquid phase.¹⁵² However, the conversion ratio by these methods usually is not high, varying from 70% to 90%.

2.5.2 Direct Synthesis Methods

The main disadvantage of phase transition method is the low phase purity, which forces researchers to put forth a lot of effort to directly synthesize the metastable phase TMDs. Using molecular beam epitaxy to grow 1T' MoS₂ on Au(111) substrate was reported, it's found that the gold substrate actually is an electron donator and promotes the formation of 1T' structure. Similarly, by contacting with electron donor materials, charge transfer to TMDs can also be achieved. It was reported that the 2H MoTe₂ stacking with 2D electride (such as Ca₂N) caused a high density of electron doping, thus leading to 2H-to-1T' phase



transition. However, the size of 1T' phase domain was around 1 µm. 153

The reduction of K₂MoS₄ at elevated temperature in hydrogen is a method to synthesize 1T' MoS₂. Liu⁵⁹ used K₂MoS₄ as CVD precursor to directly synthesize 1T' MoS₂ under hydrogen/argon atmosphere. It was found that the ratio of hydrogen influences the ratio of 1T' phase, higher the hydrogen proportion, higher purity of 1T' phase. The typical synthesis of K₂MoS₄ is achieved by the reaction of K₂MoO₄ with hydrogen sulfide at elevated temperature for nearly a day.⁶² In addition to this method, there is another K₂MoS₄ preparation technique involving a series of chemical reactions. The solution containing ammonium heptamolybdate (HMA), (NH₄)₆Mo₇O₂₄·4H₂O, and ammonium hydroxide was reacted with high-purity H₂S gas by bubbling for 60 min to prepare ATTM. The ATTM was put into potassium hydroxide solution, followed by vacuum pumping, removing NH₃, and precipitation, resulting in solid K₂MoS₄.

The electron donating precursors, alkali intercalated TMDs, such as KMoS₂, can also be employed to synthesize 1T' TMDs. Firstly, to produce the precursor of KMoS₂, K_2MoO_4 reacted with H_2S , followed by reduction in hydrogen. Or by the reaction of A_2S , MS_2 , and M (A=Li, Na, K, M=Mo, Nb, Ta, Ti), AMS₂ can also be obtained. The next step was to hydrate the intercalated alkali atoms to obtain $K_x(H_2O)_yMoS_2$ and then treated samples with an oxidizer. It is worth notice that the amount of intercalated alkali atoms and the strength of oxidizer have essential influence on the products. With x around 0.3, 1T' MoS_2 was obtained by incomplete oxidation of $K_x(H_2O)_yMoS_2$. On the other hand, complete oxidation resulted in 1T'" phase. It was found that the oxidation of $K_x(H_2O)_yMoS_2$ with x lower than 0.3 led to 1T' phase too. 154

2.6 Intercalation, Self-intercalation, and Stabilization

Intercalation has been an interesting and popular topic of TMDs. There is van del Waals gap



between TMDs layers without bonding. The in-plane structures of 1T' phase TMDs and 2H phase TMDs are completely different, however, both them are layered materials. These special structures of TMDs make intercalation much easy. The intercalation has also been used to exfoliate the TMDs to obtain monolayer or few-layer sheets recently. It was found that the intercalation can lead to the phase transition. For example, the 2H-phase MoS₂ transforms to 1T' phase after Li intercalation. The phase transition from 2H to 1T' can also be achieved by other alkali metal intercalation; it is due to the n-doping caused by intercalation. And it's worthy to note that the alkali metal intercalation can stabilize the 1T' phase which is intrinsically metastable, as the n-doping can lower the energy difference between 1T' phase and 2H phase.

Many 1T' TMDs are metastable, especially Group VI TMDs, such as 1T' MoS2, 1T' MoSe2. The distinct chemical and physical properties of 1T' TMDs encourage researchers to look for stabilization method to improve the reliability. To achieve the stabilization of 1T' TMDs without changing in-plane structure and properties, intercalation is a promising method. Both 1T' and 2H phase is layered structure with van der Waals gap between layers, though the 1T' TMDs have totally different in-plane structure from 2H phase. The intercalation into the van der Waals gap could change the formation energy of whole system without modifying the in-plane 1T' structure, thus providing a reliable method to achieve the stabilization of 1T' phase while keeping its intrinsic properties. The intercalation methods have attracted tremendous attention recently. The technical issues that usually concerns us are stability, phase purity, defects, and productivity. However, the current intercalation methods do not meet the expectation that the phase-pure stable 1T' TMDs with high crystal quality should be obtained. In this thesis, a self-intercalation method has been developed to directly synthesize stable intercalated 1T' TMDs with extremely high phase purity and high crystal quality. In this chapter, the previous intercalation methods are summarized.



2.6.1 Intercalation methods

The van der Waals gap of TMDs make intercalation possible. The intercalation is mainly utilized to tune the chemical and physical properties of TMDs, or purely a study method. The engineering of intercalated super lattice structure is promising and provide opportunities to create a large class of new combined materials with designed structure and properties. Though this thesis focuses on the stabilization of 1T' TMDs via intercalation, it is necessary to summarize the previous intercalation techniques, even not all intercalations are intended to stabilize metastable phase of TMDs.

(a) Chemical Treatment

Chemical treatment has been a frequently used method to achieve intercalation. The intercalation reagents are mainly alkali-metal-based chemicals. And lithium is most often seen in these methods, as it is most chemically active among alkali metals, therefore the electrons in lithium would be easier to be transferred to TMDs. The butyllithium, lithium metal, and lithium borohydride are usually selected as intercalation reagents. Tan et al. immersed 2H MoS₂ into butyllithium to obtain Li-intercalated MoS₂.96 The reaction between alkali metal and MoS2 in liquid ammonia was reported to obtain Cs0.3MoS2, Rb_{0.3}MoS₂, K_{0.4}MoS₂, Na_{0.3}MoS₂, and Li_{0.4}MoS₂. ¹⁵⁶ Papageorgopoulos et al. directly deposited Li metal on MoS2 to achieve intercalation reaction accompanied by a phase transition from 2H to 1T.157 Except for the direct deposition, dissolving lithium in liquid ammonia and then immersing 2H TMDs in it for a period of time is another option. 156 Lithium borohydride was used by Zhang et al. to conduct scalable solid lithiation and of metal telluride nanosheets. 158 Sodium naphthalenide, exfoliation alkali-metal-based chemicals are also suitable candidates for chemical treatment methods. 159 These chemical treatment methods use highly active chemicals and require inert gas



environment, such as argon. The intercalated TMDs are also active, the exposure to air or water could cause oxidation of both intercalant and transition metal and destroy the intercalation structure.

The 1T' phase purity and crystal defects are two main issues for intercalation. The maximal 1T' phase percentage that chemical treatment can achieve is 70-80%. This phase purity is still too low. For certain applications, the 1T' phase is preferred over the 2H phase, making the purity of the 1T' phase critical to performance. For example, 1T' phase TMDs have much higher hydrogen evolution reaction (HER) catalysis activity than 2H phase. Therefore, the HER performance highly depends on the 1T' phase purity if not involving the issues of doping or exposure of active edge sites. Because the reaction rate of chemical treatment is affected by particle size. The intercalation is usually uneven. The milling process could help the situation, but additional crystal defects are caused.⁹⁶ The extension of chemical treatment time can improve phase purity slightly, however, the usual treatment time is 1-3 days. This resort would greatly decrease the productivity, but with less improvement. It's worthy to note that the high amount of alkali metal intercalants could cause the reduction of TMDs, leading to decomposition reaction.¹²¹ Besides, the thinner TMDs sheets require more n-doping amount per volume. 160 The thickness of TMDs is difficult to keep same. Moreover, for many applications, the intercalants should be removed after phase transition to avoid oxidation. The metastable 1T' phase spontaneously transforms to 2H phase. These factors together lead to low phase purity for chemical treatment methods.

(b) Electrochemical Intercalation

Electrochemical intercalation is conducted in a two- or three-electrode cell with intercalant metal as anode, TMDs material host as cathode, and electrolyte. This method requires conductive host and ionic intercalant, thus limiting its applications. However, as the



intercalation is controlled by external bias, this method has more reversibility and controllability. Therefore, in suit characterization of optical and electric response of TMDs during the intercalation process is available. Li et al. intercalated potassium ions into the MoS₂ flake by applying external voltages. 161 It was found that the potassium ions intercalation is reversible, and the abrupt reduction of diffusion coefficient indicates the unfavorable energy change within K_xMoS₂ structure. Except for the inorganic intercalants, charged organic molecules can also be intercalated into layer gap with the help of electrochemical process. This enables the formation of organic/inorganic superlattices with tunable chemical and physical properties. Wang et al. reported the electrochemical intercalation of cetyl-trimethylammonium bromide (CTAB) into phosphorene with tunable intercalation structure and properties.¹⁶² The CTAB can be periodically intercalated into every one, two, or three phosphorene layers. The interaction between layers is weakened, as the interlayer distance is increased by CTAB intercalation, therefore the band gap can be tuned. Thanks to the passivation by organic molecules, the FET devices built based on CTAB-intercalated phosphorene showed high on/off ratio, mobility, as well as excellent stability. By controlling the system of organic intercalation, it is available to fabricate various kinds of superlattice with combination of organic intercalants and TMDs, which possess unique structures and represent distinct physical and chemical properties.

(c) Growth Intercalation

The direct reaction between metals and TMDs at high temperatures is a common manner to obtain a number of intercalated TMDs. For example, the mixture of Cu and NbS₂ was heated and kept at 800 °C for few days, resulting in the product of Cu_{0.65}NbS₂. However, this method cannot avoid the formation of unwanted by-product, such as CuS. The similar reaction between Eu and NbS₂ also led to the ferromagnetic EuS formation.¹⁴⁹ Besides,



alkali metals were also used as intercalants. At 800 °C, the alkali metals reacted with niobium and tantalum dichalcogenides and formed A_xVS_2 , where A is alkali metal and V is Nb or Ta, with x up to 0.7. The reaction using alkali carbonate¹⁴⁸ and alkali halide¹⁵² were also reported.

Melting of several elements in a stoichiometric manner is an intuitive way to synthesize intercalation structure. In melt growth method, the intercalant element and precursors are mixed and heated. The single-crystalline Cu_xBi₂Se₃ is synthesized by melting the stoichiometric mixtures of Cu, Bi, and Se.¹⁶³ Molecular beam epitaxy (MBE) was used to grow Ta-intercalated TaS₂ film, with increased Ta flux.¹⁶⁴ The alkali atom intercalated TMDs can also be formed by annealing of A₂MS₄ (A=Na, K, M=Mo, W) in H₂^{62,115} at 850 °C, or by the reaction of A₂S, MS₂, and M (A=Li, Na, K, M=Mo, Nb, Ta, Ti)¹¹⁶ at 800 °C. These reactions at high temperature produce samples with higher crystal quality, compared with chemical treatment methods. However, the synthesized intercalated TMDs by these methods have a structure similar with 2H phase. To obtain 1T' TMDs, these intercalated TMDs need a post chemical reaction.¹¹⁵ This chemical reaction would cause defects and lower the crystal quality, which is similar with the cases of chemical treatment methods.

2.6.2 Intercalation and Stabilization

Intercalation can be used to transform the 2H phase TMDs to 1T' phase. The 2H phase TMDs are thermodynamically stable, and it is easy to be synthesized. However, many 1T' phase TMDs are metastable, the direct synthesis of 1T' TMDs is difficult. So, to prepare 1T' phase TMDs, it usually follows the way of phase transition from 2H phase to 1T' phase. The intercalation is a feasible solution to achieve phase transition, which is also an important 1T'



phase TMDs preparation method. The intercalation lowers the energy difference between 1T' phase and 2H phase, which is the reason for phase transition. As the system energy is adjusted, the intercalation also stabilizes the 1T' phase which is inherently thermodynamically metastable.

(a) Mechanism of 1T' Phase TMDs Preparation and Stabilization via Intercalation

N-doping, or also called charge transfer, caused by intercalation is the main reason of phase transition. The n-doping can increase the electron count on transition metal d-orbitals, and the transition barrier of 2H-to-1T' phase transition can be lowered, as shown in Figure 2.9.160 The thermodynamically stable 2H phase TMDs are easier to be synthesized. The 1T' phase TMDs could be obtained by phase transition from 2H phase to 1T' phase. The phase transition via intercalation has been an important preparation method for 1T' TMDs, such as 1T' MoS₂, 1T' MoSe₂. The intercalation is not only the 1T' TMDs preparation method but also the stabilization method for 1T' phase. If the intercalation structure is kept, the 1T' phase would be stable with the n-doping induced by intercalation. 123 It has been found that removal of intercalants after phase transition leads to the gradual phase transition from 1T' to 2H.¹³⁴ As the 1T' phase of many TMDs are metastable, they transform to thermodynamically stable 2H phase naturally. Therefore, the intercalation is a 1T' TMDs preparation method as well as stabilization method. However, the current intercalation methods must use chemically active intercalants, usually alkali metals, such as Li, Na, and K. Because the active alkali metals are strong electron donors. These alkali metal intercalated TMDs cannot expose to air or water, otherwise the oxidation of alkali metals is unavoidable. And the intercalation structure would be damaged, and often followed by oxidation of TMDs too. 165 So, the intercalated TMDs can be only stored in inert gas environment. It is an unacceptable limitation for quite a lot of applications of 1T' TMDs.



For example, hydrogen evolution reaction (HER) requires 1T' TMDs catalysts immersing in strong acid or alkaline solution. Therefore, developing a more reliable stabilization method is needed. The following section summarizes the current stabilization methods.

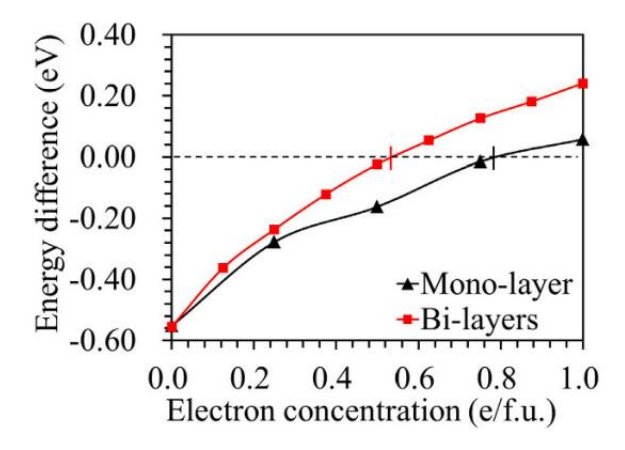


Figure 2.9: Energy difference between 2H-phase MoS₂ and 1T'-phase MoS₂ as a function of electron concentration within monolayer or bilayer. ¹⁶⁰

(b) Stabilization Methods

Stabilization of metastable phase of TMDs is a huge challenge. There are few reports about stabilization of 1T' TMDs. Because the low stability is originated by the atomic structure itself. The modification of in-plane structure, such as inducing doping, would cause additional defects and strain. The phase transition and stabilization caused by inducing defects was reported by Cai et al. The phase transition of MoS₂ is localized, which is not suitable for pure phase TMDs preparation. However, the intercalation engineering in van der Waals gap of TMDs may be a better solution. There are some reports demonstrating the stabilization of metastable phase TMDs, but the stabilization is still not good enough for applications. Park et al. proposed a molten-metal-assisted intercalation approach to stabilize 1T TMDs. The thermal stability of 1T MoS₂ has been improved to 350 °C, but the synthesized sample was the mixture of 1T and 2H phase MoS₂. Tan et al. reported that the lithium metal was deposited on 2H MoS₂ and then hydrogenated to form LiH-intercalated



1T' MoS₂.¹²³ The LiH intercalant is more stable compared with Li intercalant, showing 3-moth stability in air and 5-hour stability in water. However, the lifetime is still short and surface degeneration is unavoidable. The stabilization of 1T' TMDs remains a huge challenge, especially when it requires high stability with high phase purity and preservation of inherent in-plane 1T' phase structure and properties.

2.7 Summary

This chapter provides an overview of the structural properties of TMDs and their polymorphs, highlighting the unique properties and promising applications that arise from these characteristics. It concludes with a discussion on HER electrocatalysis, emphasizing the potential of 1T' TMDs due to their high active site density and earth-abundant elements, and summarizes other promising applications of TMDs. It also reviews previous synthesis methods for 1T' TMDs, outlining their limitations and drawbacks. Several key characterization techniques are discussed to assess the quality of the synthesized samples in terms of structure and phase purity. Next, the stabilization issue of 1T' TMDs is discussed, focusing on intercalation methods which could have a potential to achieve stabilization without changing intrinsic 1T' phase in-plane structure. In short, this chapter lays the foundation for understanding the synthesis, properties, stabilization, and applications of 1T' TMDs, while highlighting the current challenges and advancements in the field.



Chapter 3

Synthesis of Intercalated Phase-pure 1T' Transition Metal Dichalcogenides by Self-intercalation Method



3.1 Introduction

Transition metal dichalcogenides (TMDs) have recently garnered significant attention due to their unique layered structures and exceptional physicochemical properties, similar to those of graphene. The TMDs family comprises not just a collection of compounds; each compound often has multiple phases with distinct properties. 1,63 The most common and well-studied phases, such as the thermodynamically stable 2H phase of MoS₂, are at the forefront of research. In contrast, other phases, which possess higher system energy, tend to be unstable and gradually convert to the stable phase, presenting a substantial challenge in the synthesis of high-purity, metastable phase TMDs with excellent crystal quality. 72 Among various metastable phases, the 1T' phase has attracted considerable interest. Metastable TMDs exhibit unique electronic, optical, and electrochemical characteristics compared to their stable-phase counterparts, offering promising applications in superconductivity⁷⁸, device contacts⁸⁴, surface-enhanced Raman scattering (SERS)⁵², energy storage⁹⁰, electrochemical catalysis 96,97, supercapacitors 45, and synaptic transistors 98,99. To unlock these potential applications, it is crucial to produce metastable-phase TMDs with high phase purity and achieve stabilization. Phase transitions in group VI TMDs from the stable 2H phase to the 1T or 1T' phase have been reported via methods of chemical treatment 107, electrostatic gating¹⁰⁸, and mechanical strain application¹⁰⁹. However, the resulting low phase purity (up to around 80%) leads to diminished performance, and these methods impose stringent conditions that are unsuitable for large-scale production. In addition to phase transition methods, direct synthesis of metastable phase TMDs via colloidal reactions 110,111 and solvothermal processes 112,113 has also been explored. Unfortunately, these approaches also suffer from low phase purity and crystal quality. Recently the chemical oxidation of alkali atom intercalated transition metal dichalcogenides (TMDs) with a structure similar to the 2H phase¹¹⁴ was used to produce the 1T or 1T' phase of group VI TMDs. These alkali atom intercalated TMDs are primarily created by annealing A₂MS₄



compounds (where A = Na or K, and M = Mo or W) in H₂ at 850 °C^{62,115}, or through the reaction of A₂S, MS₂, and M (where A = Li, Na, or K, and M = Mo, Nb, Ta, or Ti) at 800 °C¹¹⁶. This method can achieve approximately 90% phase purity; however, the post-chemical treatment often leads to crystal defects. Additionally, the 1T or 1T' phase TMDs have a limited lifespan, even at room temperature, as they gradually convert to the more stable 2H phase^{117,118}, which is accompanied by a decline in performance. Stabilizing metastable-phase TMDs without altering their intrinsic properties presents a significant challenge. Introducing alkali atom intercalation offers an alternative approach to achieve thermodynamically stable 1T' phase TMDs. However, the chemically active alkali atoms are not stable in air, leading to the oxidation of transition metals.^{58,119,120} Achieving high purity in the 1T' phase necessitates a high alkali atom intercalation ratio, which can result in the reduction of TMDs and the formation of transition metal.¹²¹ The synthesis of 1T' TMDs with both high phase purity and stabilization remains a significant challenge.

Here, a self-intercalation method has been developed to synthesize and stabilize phase-pure 1T' MoS₂ with K₂S intercalation. The resulting material exhibits thermodynamic stability and is inert to air, ethanol, and water. Raman spectroscopy and transmission electron microscopy (TEM) have confirmed the high crystal quality of the 1T' phase, while X-ray photoelectron spectroscopy (XPS) has demonstrated nearly 100% phase purity. Thermogravimetric analysis (TGA), differential scanning calorimetry (DSC), and annealing tests have revealed thermal stability exceeding 750 °C, in contrast to intrinsic 1T' MoS₂, which transforms to the 2H phase at 97 °C¹¹⁵. Additionally, it has been extended to produce Na₂S-intercalated 1T' MoS₂, Li₂S-intercalated 1T' MoS₂, K₂Se-intercalated 1T' MoSe₂, Na₂Se-intercalated 1T' MoSe₂, and K₂Te-intercalated 1T' MoTe₂, highlighting the versatility of this approach for synthesizing various 1T' phase TMDs.



3.2 Characterization Equipment

The optical images were captured using a Leica DM2700 optical microscope. Scanning electron microscope (SEM) images were acquired with a Tescan MAIA3 field emission scanning electron microscope. Atomic force microscopy (AFM) images and height profiles were obtained using an Asylum MFP-3D Infinity scanning probe microscope. Raman spectra were recorded with a WITEC Confocal Raman spectroscopy, employing a 532 nm laser excitation at 0.5 mW power. X-ray diffraction (XRD) patterns were measured using a Rigaku SmartLab X-ray diffractometer equipped with a 9-kW rotating anode X-ray source, a scintillation counter, and a 1D high-speed detector. XPS spectra were acquired with a Thermo Fisher Scientific Nexsa instrument, featuring a monochromatic and focused 12 kV aluminum Kα X-ray source. TEM images and energy-dispersive X-ray spectroscopy (EDS) mapping were performed using a Thermo Fisher Spectra 300 scanning transmission electron microscope. DSC curves were measured with a Mettler Toledo DSC, covering a temperature range of -90 to 400 °C and heating/cooling rates from 0.1 to 300 °C/min. TGA curves were obtained using a Mettler Toledo TGA/DSC3+ system, featuring a balance sensitivity of 0.01 μg.

3.3 Synthesis and Characterization of K2S-intercalated 1T' MoS2

3.3.1 Synthesis Process

A three-zone furnace equipped with a one-meter-long quartz tube was employed for the direct synthesis of 1T' MoS₂, as illustrated in Figure 3.1. To ensure accurate synthesis, it is essential to use a completely clean quartz tube with no residual substances, particularly sulfur, which may remain from prior use. A new and clean quartz tube was utilized for each



synthesis in this work. Sulfur powder (10 g) was loaded into an alumina boat, on the upstream end of the tube (heating zone 1). The sulfur acted as excess reagent and covered the bottom of cuboid alumina boat (bottom area: 910 mm²) throughout the synthesis process, ensuring uniform supply of sulfur by evaporation. K₂MoO₄ powder (60 mg) was positioned in the downstream end of the tube (heating zone 3), evenly distributed on a sapphire substrate (area: 2 X 2 cm²) on top of an alumina boat, while the middle heating zone 2 was left empty. Before starting the synthesis, the tube was evacuated to remove air and then purged with argon until atmospheric pressure was restored. During the process, argon gas was flowed at 35 sccm, with hydrogen added at 15 sccm, maintaining atmospheric pressure. Zones 2 and 3 were then heated to 750 °C at a rate of 15 °C min⁻¹, while zone 1 was kept at room temperature. Once zones 2 and 3 reached 750 °C, zone 1 was heated to 135 °C at 30 °C min⁻¹, ensuring controlled sulfur vaporization. This step prevented premature sulfur release and undesired reactions at temperatures below the growth threshold. If a quartz tube is reused, it must be thoroughly cleaned to avoid residual sulfur vaporizing during heating, which could lead to undesirable low-temperature reactions. The temperatures in zones 2 and 3 were maintained at 750 °C for 4 hours, while zone 1 was held at 135 °C. Afterward, the furnace cooled down naturally to room temperature. The sample was retrieved after complete cooling, yielding K₂S-intercalated 1T' MoS₂ without requiring any post-treatment.

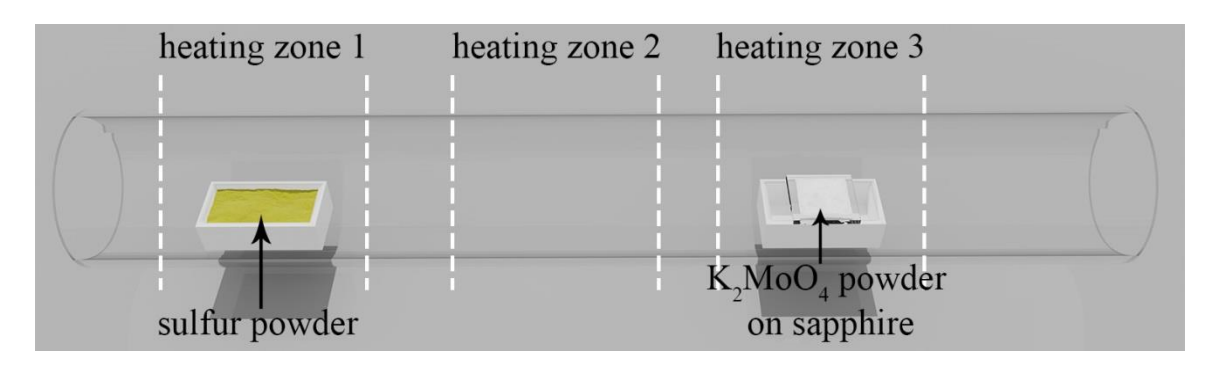


Figure 3.1: Schematic of K₂S-intercalated 1T' MoS₂ synthesis setup.



3.3.2 Characterization Results

As shown in Figure 3.2a and 3.2b, the as-synthesized K₂S-intercalated 1T' MoS₂ powder consists of numerous stacked trapezoidal flakes, with individual flakes reaching sizes over 100 µm. This morphology differs significantly from the typical triangular flakes of 2H MoS₂. The powder also exhibits a distinct metallic luster, as shown in the inset of Figure 3.2a. The as-synthesized sample exhibits a unique Raman spectrum (Figure 3.3a) that differs from that of 2H MoS₂. The characteristic J₁ and J₃ peaks of the 1T' phase are clearly distinguishable, confirming the presence of high-quality 1T' phase MoS₂. Notably, the defect-related Raman peak J₂^{97,115,168,169}, which is commonly observed in samples prepared using solution-phase intercalation methods, is absent, indicating the lack of typical defects. In addition to the characteristic 1T' peaks, three additional Raman peaks (labeled A, B, and C) associated with the intercalation are observed. For comparison, n-butyllithium treatment, a common method for preparing 1T' MoS₂¹, was applied to transform 2H-phase MoS₂ into the 1T' phase. Briefly, 2H-phase MoS₂ flakes were grown on SiO₂/Si substrates by chemical vapor deposition (CVD) using MoO₃ and sulfur powders as precursors. These flakes were then immersed in a 2 M n-butyllithium solution in cyclohexane for 200 hours in an argon-filled glove box. The treated samples were thoroughly washed with cyclohexane and dried. The Raman spectrum of the n-butyllithium-treated sample (Figure 3.3a) shows significantly weaker peaks compared to those of the K₂S-intercalated 1T' MoS₂ prepared in this work, indicating inferior crystal quality. This suggests the demonstrated self-intercalation method is better than commonly used chemical treatment methods.



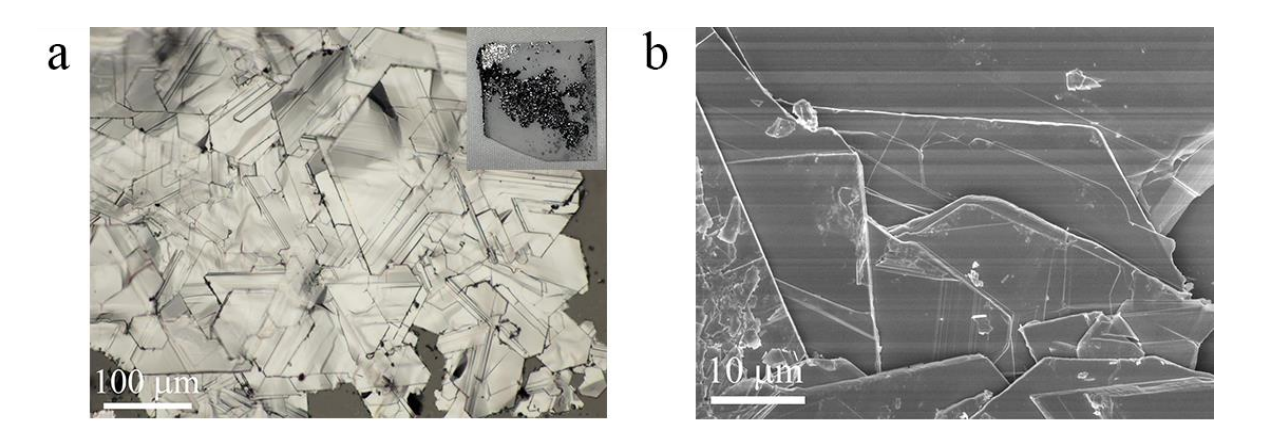


Figure 3.2: Characterization of K₂S-intercalated 1T' MoS₂. (a) Optical and (b) SEM images of K₂S-intercalated 1T' MoS₂ powder, respectively. Inset of (a), Photo of K₂S-intercalated 1T' MoS₂ powder on the sapphire substrate.

XRD was employed to analyze the structure of the sample. As shown in Figure 3.3b, the as-synthesized K₂S-intercalated 1T' MoS₂ exhibits an increased interlayer distance, d₍₂₀₀₎ (0.9064 nm), compared to intrinsic 1T' MoS₂ (0.5876 nm) and 2H MoS₂ (0.6148 nm). The intercalation also extends the lattice constant *a*, from 1.2835 nm to 1.9797 nm. This structural change is illustrated in the lattice schematic in Figure 3.4, which highlights the expansion of both the interlayer distance and the lattice constant *a* due to intercalation. Notably, the structure of 1T' phase is greatly different from usual 2H phase. Recently, the specific lattice parameters of 1T' MoS₂ were measured using single-crystal XRD.⁷⁸ 1T' phase belongs to monoclinic crystal system and *C2/m* space group. As illustrated in Figure 3.4, only *a*-axis goes through the MoS₂ layers. Therefore, the extension of interlayer distance directly leads to the increase of lattice constant *a*, consistent with the XRD data. The well-defined XRD peaks with lattice planes parallel to the basal plane of MoS₂ indicate a preference for two-dimensional (2D) growth, where the structure extends along the basal plane. This growth tendency is also evident in the flake-like morphology shown in Figure 3.2a and 3.2b.



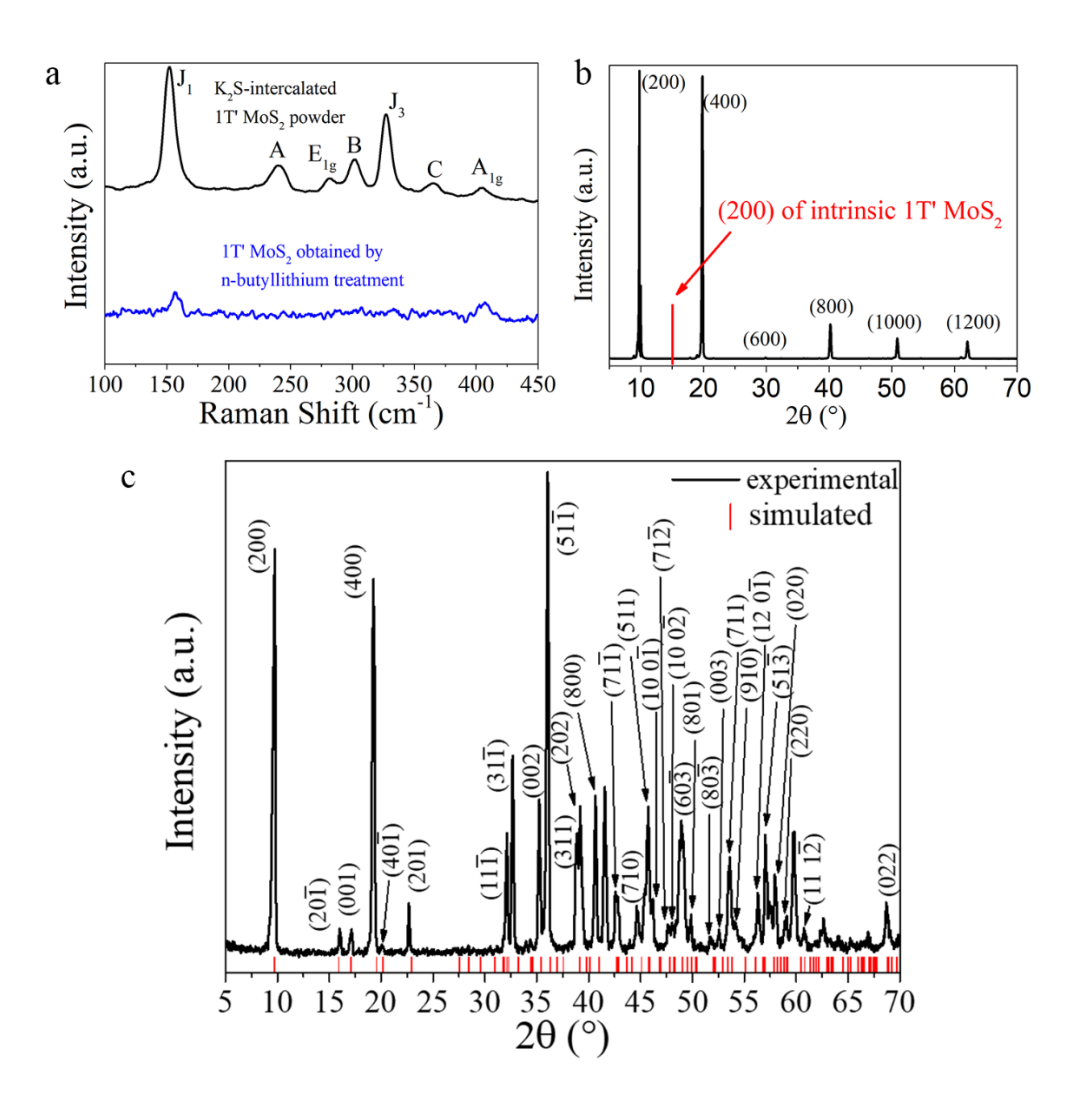


Figure 3.3: (a) Raman spectra of K₂S-intercalated 1T' MoS₂ powder and 1T' MoS₂ obtained by n-butyllithium treatment. XRD results of (b) as-synthesized and (c) fully stirred K₂S-intercalated 1T' MoS₂ powder, respectively.

To further examine the lattice structure, the K₂S-intercalated 1T' MoS₂ powder was scraped off the substrate, spread, and filled into an XRD powder sample holder for testing. The resulting XRD pattern (Figure 3.3c) displays more peaks compared to the previous XRD result (Figure 3.2f), due to the random orientation of MoS₂ flakes during the last mentioned XRD sample preparation. The expanded lattice constant *a* significantly shifts the positions of the XRD peaks relative to intrinsic 1T' MoS₂. To confirm the structural changes, a lattice model was constructed (Figure 3.4) to simulate the XRD spectrum, assuming the same basal



plane structure as 1T' MoS₂ but with an extended *a*. As shown in Figure 3.3c, the experimental XRD data aligns closely with the simulated spectrum, strongly supporting the conclusion that the as-synthesized sample retains the in-plane structure of intrinsic 1T' MoS₂ while exhibiting an increased interlayer distance due to intercalation.

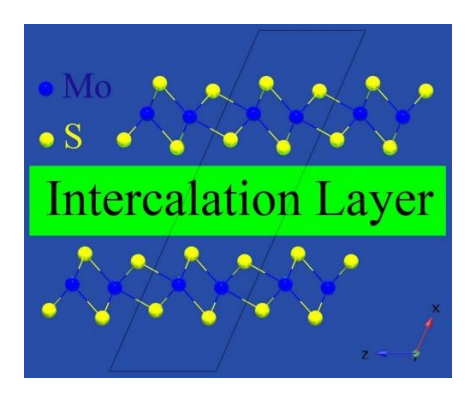


Figure 3.4: Lattice model of K_2S -intercalated 1T' MoS₂. Lattice constant a, b, c is along the direction of x, y, z axis, respectively.

The phase purity of 1T' TMDs samples have been commonly evaluated using XPS. ^{1,78,168,169} As shown in Figure 3.5a, the Mo 3d XPS spectrum reveals that the Mo 3d_{5/2} and Mo 3d_{3/2} peaks exhibit lower binding energies (228.00 eV and 231.17 eV, respectively) compared to those of 2H MoS₂. These binding energies align closely with previously reported values for 1T' MoS₂. ¹⁶⁸ The fitting results indicate only one set of Mo 3d peaks, with the fitting curve matching the experimental data perfectly, confirming the high phase purity of the prepared sample. Additional XPS tests (Figure 3.6) further validate this finding, showing consistent results with only one set of Mo 3d peaks in each spectrum. These results confirm that the sample's phase purity is nearly 100%, as determined by the precision of XPS analysis. The presence of potassium is evidenced by the K 2p XPS peaks (Figure 3.5b), with binding energies of 295.0 eV (K 2p_{1/2}) and 292.2 eV (K 2p_{3/2}), corresponding to univalent potassium ions (K⁺). The sulfur XPS spectrum reveals two distinct chemical environments, represented by two sets of fitting curves. As shown in Figure 3.5c, the larger sulfur contribution matches



the binding energy of S in 1T' MoS₂, and a 1:2 atomic ratio of Mo to S is derived by quantifying this sulfur component. The remaining sulfur exhibits a higher binding energy (162.37 eV, S2p_{3/2}), suggesting bonding with potassium atoms. This component yields a 2:1 atomic ratio of K to S. Consequently, the chemical formula is determined to be (K₂S)_xMoS₂, with x=0.18. Raman spectroscopy and XRD results confirm that the in-plane structure of the material remains consistent with intrinsic 1T' MoS₂. This suggests that K₂S is located in the interlayer spaces, indicating its intercalation within the layered 1T' MoS₂ structure. Further evidence supporting this conclusion is provided by subsequent TEM characterization.

TEM characterization was performed to examine the lattice structure of the samples, with the results presented in Figure 3.7. The distinct feature of the 1T' phase superstructure, namely the Mo zigzag chains, is clearly visible in the high-resolution TEM (HRTEM) image (highlighted in Figure 3.7c). A schematic of the in-plane lattice structure of 1T' MoS₂ (Figure 3.9) also depicts these Mo zigzag chains. The selected area electron diffraction (SAED) pattern (Figure 3.7d) and the fast Fourier transform (FFT) pattern (inset of Figure 3.7c) confirm the distorted octahedral coordination characteristic of the 1T' MoS₂. Figure 3.8 show EDS mapping, which provides evidence of the presence of Mo, S, and K. The detected K originates from the intercalation of "K₂S."



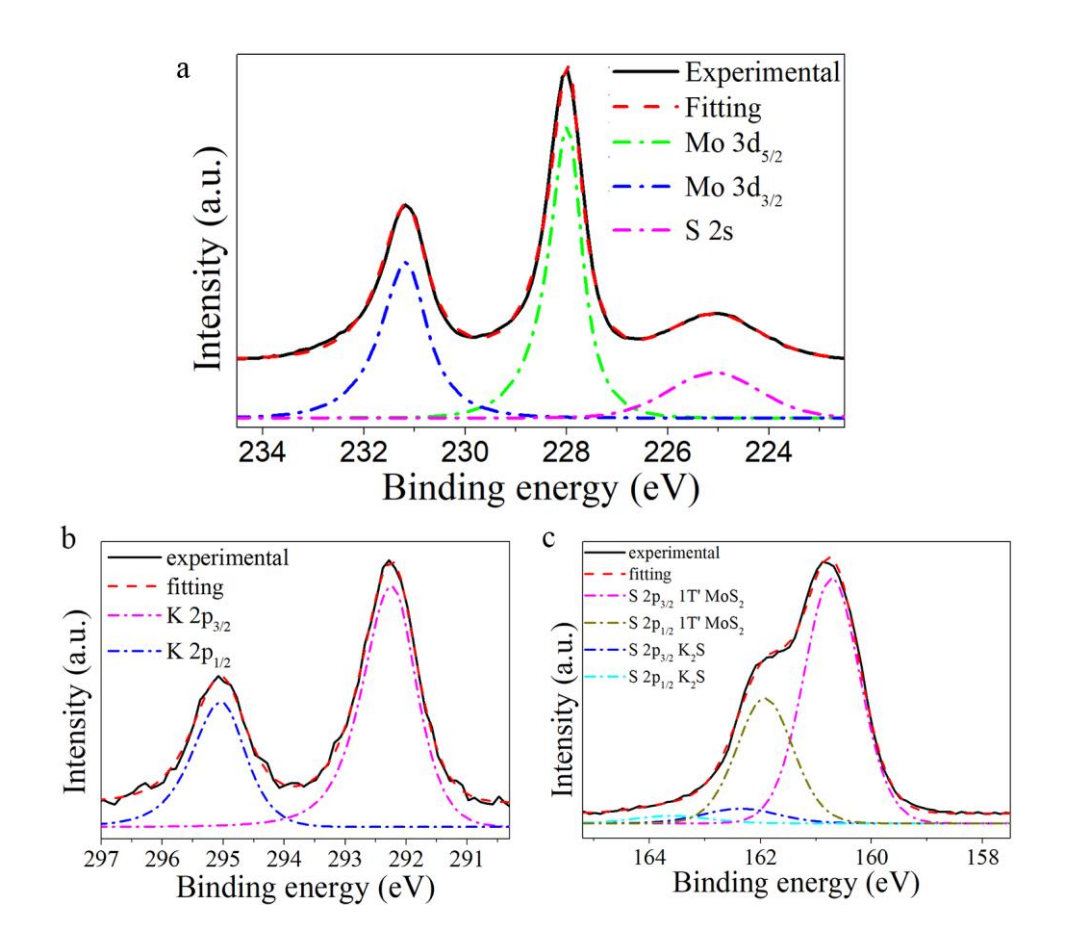


Figure 3.5: Experimental and fitted XPS (a) Mo 3d and S 2s, (b) K 2p, and (c) S 2p spectra of K₂S-intercalated 1T' MoS₂ powder, respectively.

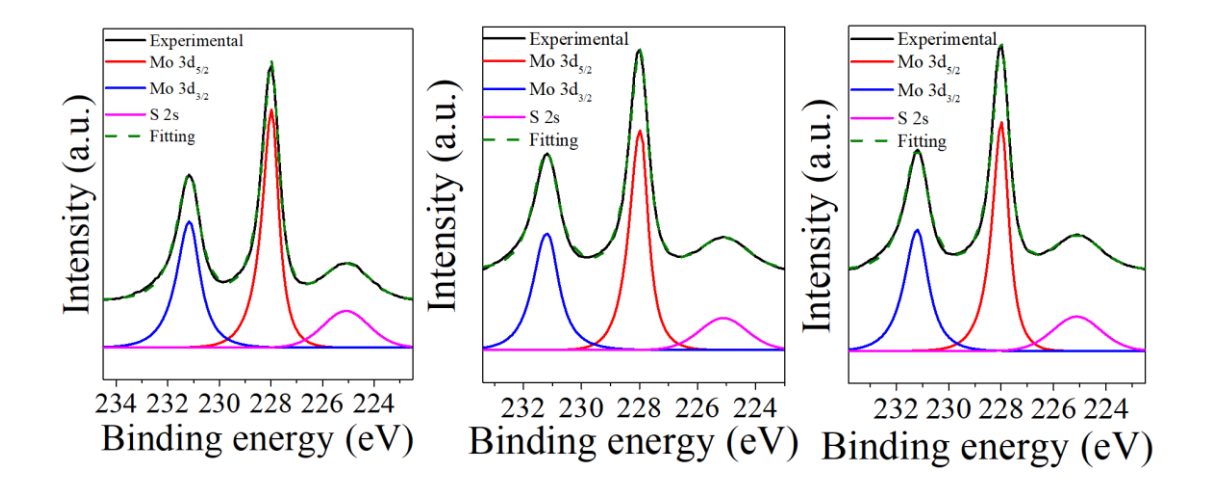


Figure 3.6: Another three XPS results of K₂S-intercalted 1T' MoS₂ in random sampling.



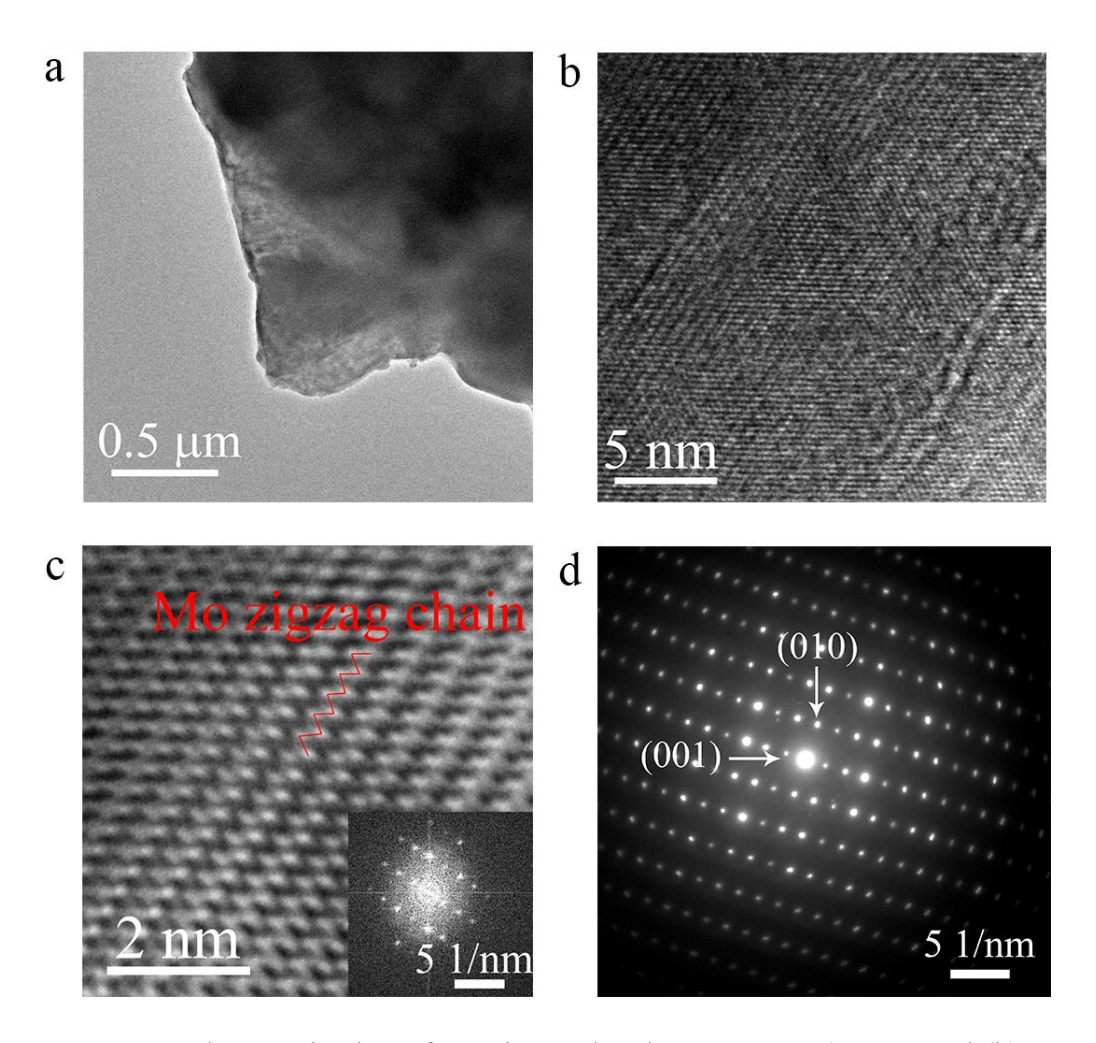


Figure 3.7: TEM characterization of K₂S-intercalated 1T' MoS₂. (a) TEM and (b) HRTEM images of K₂S-intercalated 1T' MoS₂, respectively. (c) Fast Fourier transform (FFT) filtered images of (b). Inset of (c), FFT pattern of (b). (d) SAED pattern of K₂S-intercalated 1T' MoS₂.

Cross-sectional TEM was employed to further investigate the intercalation, with results shown in Figures 3.10. Details of the sample preparation process are provided below. First, the K₂S-intercalated 1T' MoS₂ was ultrasonically dispersed in ethanol and subsequently drop-dried onto a silicon substrate. A selected flake of K₂S-intercalated 1T' MoS₂ was identified, and its location was determined. A carbon protection layer was then deposited onto the surface of the sample. Next, focused ion beam-scanning electron microscopy (FIB-SEM, FEI Scios) was used to prepare the cross-sectional TEM sample. The two longer



sides of the sample were cut first, followed by rotating the sample to cut the bottom and one shorter side. Finally, the cross-sectional TEM sample was lifted using a manipulator and securely welded onto a holder. As shown in Figure 3.10, the interlayer distance is extended to 0.893 nm, closely matching the d₍₂₀₀₎ spacing of 0.9064 nm measured by XRD. EDS mapping under high-angle annular dark-field scanning TEM (HAADF-STEM), presented in Figure 3.11, reveals the distribution of Mo, S, and K. The mapping confirms that K layers are located between MoS₂ layers. These findings corroborate that the synthesized sample possesses the in-plane lattice structure of 1T' MoS₂, with "K₂S" intercalated between the layers. The cross-sectional TEM image and its brightness profile (Figure 3.10a, b) show an extended van der Waals gap of 0.893 nm. This observation aligns with the XRD spectrum in Figure 3.3b, which also indicates an interlayer distance extension. Furthermore, the intercalation of K₂S increases the *a*-axis lattice parameter from 1.2835 nm to 1.9797 nm due to the increase of interlayer distance.

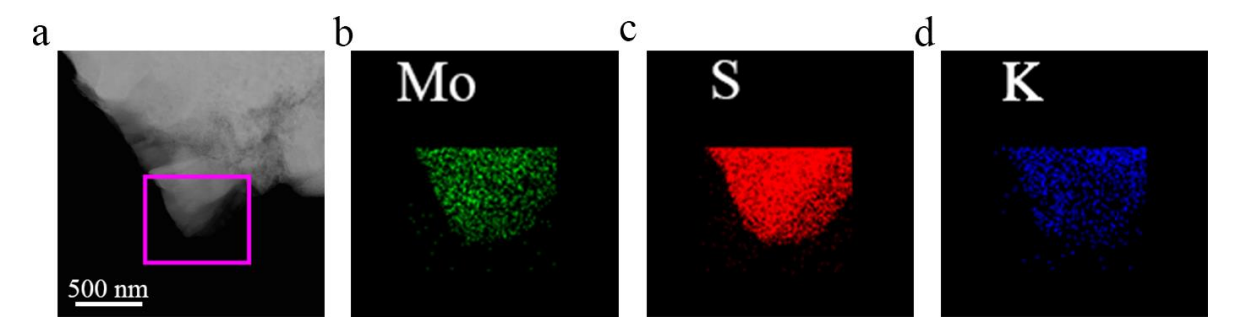


Figure 3.8: (a) Dark-field STEM image of K₂S-intercalated 1T' MoS₂. (b-d) Elemental mapping images of Mo, S, and K, respectively, acquired from pink rectangular box in a.



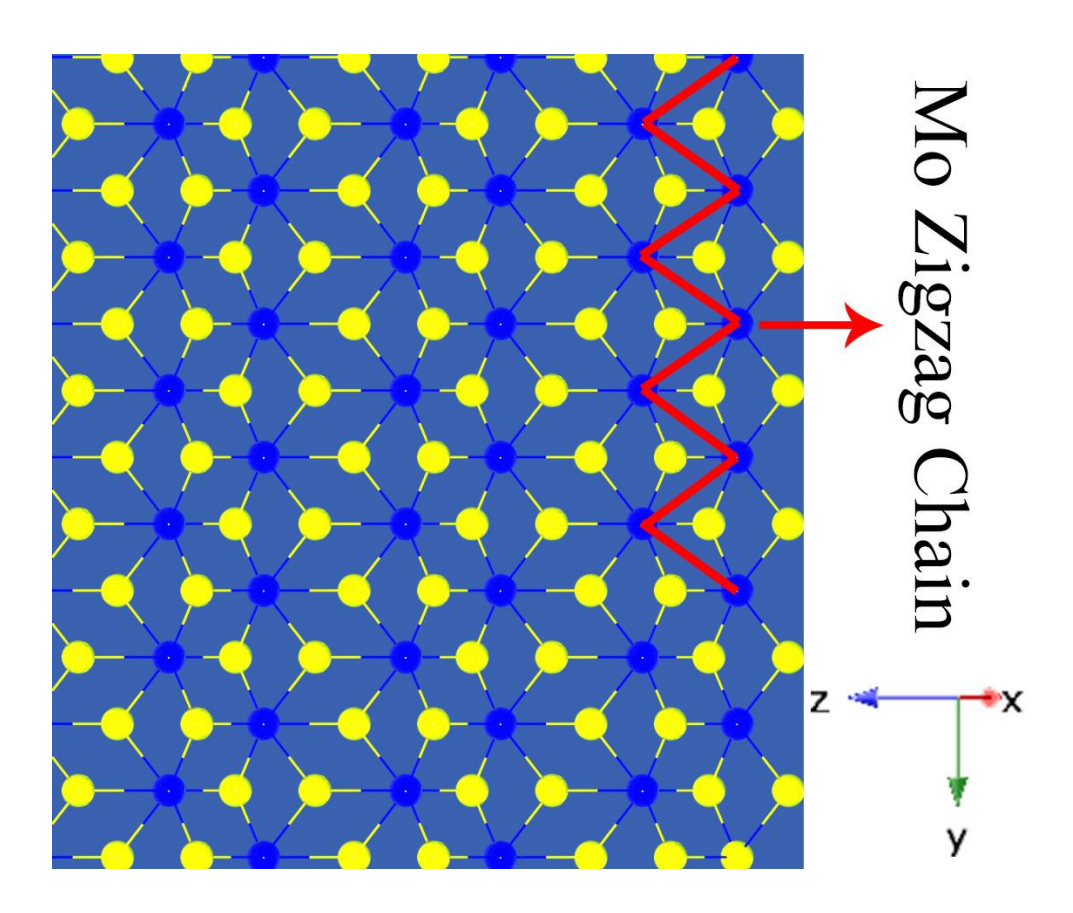


Figure 3.9: In-plane lattice structure of 1T' MoS₂ showing distinct Mo zigzag chains.

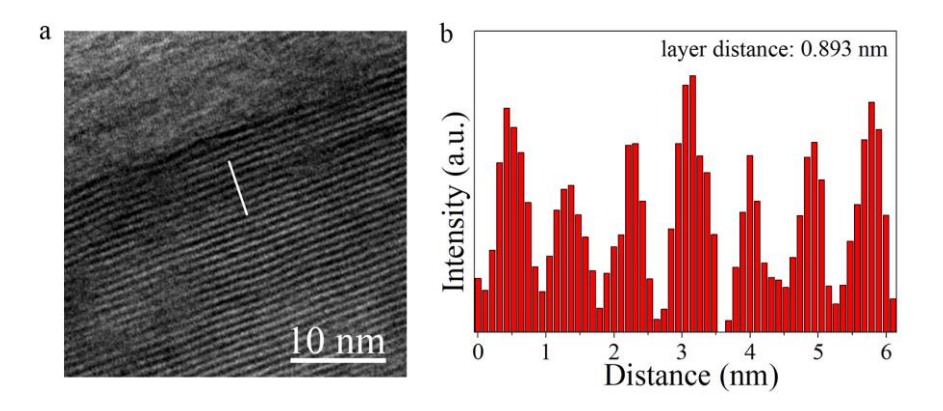


Figure 3.10: (a) High-resolution cross-sectional TEM image. (b) Brightness profile along the white line in a.



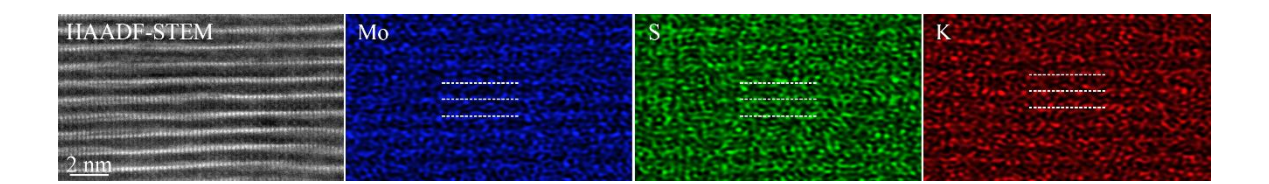


Figure 3.11: HAADF-STEM image and EDS mapping of Mo, S, and K.

An additional SAED pattern of K₂S-intercalated 1T' MoS₂, prepared in this study, is presented in Figure 3.12. The pattern reveals a single set of diffraction spots, corresponding to the distorted octahedral coordination of the 1T' MoS₂ structure, which differs from the hexagonal pattern characteristic of the 2H phase. This observation confirms that, at least in the tested region, the sample is a single crystal of 1T' MoS₂. If the sample were a mixture of 1T' and 2H phases, overlapping diffraction patterns would be observed. Thus, this result provides another evidence that the sample is nearly 100% pure 1T' phase.

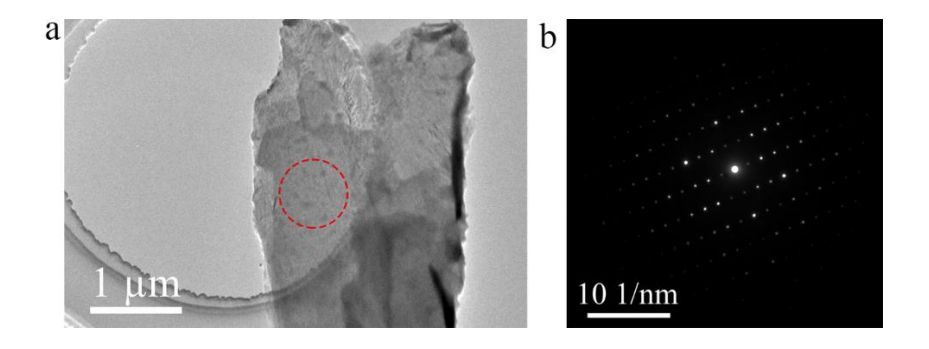


Figure 3.12: An additional SAED test result of K₂S-intercalated 1T' MoS₂. (a) TEM image of a piece of K₂S-intercalated 1T' MoS₂ flake. (b) SAED pattern acquired from red circle area shown in a.

3.4 Synthesis and Characterization of Na₂S, Li₂S-intercalated 1T' MoS₂

3.4.1 Synthesis Process

(a) Synthesis of Na₂S, Li₂S-intercalated 1T' MoS₂ powder



A three-zone furnace equipped with a one-meter-long quartz tube was employed for the direct synthesis of 1T' MoS2, as illustrated in Figure 3.1, which is same as the equipment for K₂S-intercalated 1T' MoS₂ synthesis. To ensure accurate synthesis, it is essential to use a completely clean quartz tube with no residual substances, particularly sulfur, which may remain from prior use. A new and clean quartz tube was utilized for each synthesis in this work. Sulfur powder (10 g) was loaded into an alumina boat, on the upstream end of the tube (heating zone 1). The sulfur acted as excess reagent and covered the bottom of cuboid alumina boat (bottom area: 910 mm²) throughout the synthesis process, ensuring uniform supply of sulfur by evaporation. Na₂MoO₄ or Li₂MoO₄ powder (60 mg) was positioned in the downstream end of the tube (heating zone 3), evenly distributed on a sapphire substrate (area: 2 X 2 cm²) on top of an alumina boat, while the middle heating zone 2 was left empty. Before starting the synthesis, the tube was evacuated to remove air and then purged with argon until atmospheric pressure was restored. During the process, argon gas was flowed at 35 sccm, with hydrogen added at 15 sccm, maintaining atmospheric pressure. Zones 2 and 3 were then heated with a rate of 15 °C min⁻¹ to 650 °C for Na₂S-intercalated 1T' MoS₂ synthesis or 700 °C for Li₂S-intercalated 1T' MoS₂ synthesis, while zone 1 was kept at room temperature. Once zones 2 and 3 reached 650 °C (Na₂S-intercalated 1T' MoS₂ synthesis) or 700 °C (Li₂S-intercalated 1T' MoS₂ synthesis), zone 1 was heated to 135 °C at 30 °C min⁻¹, ensuring controlled sulfur vaporization. This step prevented premature sulfur release and undesired reactions at temperatures below the growth threshold. If a quartz tube is reused, it must be thoroughly cleaned to avoid residual sulfur vaporizing during heating, which could lead to undesirable low-temperature reactions. The temperatures in zones 2 and 3 were maintained at 650 °C (Na₂S-intercalated 1T' MoS₂ synthesis) or 700 °C (Li₂S-intercalated 1T' MoS₂ synthesis) for 4 hours, while zone 1 was held at 135 °C. Afterward, the furnace cooled down naturally to room temperature. The sample was retrieved after complete cooling, yielding Na₂S-intercalated 1T' MoS₂ (or Li₂S-intercalated



1T' MoS₂) without requiring any post-treatment.

(b) Sputtering Deposition of Na₂MoO₄ Film and Na₂S-intercalated 1T' MoS₂ Nanosheets Synthesis

Na₂MoO₄ film was grown on a sapphire substrate by sputtering deposition (sputtering target: Na₂MoO₄, 50 W, 600 s, 20 sccm Ar/10 sccm O₂). Then the Na₂MoO₄ film replaced the Na₂MoO₄ powder and the other process steps were same as the above-described Na₂S-intercalated 1T' MoS₂ powder synthesis. After that, the Na₂S-intercalated 1T' MoS₂ nanosheets on sapphire substrate were obtained.

3.4.2 Characterization Results

(a) Na₂S, Li₂S-intercalated 1T' MoS₂ powder

The Na₂S-intercalated 1T' MoS₂ exhibits the same Raman spectrum as the K₂S-intercalated 1T' MoS₂, as shown in Figure 3.13, confirming its 1T' phase purity. Similarly, the Li₂S-intercalated 1T' MoS₂ displays a comparable Raman spectrum (Figure 3.14); however, the appearance of the E_{2g} Raman peak, associated with the 2H MoS₂ phase, is observed. This is likely due to the high reactivity of lithium compared to sodium and potassium, which may cause it to react with air when the sample is exposed, partially transforming it to the 2H phase. Despite this, the Na₂S-intercalated 1T' MoS₂, like the K₂S-intercalated 1T' MoS₂, demonstrates excellent crystal quality and phase purity. Further details on the TEM and XPS results are discussed below.



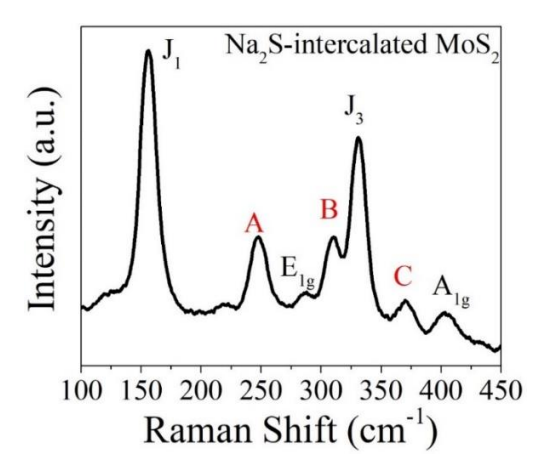


Figure 3.13: Raman spectrum of Na₂S-intercalated MoS₂.

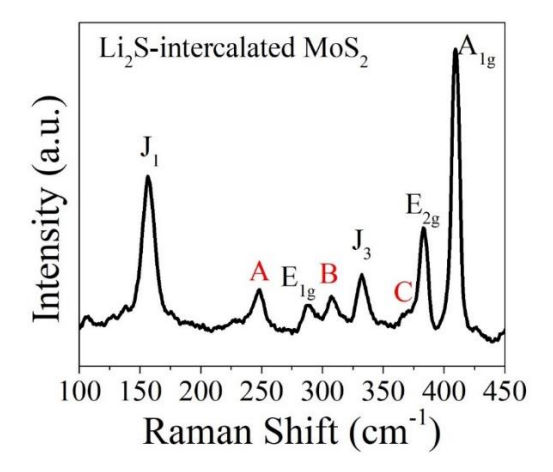


Figure 3.14: Raman spectrum of Li₂S-intercalated MoS₂.

TEM characterization has been performed to examine the lattice structure of Na₂S-intercalated 1T' MoS₂, as shown in Figure 3.15a-c. The distinct superstructural feature of the 1T' phase, namely the Mo zigzag chains, is clearly visible in the high-resolution TEM image (Figure 3.15c). The SAED pattern (inset in Figure 3.15b) confirms the distorted octahedral coordination characteristic of the 1T' MoS₂ structure. As shown in Figure 3.15d-g, EDS mapping provides evidence of the presence of Mo and S, as well as Na, which originates from the intercalation of "Na₂S". These results further confirm that the synthesized sample possesses the 1T' phase MoS₂ structure.



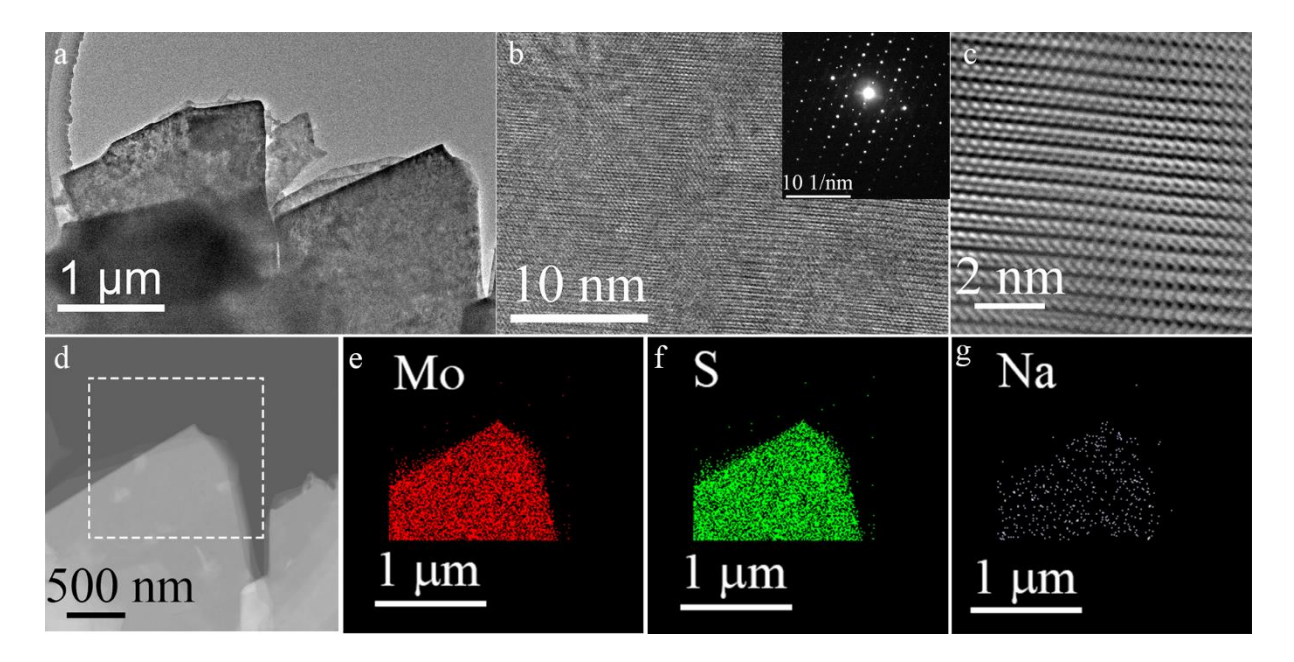


Figure 3.15: TEM characterization of Na₂S-intercalated 1T' MoS₂. (a) TEM and (b) HRTEM images of Na₂S-intercalated 1T' MoS₂, respectively. Inset in b: SAED pattern of Na₂S-intercalated 1T' MoS₂. (c) FFT filtered images of b. (d) Dark-field STEM image of Na₂S-intercalated 1T' MoS₂. Elemental mapping images of (e) Mo, (f) S, and (g) Na, respectively, acquired from rectangular dot box in d.

The Mo 3d XPS spectrum (Figure 3.16a) reveals that the Mo 3d_{5/2} and Mo 3d_{3/2} peaks have lower binding energies compared to those of 2H MoS₂, closely matching the binding energies of intrinsic 1T' MoS₂.¹⁶⁸ The fitting results show only one set of Mo 3d XPS peaks, with the fitting curve perfectly aligning with the experimental data, confirming that the Na₂S-intercalated 1T' MoS₂ is nearly 100% phase pure. Similar to the K₂S-intercalated 1T' MoS₂, the S 2p XPS spectrum (Figure 3.16b) displays two sets of peaks: one corresponding to 1T' MoS₂ and the other to the intercalated Na₂S. The presence of Na is further confirmed by the Na 1s XPS spectrum (Figure 3.16c).



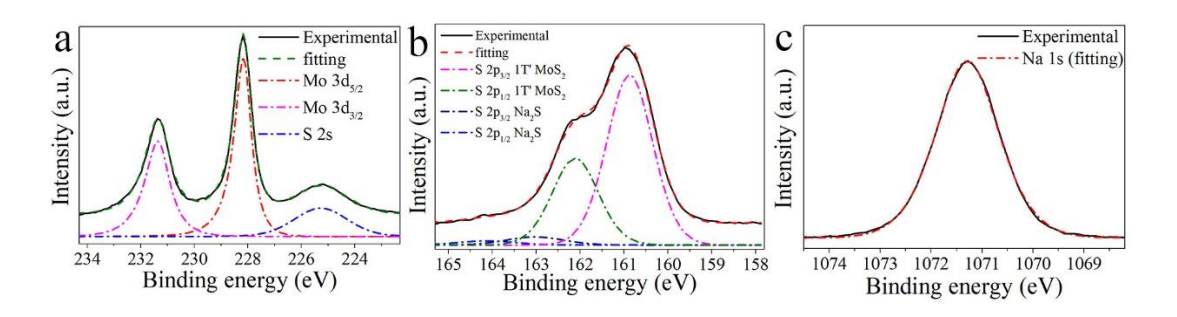


Figure 3.16: XPS spectra of Na₂S-intercalated 1T' MoS₂. Experimental and fitted XPS (a) Mo 3d and S 2s, (b) S 2p, and (c) Na 1s spectra of Na₂S-intercalated 1T' MoS₂, respectively.

(b) Na₂S-intercalated 1T' MoS₂ Nanosheets

Figure 3.17a displays an optical image of Na₂S-intercalated 1T' MoS₂ nanosheets, which have a strip-like morphology. According to the AFM height profile in Figure 3.17b, the thinnest strip has a thickness of approximately 12.43 nm. Figure 3.17c is the Raman spectrum of Na₂S-intercalated 1T' MoS₂ nanosheets. The characteristic Raman peaks of J₁ and J₃ are represented with the absence of the defect-related Raman peak J₂^{97,115,168,169}, which is usually seen in samples prepared via solution-phase intercalation methods. Three additional Raman peaks (labeled A, B, and C) associated with the intercalation are observed.



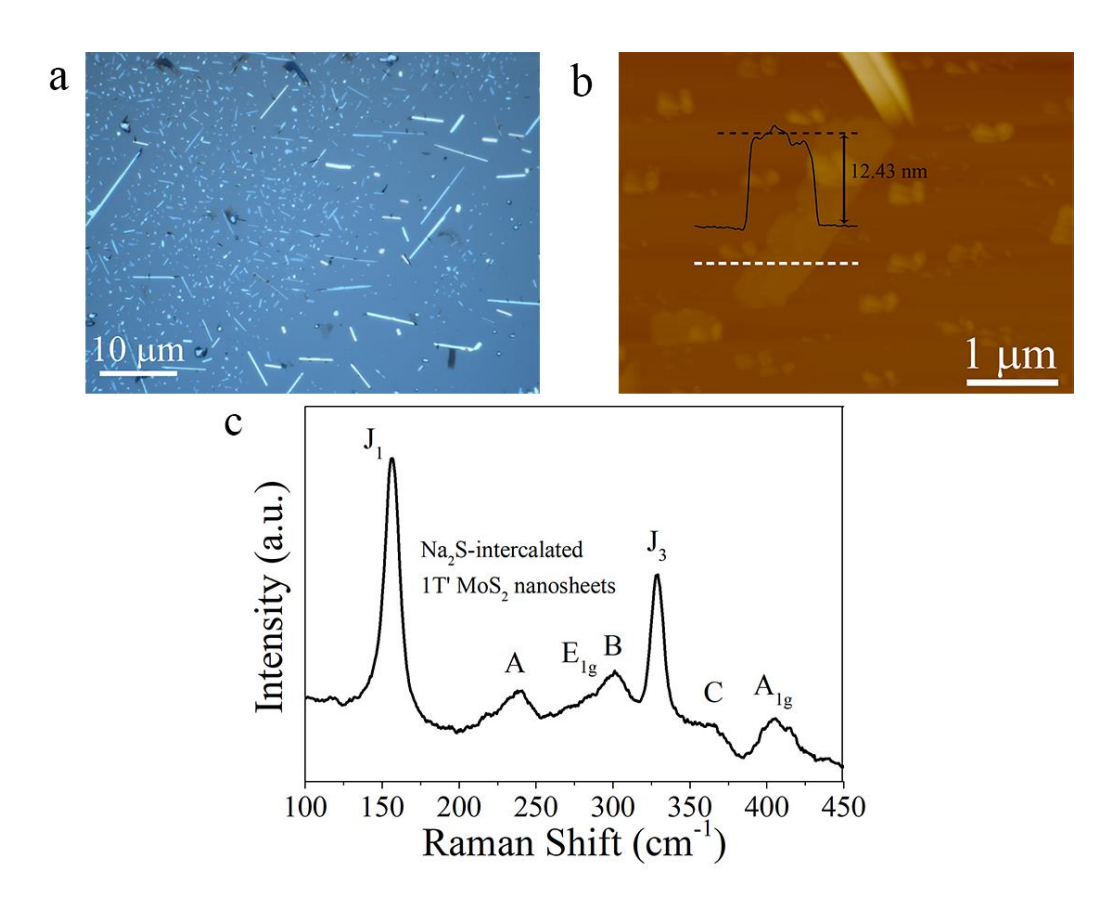


Figure 3.17: (a) Optical image of Na₂S-intercalated 1T' MoS₂ nanosheets. (b) AFM image of Na₂S-intercalated 1T' MoS₂ nanosheets and height profile along white dot line. (c) Raman spectra of Na₂S-intercalated 1T' MoS₂ nanosheets.

3.5 Synthesis and Characterization of Na₂Se, K₂Se-intercalated 1T' MoSe₂

3.5.1 Synthesis Process

It is highly similar to the synthesis of Na₂S-intercalated and K₂S-intercalated 1T' MoS₂ described above. The sulfur powder is replaced with selenium powder, and the heating temperature is 230 °C.



3.5.2 Characterization Results

The Raman spectrum of the as-synthesized K₂Se-intercalated MoSe₂ is shown in Figure 3.18. It exhibits J₁, J₂, J₃, and E_{2g}¹ Raman peaks, consistent with those of intrinsic 1T' MoSe₂^{169,170}. Additionally, Raman peaks A and B, attributed to intercalation, are observed. The inset in Figure 3.18 displays an optical image of K₂Se-intercalated MoSe₂ flakes on a sapphire substrate, with the size of around 50 μm.

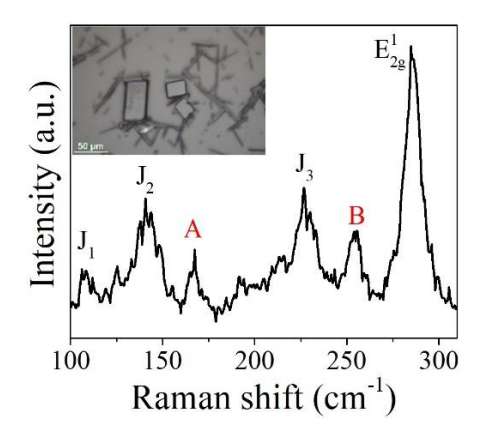


Figure 3.18: Raman spectrum of K₂Se-intercalated MoSe₂. Inset: optical image of K₂Se-intercalated MoSe₂.

Figure 3.19 presents the Raman spectrum of Na₂Se-intercalated MoSe₂, with peak positions resembling those of K₂Se-intercalated MoSe₂. Similarly, Raman peaks A and B arise from intercalation, while the remaining peaks correspond closely to those of intrinsic 1T' MoSe₂^{169,170}. The inset of Figure 3.19 shows an optical image of Na₂Se-intercalated MoSe₂ flakes, highlighting their morphology.



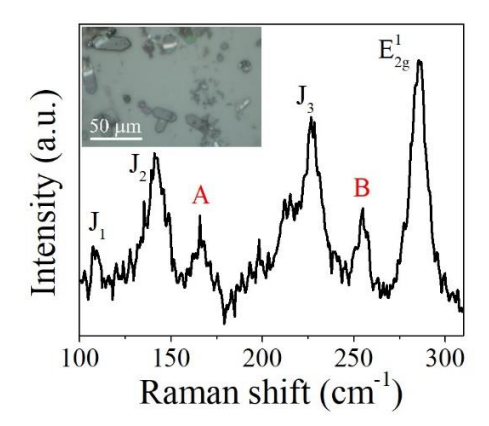


Figure 3.19: Raman spectrum of Na₂Se-intercalated MoSe₂. Inset: optical image of Na₂Se-intercalated MoSe₂.

TEM analysis was performed to characterize the structure of K₂Se-intercalated 1T' MoSe₂. The HRTEM image in Figure 3.20b, c reveals the characteristic 1T' MoSe₂ structure. The SAED pattern shown in the inset of Figure 3.20b indicates the 1T' MoSe₂ structure. Elemental mapping was conducted in dark-field STEM mode, with the results shown in Figure 3.20d-g. The distributions of Mo, Se, and K elements align with the dark-field STEM image of the flake, indicating uniform element distribution.

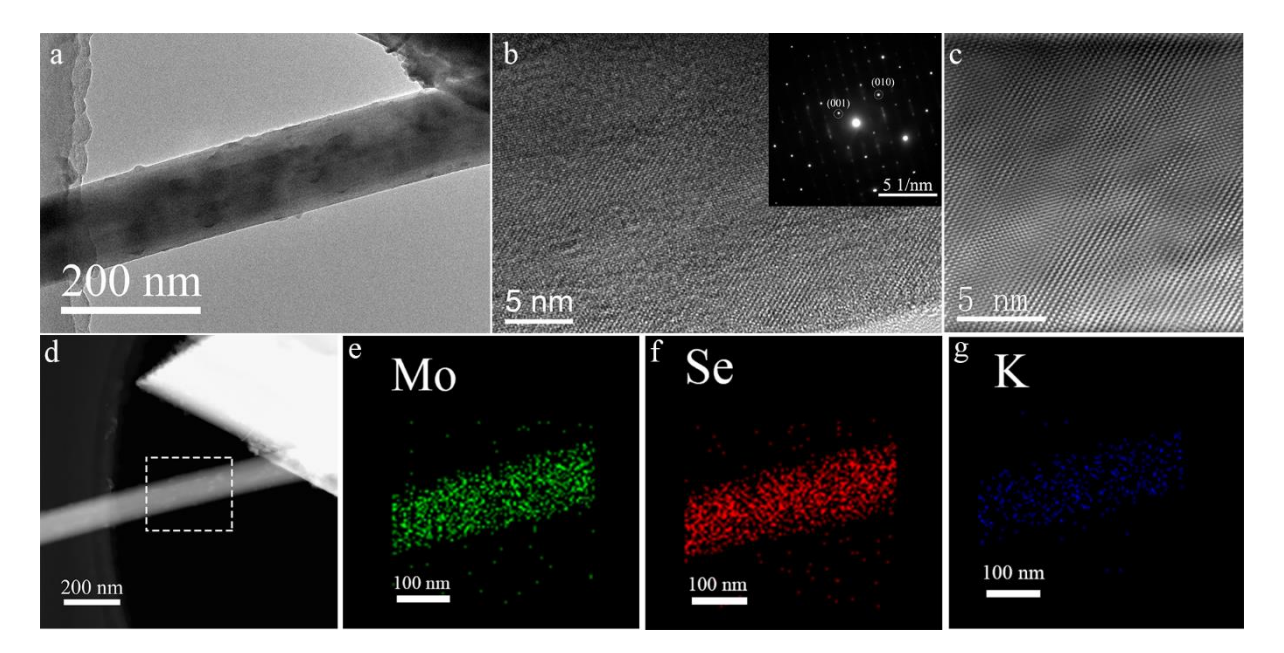


Figure 3.20: TEM characterization of K₂Se-intercalated 1T' MoSe₂. (a) TEM and (b)



HRTEM images of K₂Se-intercalated 1T' MoSe₂, respectively. Inset in b: SAED pattern of K₂Se-intercalated 1T' MoSe₂. (c) FFT filtered images of b. (d) Dark-field STEM image of K₂Se-intercalated 1T' MoSe₂. Elemental mapping images of (e) Mo, (f) Se, and (g) K, respectively, acquired from rectangular dot box in d.

3.6 Synthesis and Characterization of K_2 Te-intercalated 1T' $MoTe_2$

3.6.1 Synthesis Process

It is almost the same as the synthesis of K₂S-intercalated 1T' MoS₂ demonstrated in Section 3.3.1. Sulfur powder was replaced with tellurium powder, of which the heating temperature is 500 °C.

3.6.2 Characterization Results

The Raman spectrum of the as-synthesized K₂Te-intercalated MoTe₂ is shown in Figure 3.21. It features A_g and B_g Raman peaks, identical to those of intrinsic 1T' MoTe₂¹⁷¹. Additionally, Raman peak A is observed, which originates from intercalation. The inset in Figure 3.21 displays an optical image of K₂Te-intercalated MoTe₂ flakes on a sapphire substrate.



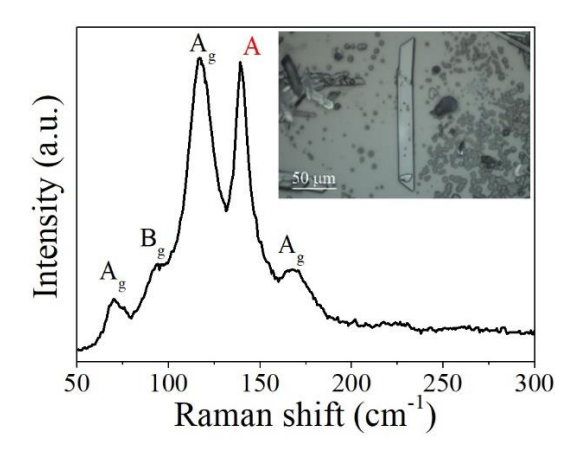


Figure 3.21: Raman spectrum of K₂Te-intercalated MoTe₂. Inset: optical image of K₂Te-intercalated MoTe₂.

TEM analysis was conducted to investigate the lattice structure of K₂Te-intercalated 1T' MoTe₂, as presented in Figure 3.22a-c. The FFT filtered image of HRTEM is shown in Figure 3.22c, which distinctly reveals the superstructure characteristic of the 1T' MoTe₂. The SAED pattern (inset in Figure 3.22b) further confirms the distorted octahedral coordination typical of the 1T' MoTe₂ structure. Figure 3.22d-g show EDS mapping results, providing evidence of the presence of Mo and Te elements, along with K, which originates from the intercalation of "K₂Te." These findings confirm that the synthesized sample possesses the 1T' phase MoTe₂ structure.



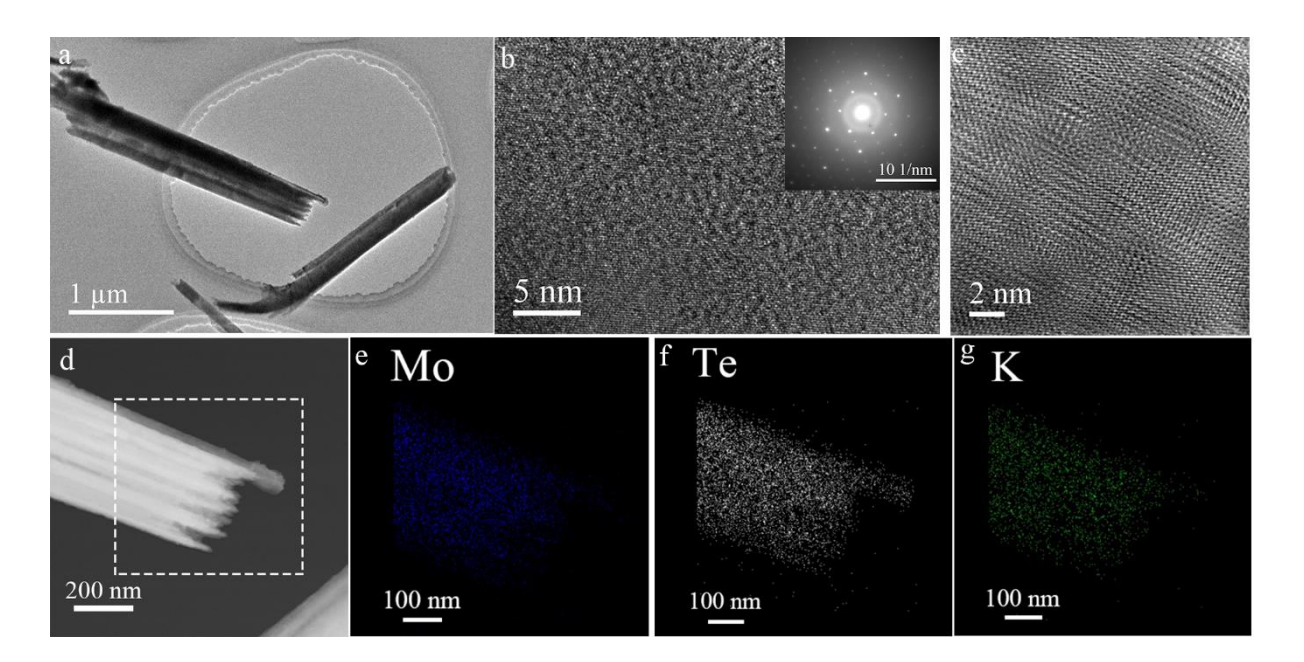


Figure 3.22: TEM characterization of K₂Te-intercalated 1T' MoTe₂. (a) TEM and (b) HRTEM images of K₂Te-intercalated 1T' MoTe₂, respectively. Inset in b: SAED pattern of K₂Te-intercalated 1T' MoTe₂. (c) FFT filtered images of b. (d) Dark-field STEM image of K₂Te-intercalated 1T' MoTe₂. Elemental mapping images of (e) Mo, (f) Te, and (g) K, respectively, acquired from rectangular dot box in d.

3.7 Self-intercalation Method

This chapter demonstrates a self-intercalation method to obtain intercalated 1T' TMDs with high phase purity, high crystal quality, and high productivity. Utilizing the structure similarity between alkali metal molybdates and intercalated 1T' TMDs to achieve self-intercalation has been firstly proposed by this thesis.

In Section 3.3, the K₂S-intercalated 1T' MoS₂ was successfully synthesized by self-intercalation method. Self-intercalation means the intercalation is done spontaneously. The intercalated 1T' structure itself is thermodynamically stable. The intercalated 1T' TMDs are directly synthesized rather than built by forcing intercalants to insert into layer gap. Self-intercalation could avoid crystal defects formation during intercalation. As



discussed in Chapter 2, the defects formation is unavoidable during the insertion of intercalants using n-butyllithium treatment method, alkali metal deposition method, or electrochemical intercalation method. Moreover, these methods are localized, which leads to uneven intercalation and low phase purity. During the synthesis via proposed self-intercalation method, there is no solution-phase intercalation. The products are directly grown without any post treatments, so the typical defects caused by solution-phase intercalation methods do not appear, thus leading to phase purity and high crystal quality.

The selection of intercalant is also an important issue. The current intercalation methods usually use alkali metals as intercalants. However, the alkali metals, such as Li, Na, K, are very active. They react with oxygen, water, ethanol and many others. The active intercalants would definitely cause additional stability problems besides the stability of 1T' phase itself. The self-intercalation method demonstrated by this thesis can achieve A₂C intercalation (A=Li, Na, K; C=S, Se, Te), which are much more stable than alkali metals. The stability of whole system would be greatly increased, and it makes applications more reliable.

To achieve the self-intercalation, the crystal similarity is utilized. The intercalated 1T' TMDs, such as 1T' MoS₂, 1T' MoSe₂, belong to monoclinic crystal system and *C2/m* space group. Interestingly, potassium molybdate (K₂MoO₄), sodium molybdate (Na₂MoO₄), lithium molybdate (Li₂MoO₄) also belong to the same crystal system and space group. Figure 3.23a shows the structure of potassium molybdate, and the schematic of self-intercalation and synthesis, the atomic model of K₂S-intercalated 1T' MoS₂ is given in Figure 3.23b. There are layer-like distributions of molybdenum atoms and potassium atoms in potassium molybdate, corresponding to layered 1T' MoS₂. Because the source of intercalated potassium element is potassium molybdate itself, this self-intercalation method can achieve uniform intercalation stoichiometrically and spatially within interlayer. It is worthy to note that density functional theory (DFT) calculation results (Chapter 4) indicate K₂S intercalation lowers the formation energy of 1T' MoS₂, which makes metastable 1T'



phase thermodynamically stable and allows 1T' MoS₂ synthesis at high temperatures.

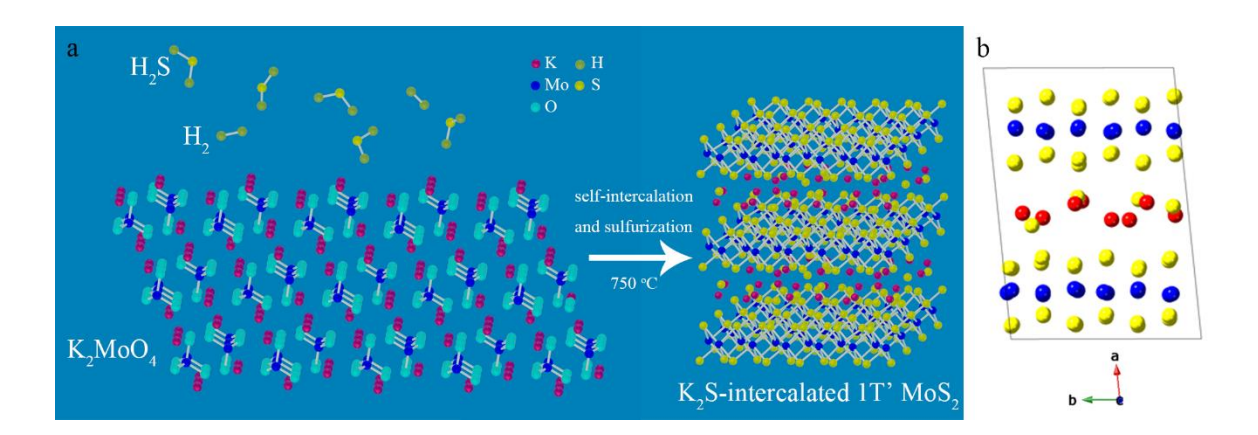


Figure 3.23: (a) Schematic of self-intercalation and synthesis. (b) Atomic model of K₂S-intercalated 1T' MoS₂.

It is found that self-intercalation of K₂S only happens at around 750 °C, and low-temperature reactions lead to phase impurity and 2H phase formation. So, the sulfur supply is carefully controlled to make the reaction only happen at 750 °C, avoiding any low-temperature reaction. Additionally, our attempts to prepare K₂S-intercalated 1T' MoS₂ at reduced temperatures were unsuccessful, suggesting that K₂S requires sufficient energy to effectively position itself between the layers of 1T' MoS₂. The temperature is the key factor in the self-intercalation process.

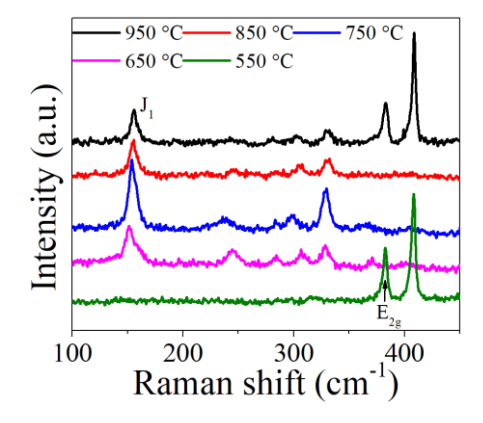


Figure 3.24: Raman spectra of samples with growth temperature from 550 °C to 950 °C.



To investigate the influence of reaction temperature on phase structure, the samples were grown at 550 °C, 650 °C, 750 °C, 850 °C, and 950 °C, while keeping other parameters same. The Raman spectra of the products are given in Figure 3.24. The sample with growth temperature of 750 °C has strongest 1T' phase characteristic Raman peak, J₁. With the decrease in growth temperature, J₁ peak disappear and the 2H phase characteristic Raman peak can be observed at 550 °C. The low-temperature reaction cannot provide K₂S enough energy to intercalate into the layered MoS₂, thus leading to 2H phase formation. With the increase in growth temperature, the intensity of J₁ Raman peak drops and the product is the mixture of 1T' and 2H phase MoS₂ at 950 °C. The potassium sulfide melts at 840 °C, and the intercalated K₂S would have similar property with potassium sulfide. The temperature above 850 °C could release K₂S from interlayer of MoS₂ by melting or vaporization, which would destroy the intercalation structure and cause formation of 2H phase, thus lowering phase purity. Overall, 750 °C is most suitable for K₂S-intercalated 1T' MoS₂ growth. This result suggests that the temperature is the critical point of self-intercalation method, which requires a temperature control to avoid phase impurity.

The influence of K₂S intercalation on metallic conduction behavior of 1T' MoS₂ is another issue worthy attention. It has been found that the intercalation of K₂S does not change the metallic conduction behavior of intrinsic 1T' MoS₂. The experimental details are shown below.

A piece of K₂S intercalated 1T' MoS₂ flake was transferred on gold electrodes which were fabricated on SiO₂/Si substrate by conventional photolithography process. The Figure 3.25a shows its optical image. The output characteristic curve and transfer characteristic curve were measured by a semiconductor analyzer (Keysight B1500A) with a probe station (LakeShore). As shown in Figure 3.25b, the linear output characteristic curve suggests there is Ohmic contact between gold electrodes and K₂S intercalated 1T' MoS₂. The transfer characteristic curve (Figure 3.25c) shows no gate-controlled drain current, which also



confirms the K₂S intercalated 1T' MoS₂ is metallic, same as the intrinsic 1T' MoS₂.

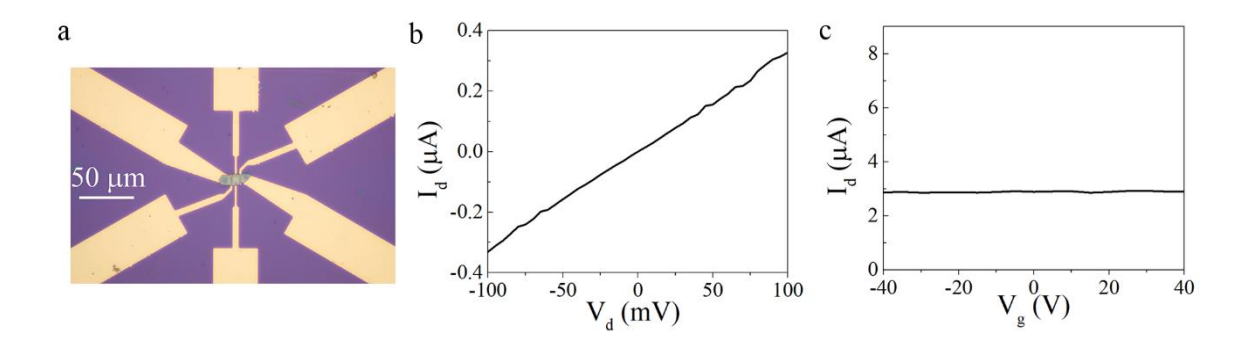


Figure 3.25: (a) Optical image of K₂S intercalated 1T' MoS₂ transferred on gold electrodes. (b) Output characteristic curve of K₂S intercalated 1T' MoS₂. (c) Transfer characteristic curve of K₂S intercalated 1T' MoS₂.

3.8 Summary

A self-intercalation method for synthesizing intercalated 1T' TMDs has been demonstrated. Using this method, K₂S-intercalated 1T' MoS₂ was successfully synthesized. Characterization results confirm that the material is nearly 100% pure 1T' phase, with high crystal quality. The as-synthesized sample retains the same in-plane structure as intrinsic 1T' MoS₂, with K₂S acting as an intercalant in the interlayer gap. This unique structure not only preserves the original in-plane structure of 1T' MoS₂ but also stabilizes the entire system through intercalation. Importantly, this method employs inexpensive reagents, a simple tube furnace, and a short processing time of just a few hours, with no need for post-treatment. As a result, it is suitable for large-scale production, which is crucial for industrial and commercial applications. Moreover, this method is adaptable to various TMDs. In addition to K₂S-intercalated 1T' MoS₂, 1T' MoS₂ intercalated with Li₂S and Na₂S have also been synthesized, along with K₂Se-intercalated 1T' MoSe₂, Na₂Se-intercalated 1T' MoSe₂, and K₂Te-intercalated 1T' MoTe₂, showcasing the versatility of the method. This proposed synthesis method would allow an easier access to the study and applications of 1T' phase



TMDs.



Chapter 4

Stability and Stabilization Mechanism



4.1 Introduction

The properties of transition metal dichalcogenides (TMDs) depends on the crystalline structure. The most well-known Group VI TMDs, such as MoS2, mostly are thermodynamically stable in 2H phase. The polymorphs of 1T, 1T', 1T", or 1T" phases represent distinct structures and unique properties which make them promising candidates for various applications. However, the formation energy of these phases is higher than 2H phase, therefore they are metastable and tend to transition to 2H phase gradually. Moreover, they transform to stable 2H phase at a relatively low temperature, for example, the 1T' MoS₂ experiences a phase transition to 2H phase over 100 °C. The low stability is an intrinsic drawback of 1T' phase, which was attempted to solve by doping or applying strain. 109,125 Unfortunately, these methods would cause defects and not suitable for mass production. The stabilization by intercalation engineering has drawn more and more attention, as it has potential to lower system energy while retaining intrinsic in-plane 1T' phase structure. A molten-metal-assisted intercalation method was proposed by Park et al. to stabilize 1T' TMDs. 122 Although the intercalated 1T MoS2 can sustain 350 °C, the synthesized samples showed a low phase purity. It is reported that the lithium was directly deposited on 2H MoS₂ and the subsequent heating in hydrogen lead to formation of LiH-intercalated 1T' MoS₂. 123 This intercalated structure represented 3-moth stability in air and 5-hour stability in water, the outcome fell short of expectation and the surface degradation could not be avoided. To fully explore and harness their potential, it is crucial to synthesize metastable-phase TMDs with high phase purity and stabilization.

The stabilization of 1T' TMDs is highly desired. In chapter 3, the synthesis and characterization of various 1T' TMDs with alkali metal chalcogenides intercalant are demonstrated, and the typical K₂S-intercalated 1T' MoS₂ has been especially characterized and studied. The high crystal quality and phase purity have been confirmed by



characterization results. Importantly, the issue about stability of 1T' TMDs acquires more attention due to the reliability greatly influences the applications performance, considering that many 1T' TMDs are intrinsically metastable. In this chapter, the stability of K₂S-intercalated 1T' MoS₂ under different conditions were tested, including temperature, solvents, thickness, or aging. The synthesized K₂S-intercalated 1T' MoS₂ represents excellent stability compared with the samples prepared by the previous work. The as-synthesized K₂S-intercalated 1T' MoS₂ can endure temperatures above 750 °C and remains stable in air, water, and ethanol, maintaining its stability even after one year of aging. The theory calculation was conducted with K₂S-intercalated 1T' MoS₂ model. The results show K₂S intercalation decrease the formation energy by N-doping and forming bonding with 1T' MoS₂, thus stabilizing the 1T' phase.

4.2 Stability

4.2.1 Temperature

The as-synthesized K₂S-intercalated 1T' MoS₂ exhibits remarkable stability in this study. The prepared sample demonstrates resistance to high temperatures. A differential scanning calorimetry (DSC) test, conducted within a temperature range of 50 °C to 380 °C, confirms that the K₂S-intercalated 1T' MoS₂ retains its phase, as shown in Figure 4.1a. Furthermore, the Thermogravimetric analysis (TGA) curve (Figure 4.1a) indicates that there is no weight loss. In contrast, the intrinsic 1T' MoS₂ undergoes a phase transition to the 2H phase at a relatively low temperature of 97 °C¹¹⁵.

To further assess thermal stability, the as-synthesized K₂S-intercalated 1T' MoS₂ was annealed at 750 °C immediately after synthesis and then characterized using Raman spectroscopy and X-ray photoelectron spectroscopy (XPS). The Raman spectrum (Figure



4.1b) shows no significant changes compared to the as-synthesized sample. The XPS spectra of Mo 3d and S 2s (Figure 4.1c) confirm that the sample retains its nearly 100% 1T' phase purity even after annealing at 750 °C. These results demonstrate that K₂S intercalation significantly enhances stability against high temperatures.

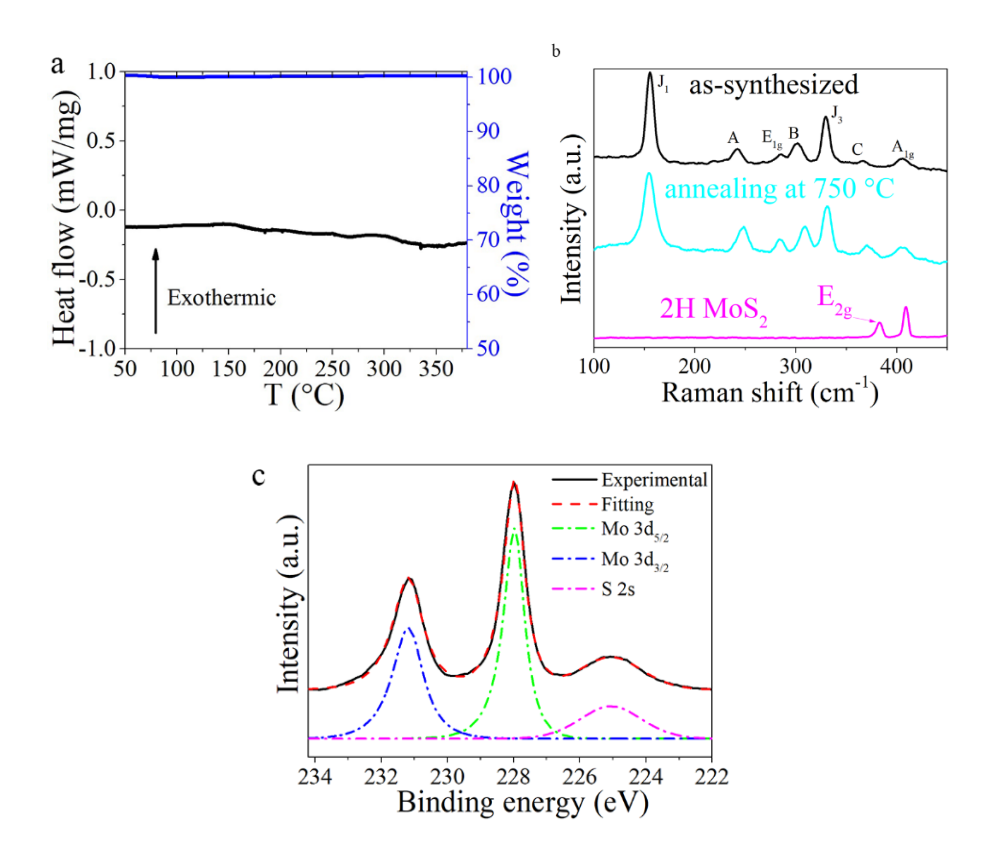


Figure 4.1: Thermal stability of K₂S-intercalated 1T' MoS₂. (a) TGA and DSC curves of K₂S-intercalated 1T' MoS₂ powder. (b) Raman spectra of as-synthesized K₂S-intercalated 1T' MoS₂ before and after annealed at 750 °C, and 2H MoS₂. (c) Experimental and fitted XPS Mo 3d and S 2s spectra of K₂S-intercalated 1T' MoS₂ powder after annealing at 750 °C.

4.2.2 Solvents and aging in air

The K₂S-intercalated 1T' MoS₂ also demonstrates stability against solvents. The samples were thoroughly washed with deionized water and ethanol, with no significant changes



observed in the Raman spectra (Figure 4.2). Scanning electron microscope (SEM) images and energy-dispersive X-ray spectroscopy (EDS) mapping (Figure 4.3) reveals the presence of potassium after washing, suggesting that the intercalated K₂S is not easily dissolved by water or ethanol. For comparison, the Raman spectrum of commercial 2H MoS₂ powder is included in Figure 4.2, where the E_{2g} peak characteristic of the 2H phase is marked. To evaluate aging stability, the as-synthesized samples were exposed to air at room temperature for one year, and no signs of degradation were observed, as shown by the Raman spectrum in Figure 4.2. These samples exhibit exceptional stability compared to 1T' MoS₂ prepared by other methods^{59,78,115,172}, which makes them promising materials for various practical applications.

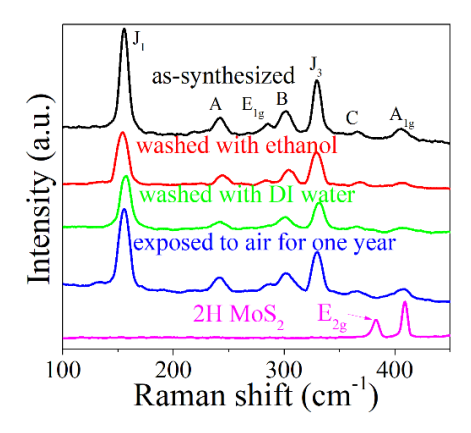


Figure 4.2: Raman spectra of as-synthesized K₂S-intercalated 1T' MoS₂, K₂S-intercalated 1T' MoS₂ washed with ethanol, washed with DI water, exposed to air for one year, and 2H MoS₂.



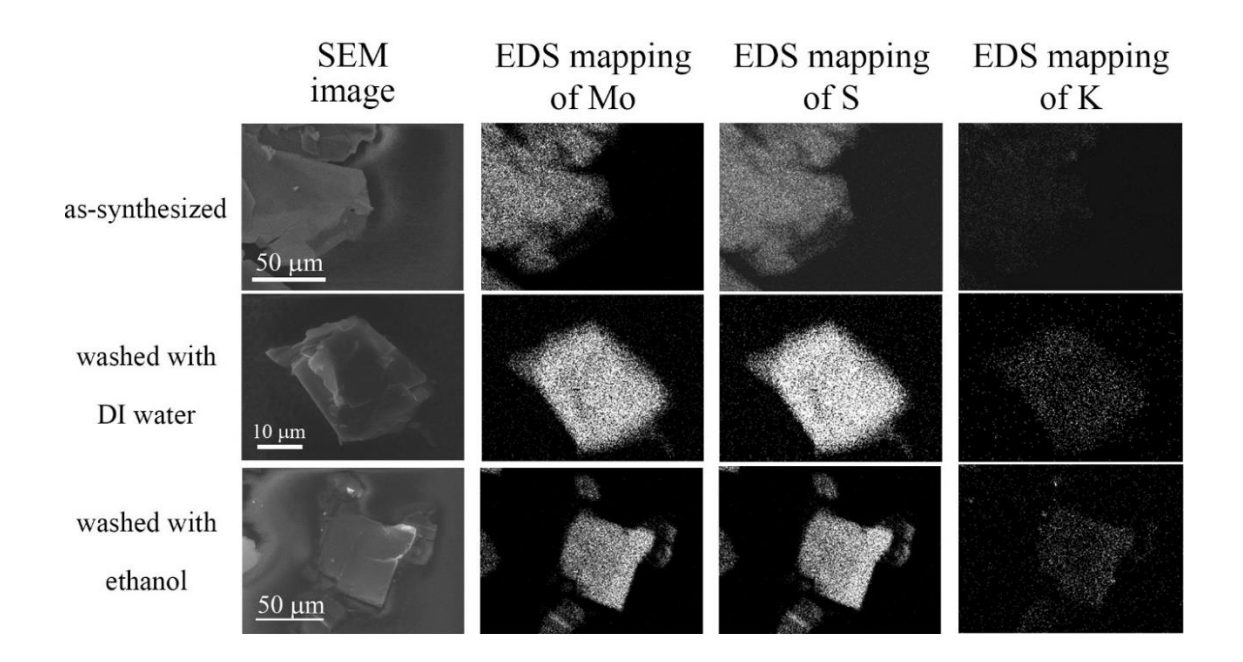


Figure 4.3: SEM images and EDS mapping results of as-synthesized K₂S-intercalated 1T' MoS₂ and K₂S-intercalated 1T' MoS₂ after washed with DI water and ethanol.

4.2.3 Thickness

Interestingly, the intercalation of K₂S can stabilize the 1T' MoS₂, which piqued our interest in exploring the relationship between flake thickness and stability. A thicker flake contains more intercalated K₂S, while a monolayer MoS₂ lacks sufficient space for intercalation. The synthesized K₂S-intercalated 1T' MoS₂ was exfoliated using tape, and the thickness was measured by Atomic force microscopy (AFM). It was observed by optical microscopy that thinner flakes tended to be more transparent. Two flakes, with thicknesses of 10 nm and 34 nm, were selected for further analysis. Their optical images are shown in Figure 4.4 and Figure 4.6, respectively. The corresponding Raman spectra of these flakes are presented in Figure 4.5a and Figure 4.7a, both of which retained the 1T' phase after tape exfoliation.

The flakes were then placed on a 100 °C hotplate in air for 30 minutes, and their Raman spectra were measured again, as shown in Figure 4.5b and Figure 4.7b. The 10-nm-thick



flake exhibited a phase transition, showing a mixture of the 1T' and 2H phases (indicated by the appearance of the E_{2g} Raman peak), while the 34-nm-thick flake showed no noticeable change in its Raman spectrum, retaining its 1T' phase. These results suggest that the intercalation-induced stabilization against high temperatures requires the flakes to be at least 10 nm thick. It is also noted that the thinnest flakes obtained by this synthesis method were 12.43 nm, as shown in Figure 3.17b.

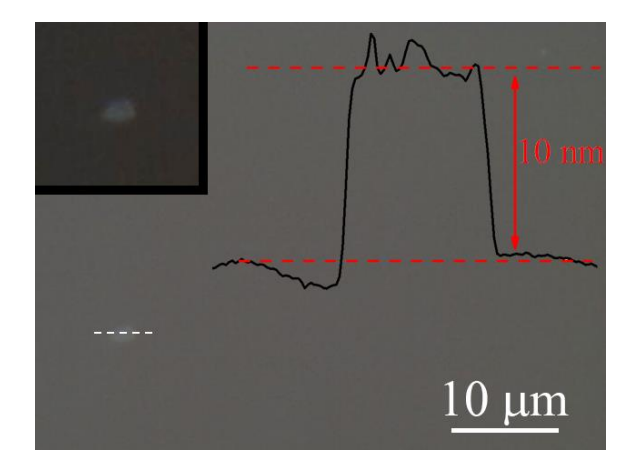


Figure 4.4: Optical image of 10-nm-thick K₂S-intercalated 1T' MoS₂ flake obtained by tape exfoliation and height profile along white dot line measured by AFM. Inset: the zoom-in image of K₂S-intercalated 1T' MoS₂ flake.

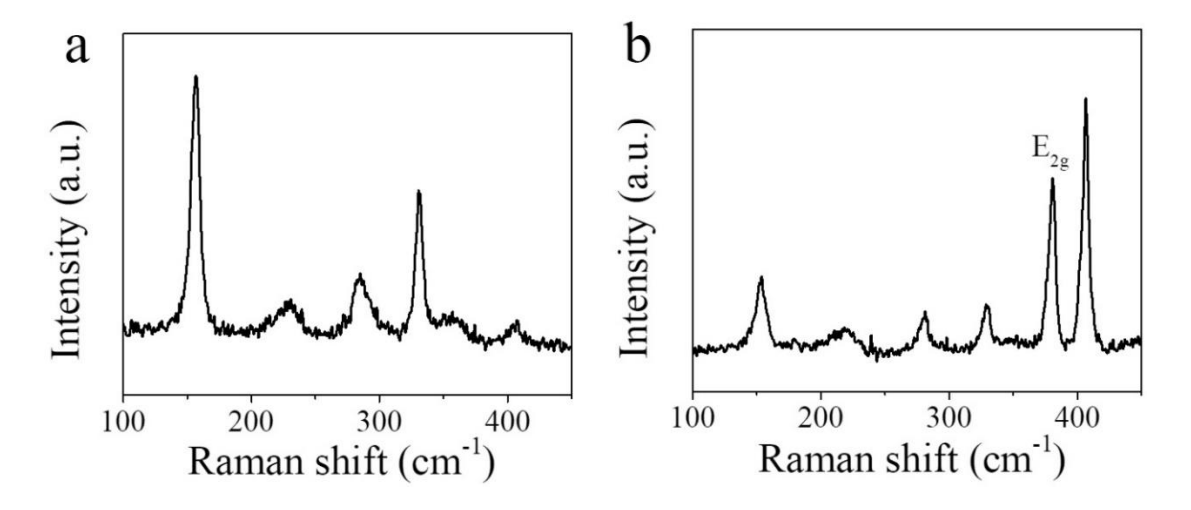


Figure 4.5: Raman spectra of 10-nm-thick K₂S-intercalated 1T' MoS₂ flake obtained by tape exfoliation. (a) Before 100 °C annealing. (b) After 100 °C annealing.



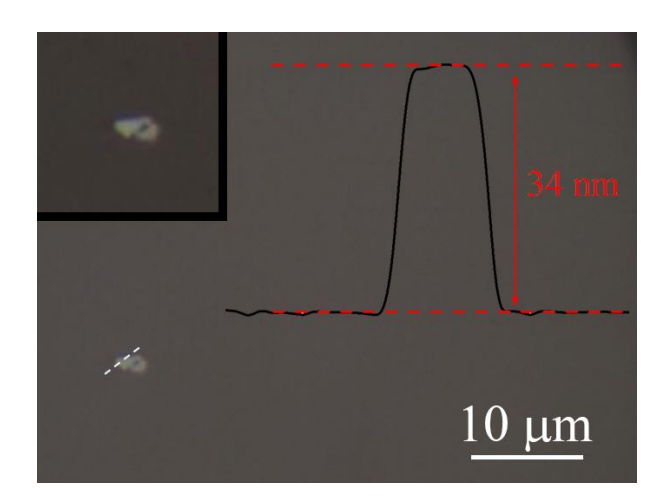


Figure 4.6: Optical image of 34-nm-thick K₂S-intercalated 1T' MoS₂ flake obtained by tape exfoliation and height profile along white dot line measured by AFM. Inset: the zoom-in image of K₂S-intercalated 1T' MoS₂ flake.

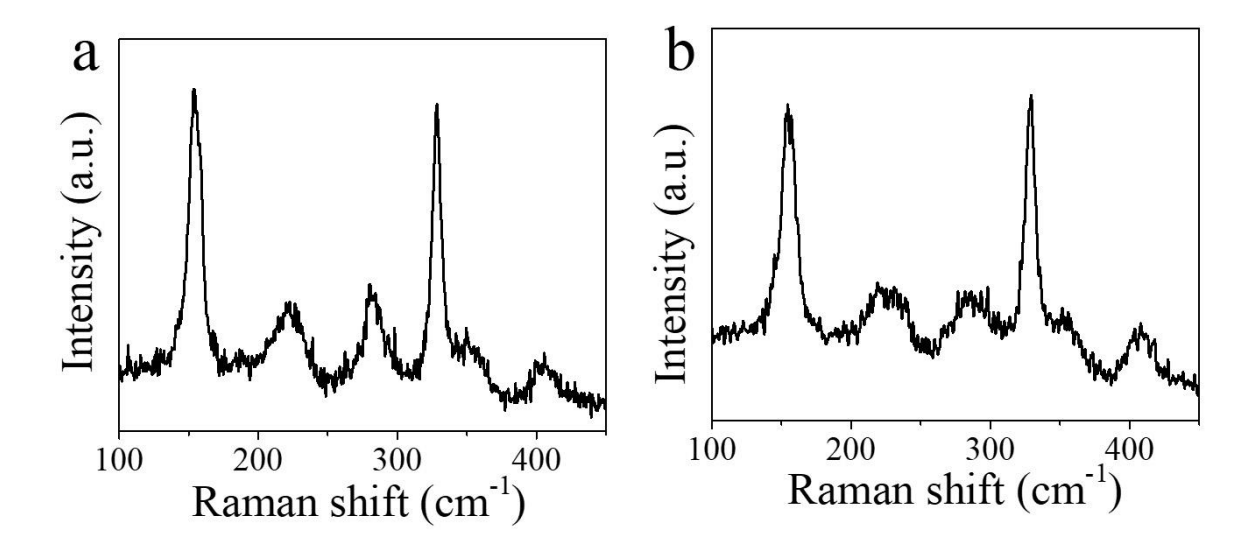


Figure 4.7: Raman spectra of 34-nm-thick K₂S-intercalated 1T' MoS₂ flake obtained by tape exfoliation. (a) Before 100 °C annealing. (b) After 100 °C annealing.

The thinner flakes require higher N-doping concentration to achieve stabilization. To stabilize them, higher concentration of intercalated K₂S is required. Decrease of the reaction time can reduce the vaporization of K₂S during the synthesis, thus increasing the ratio of K₂S.



4.3 Theoretical calculation

To investigate the influence of K₂S intercalation further, we conducted the calculation in the framework of the Density functional theory (DFT). The models of K₂S-intercalated 1T'- and 2H-MoS₂ were constructed to evaluate the influence of K₂S intercalation on the stability of MoS₂ with different phases.

DFT calculations were performed using the Vienna Ab initio Simulation Package (VASP) with projector augmented wave (PAW) pseudopotentials. 173,174 The Perdew–Burke–Ernzerhof (PBE) functional 175 was employed to approximate the exchange-correlation interaction, utilizing a plane-wave basis set with an energy cutoff of 450 eV. Van der Waals interactions were accounted using the Grimme-D3 scheme. 176 The Fermi-level smearing width was set to 0.05 eV for both geometry optimization and electronic structure calculations. The Brillouin zone was sampled with $5\times5\times5$ and $4\times16\times8$ Monkhorst-Pack k-point grids for K₂S cubic bulk and 1T'-MoS₂ bulk phases, respectively. Spin polarization was incorporated into all calculations, and model structures were optimized until force components were reduced below 0.05 eV/Å. The lattice constant of K₂S cubic bulk and 1T'-MoS₂ were calculated to be 7.39 Å and a = 12.39 Å, b = 3.20 Å, c = 5.76 Å, β = 114.7°, respectively, aligning well with reference data. 78,177

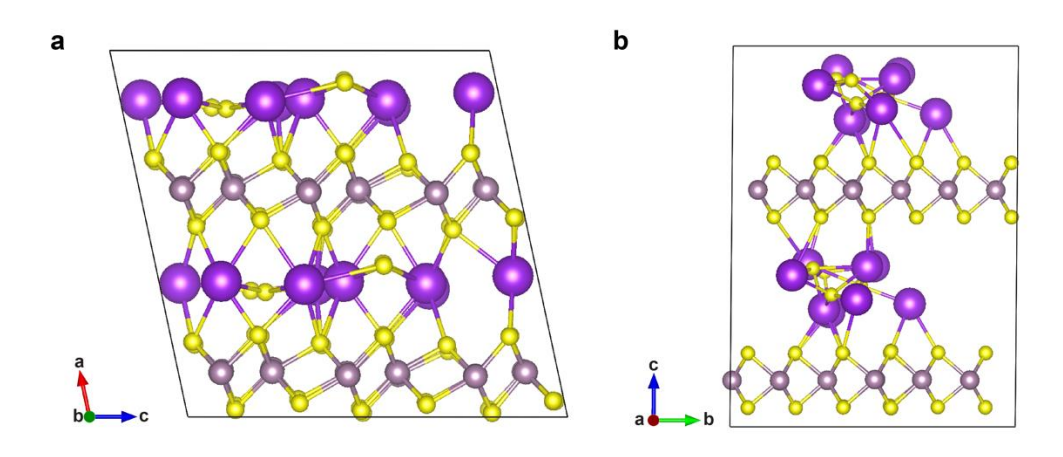




Figure 4.8: The K_2S -intercalated MoS_2 models. (a) 1T'- $(K_2S)_{x=0.22}MoS_2$ and (b) 2H- $(K_2S)_{x=0.17}MoS_2$ models.

To examine the structural stability of K₂S-intercalated MoS₂, two intercalation models were considered: K2S-intercalated 1T'- and 2H-MoS2. These models were constructed using supercells containing two layers each of MoS₂ and K₂S, arranged sequentially, with 132 and 168 atoms in the respective supercells. The Brillouin zone was sampled using 2×3×2 and 2×2×1 Monkhorst-Pack k-point grids for K₂S-intercalated 1T'- and 2H-MoS₂, respectively. Experimental results reveal that the interlayer distance of synthesized K2S-intercalated MoS2 extends from 5.88 Å (intrinsic 1T'-MoS₂) to 9.06 Å, an increase of about 3.2 Å. In comparison, K-intercalated MoS₂ exhibits a similar interlayer distance increase of about 2 Å. ¹²¹ Given that the K-K distance in the K₂S cubic bulk is approximately 3.7 Å, we hypothesize that the K₂S intercalation layer forms an approximate monolayer structure between MoS₂ layers, similar to the K intercalation layer in K-intercalated MoS₂. Previous theoretical studies have predicted K₂S to be stable as a 1T monolayer structure. 178 Considering this, models of K₂S-intercalated 1T'-MoS₂ K₂S-intercalated 2H-MoS₂ were constructed, denoted as 1T'-(K₂S)_{x=0.22}MoS₂ and $2H-(K_2S)_{x=0.17}MoS_2$, respectively, with the chemical percentage of K₂S approximating the experimental observation (x=0.18). These models are shown in Figure 4.8. In these models, K₂S formed a 1T monolayer intercalated between two layers of MoS₂, creating a sandwich-like structure. Upon structural relaxation, the K₂S intercalation layer relaxed to a nearly flat monolayer in 1T'-(K₂S)_{x=0.22}MoS₂, with the interlayer distance of MoS₂ reaching 8.10 Å, closely matching the experimental value of 9.06 Å. In contrast, the 2H-(K₂S)_{x=0.17}MoS₂ model exhibited an interlayer distance of 11.4 Å, deviating from the experimental observation.



Table 4.1: Average bond length of Mo-Mo and Mo-S of MoS₂ before and after K₂S intercalation acquired by theoretical calculation.

average bond length (Å)	2H MoS ₂	K ₂ S-intercalated 2H MoS ₂		
Мо-Мо	3.16	3.17	2.79	2.81
Mo-S	2.40	2.41	2.43	2.44

The average bond lengths of Mo-Mo and Mo-S in MoS₂ after K₂S intercalation were also determined, as shown in Table 4.1. The results indicate that K₂S intercalation has minimal impact on the in-plane structure of both 2H and 1T' MoS₂, as the average bond lengths of Mo-Mo and Mo-S remain nearly unchanged. This is consistent with experimental findings, where TEM and XRD data suggest that the in-plane structure of 1T' MoS₂ is preserved after intercalation.

The formation energy of K₂S-intercalated MoS₂ systems were then calculated using the expression:

$$E_{f(x)} = E_{X-(K_2S)_xMoS_2} - E_{X-MoS_2} - xE_{K_2S}$$

where $E_{X-(K_2S)_xMoS_2}$ represents the total energy of the K₂S-intercalated MoS₂ system in phase X (1T' or 2H), E_{X-MoS_2} is the total energy of MoS₂ in the same phase, and E_{K_2S} is the total energy of the K₂S cubic bulk. The formation energies of K₂S-intercalated 1T'- and 2H-MoS₂ models were -0.077 eV/atom and 0.076 eV/atom, respectively, indicating that the K₂S-intercalated 1T'-MoS₂ is more energetically stable.



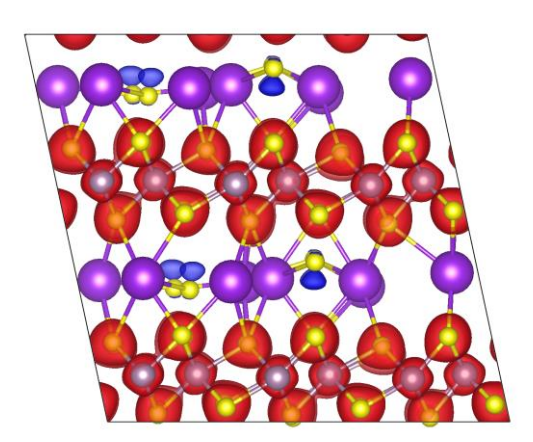


Figure 4.9: Isosurface plots of charge density differences for the 1T'- $(\text{K}_2\text{S})_{x=0.22}\text{MoS}_2$ models. The isosurface densities for the charge accumulation region (red color) and depletion region (bule color) are 0.15 e/Bohr³ and 0.01 e/Bohr³, respectively.

This increased stability of 1T' phase over the 2H phase is attributed primarily to the interlayer confinement effect of K₂S intercalation and enhanced N-doping effect in the MoS₂. To investigate the interlayer confinement effect, we have analyzed the average bond lengths of K-S within K₂S layer (intralayer) and between K₂S and MoS₂ layers (interlayer). For 1T' phase, the average intralayer K-S bond length was about 3.42 Å, and interlayer K-S bond length was about 3.26 Å. For 2H phase, the intralayer K-S bond length averaged to about 3.08 Å, while the interlayer K-S bond length was about 3.34 Å. The shorter interlayer K-S bond length in the 1T' phase implies stronger interlayer interactions, enhancing the confinement effect of K₂S intercalation within the 1T'-MoS₂ structure.



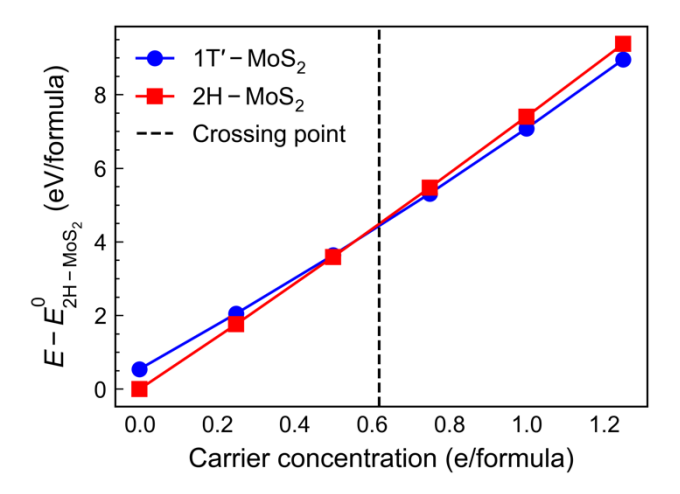


Figure 4.10: Energy difference between the pristine 1T'- and 2H-MoS₂ models as a function of increasing electron doping concentration.

To investigate charge transfer in the K₂S-intercalated MoS₂, we have conducted the bader charge analysis and summarized the results in Table 4.2 and Table 4.3. The analysis revealed that charge transfer occurs primarily from the S atoms of K₂S layer to the S atoms in the MoS₂ layer, with a significantly larger magnitude for the 1T' phase (-1.04 electrons per S atom) compared to the 2H phase (-0.46 electrons per S atom). Charge density difference plots further confirmed enhanced N-doping in the 1T'-MoS₂, as show in Figure 4.9. To investigate the influence of charge transfer on structural stability, we have performed electron doping calculations on pristine 1T'-and 2H-MoS₂, as shown in Figure 4.10. The results indicated that increasing electron doping concentration favored the stability of the 1T' phase over the 2H phase, affirming that enhanced N-doping effect in the K₂S-intercalated 1T'- MoS₂ contributes significantly to its stability.



Table 4.2: Bader charge analysis of the K₂S-intercalated 1T' MoS₂ model.

bader charge (e)	Mo	S	K	S
K ₂ S-intercalated 1T' MoS ₂	4.327	6.967	8.179	6.467
K ₂ S (cubic-bulk)			8.246	7.508
MoS ₂ (1T'-bulk)	4.324	6.838		
delta_e	0.003	0.129	-0.067	-1.041

Table 4.3: Bader charge analysis of the K₂S-intercalated 2H MoS₂ model.

bader charge (e)	Mo	S	K	S
K ₂ S-intercalated 2H MoS ₂	4.255	6.919	8.195	7.052
K ₂ S (cubic-bulk)			8.246	7.508
MoS ₂ (2H-bulk)	4.308	6.846		
delta_e	-0.053	0.073	-0.051	-0.456

According to the above results, a conclusion can be drawn that the chemical environment of intercalated K₂S is different from the potassium sulfide. There are bonds between intercalated K₂S and 1T' MoS₂. According to the theoretical calculation, the Bader charge analysis reveals the charge transfer from K₂S to MoS₂ (N-doping effect), and the K atoms in K₂S bond



with S atoms in MoS₂. The N-doping effect and interlayer confinement effect together stabilize the whole system, including intercalated K₂S and MoS₂.

The band diagram of K₂S-intercalated 1T'MoS₂ is shown in Figure 4.11, which indicates it's still metallic.

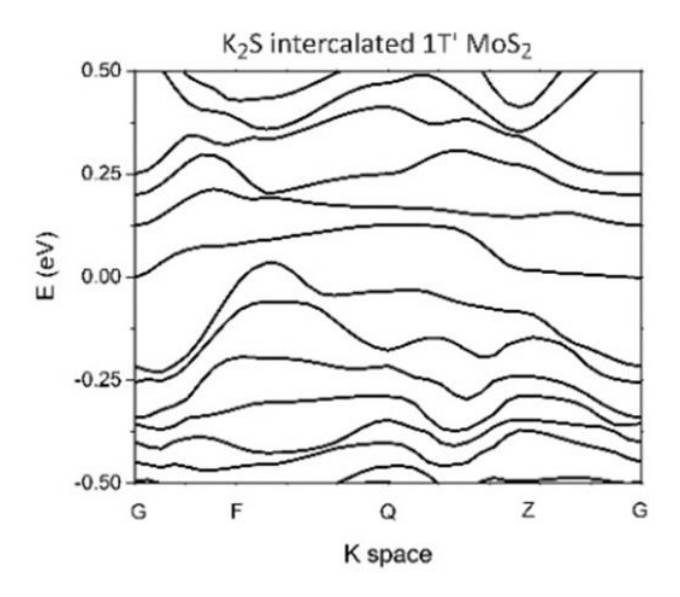


Figure 4.11: The band diagrams of K₂S-intercalated 1T' MoS₂

4.4 Summary

In summary, a scalable method involving self-intercalation has been developed to synthesize phase-pure K₂S-intercalated 1T' MoS₂. This method is well-suited for mass production, as it employs inexpensive reactants and equipment, and requires only a single step and a few hours for completion. Additionally, the process is versatile and can be applied to various TMDs. In addition to K₂S-intercalated 1T' MoS₂, Li₂S-intercalated and Na₂S-intercalated 1T' MoS₂ have also been successfully synthesized using this method. Furthermore, K₂Se-intercalated 1T' MoSe₂, Na₂Se-intercalated 1T' MoSe₂, and K₂Te-intercalated 1T' MoTe₂ have been successfully prepared, demonstrating the method's adaptability. This work opens up a new approach for synthesizing phase-pure 1T' TMDs



and stabilizing them via intercalation without altering their in-plane structure. It paves the way for more accessible exploration of the novel properties of metastable-phase TMDs and the development of their promising applications across various fields.



Chapter 5

Durable K₂S-intercalated 1T' MoS₂ Electrocatalyst for Efficient Hydrogen Evolution Reaction



5.1 Introduction

Hydrogen is one of the most important clean energy in the future, as it could potentially replace fossil fuel that causes large-scale carbon emission and environment pollution. The hydrogen evolution reaction (HER) is a significant way to produce hydrogen, for which it is necessary to develop a low-cost, earth-abundant, and efficient HER electrocatalyst. Current commonly used Pt-based catalysts require expensive and rare platinum, greatly hindering its massive applications.¹⁷⁹ In recent years, the TMDs materials have drawn tremendous attention in the area of HER catalysis. The edge sites of 2H MoS₂ flakes are found active in HER catalysis.²⁹ However, the basal plane of 2H MoS₂ has been found inert for HER catalysis. So, there is quite much effort focusing on exposing edge sites as much as possible ^{96,180}, or inducing active sites by doping ¹⁸¹. However, 2H MoS₂ is semiconducting, blocking the electron transport, thus leading to low HER catalysis efficiency.

Fortunately, the 1T' MoS₂ possess much better HER catalysis performance because it is metallic and both in-plane and edge sites are active in catalysis.²⁹ Therefore, there is no need to consider the issues about edge site exposing or introduction of additional active sites by doping. It is worthy to note that the synthesis of 1T' MoS₂ with phase purity and stabilization remains a huge challenge.⁷² The structure of 1T' MoS₂ is totally different from 2H phase, which is the origin of its excellent HER catalysis performance and also the origin of its low stability. The 1T' MoS₂ is metastable and has higher system energy than 2H phase, which transforms to 2H phase gradually at room temperature or instantly over 100 °C.¹¹⁵ This feature makes 1T' MoS₂ difficult to be synthesized and unreliable in applications. And this is the reason why as-synthesized 1T' MoS₂ had low phase purity and bad HER long-term stability in previous reports. Nevertheless, the 1T' MoS₂ has been considered as an excellent earth-abundant electrocatalyst for hydrogen evolution reaction (HER), as it's metallic, which helps transport of electrons, and has high density of catalysis active



sites.^{97,182,183} And theory calculation¹²⁴ proves pure 1T' MoS₂ possesses advanced electrochemical HER performance.

Here, 1T' MoS₂ with intercalant of K₂S has been grown on carbon cloth by self-intercalation method for HER catalysis. The intercalation of K₂S adjusts the system energy and stabilizes the 1T' MoS₂. Therefore, the critical drawback of intrinsic 1T' MoS₂, low stability, has been overcome. The as-synthesized K₂S-intercalated 1T' MoS₂ represents excellent HER long-term stability, making it feasible in HER electrocatalyst application. Moreover, the 100% phase purity enhances HER performance compared with mixed-phase electrocatalysts. As a result, the sample shows excellent HER electrocatalyst performance with a low onset potential of -73 mV at the current density of 10 mA/cm² and low Tafel slope of 39.3 mV/dec. And the HER long-term stability (30000 cycles and 1000 hours with constant current density of 50 mA/cm²) is much better than counterparts.

5.2 K₂S-intercalated 1T' MoS₂ HER Catalysts Preparation and Setup

To perform the HER test, the K₂S-intercalated 1T' MoS₂ was directly grown on carbon cloth. First, the carbon cloth was placed on a 130 °C hotplate, and a few drops of ethanol were added to soak it. Next, 10 drops of a saturated K₂MoO₄ solution were applied to the carbon cloth, one drop at a time, over the course of one minute. The carbon cloth was then left on the hotplate for 20 minutes to dry, allowing the solid K₂MoO₄ to uniformly adhere to the fabric. The subsequent process followed the same procedure as the synthesis of K₂S-intercalated 1T' MoS₂ demonstrated in Chapter 3, but with the K₂MoO₄/carbon cloth replacing the K₂MoO₄ powder.

A three-zone furnace with a one-meter-long quartz tube was used for the synthesis of

K₂S-intercalated 1T' MoS₂/carbon cloth for HER catalysis, as shown in Figure 5.1. To ensure precise synthesis, it was crucial to use a completely clean quartz tube, free of any residual substances, particularly sulfur, which could affect the reaction. For each synthesis, a new, clean quartz tube was employed. Sulfur powder (10 g) was placed in an alumina boat at the upstream end of the tube (heating zone 1). The sulfur served as an excess reagent and covered the bottom of the alumina boat (bottom area: 910 mm²) throughout the synthesis, providing a consistent supply of sulfur via evaporation.

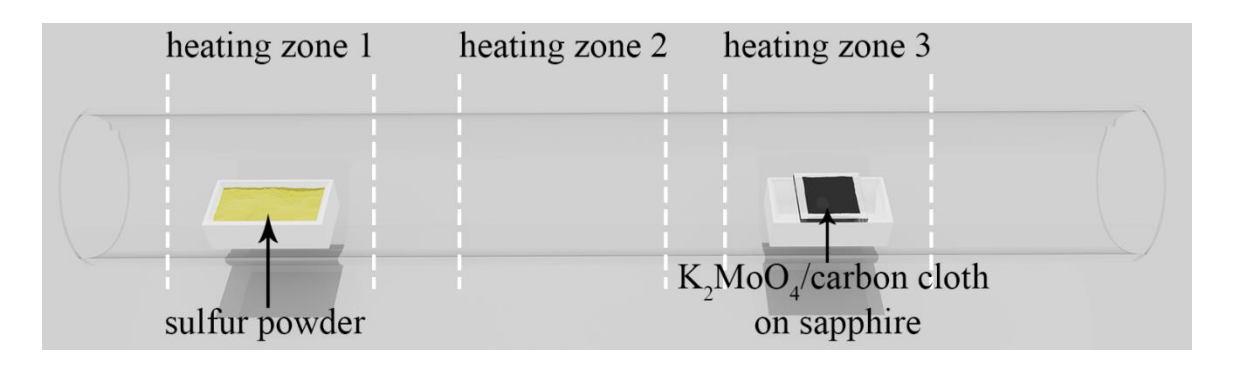


Figure 5.1: Schematic of K₂S-intercalated 1T' MoS₂/carbon cloth synthesis setup.

The K₂MoO₄/carbon cloth was placed in the downstream end of the tube (heating zone 3), atop another alumina boat, while the middle zone (zone 2) was left empty. Before beginning the synthesis, the quartz tube was evacuated to remove air, then purged with argon to restore atmospheric pressure. During the process, argon gas was introduced at a flow rate of 35 sccm, with hydrogen added at 15 sccm, and the left process was conducted at atmospheric pressure. Zones 2 and 3 were heated to 750 °C at a rate of 15 °C/min, while zone 1 remained at room temperature. Once zones 2 and 3 reached 750 °C, zone 1 was gradually heated to 135 °C at 30 °C/min to ensure controlled sulfur vaporization. This step prevented premature sulfur release and avoided unwanted reactions at temperatures below the growth threshold.

If a quartz tube is reused, it must be thoroughly cleaned to prevent any residual sulfur from vaporizing during heating, which could lead to undesirable low-temperature reactions. The



temperatures in zones 2 and 3 were maintained at 750 °C for 4 hours, while zone 1 remained at 135 °C. After the synthesis, the furnace was allowed to cool naturally to room temperature. Once cooled, the sample was collected, yielding the K₂S-intercalated 1T' MoS₂/carbon cloth without any need for post-treatment. The final loading mass was 22.7 mg/cm².

For the HER measurements, an electrochemical setup using an H-type cell was employed, carefully designed to prevent contamination from the reference and counter electrodes, as shown in Figure 5.2. The electrochemical configuration consisted of a 0.5 M H₂SO₄ electrolyte, with the K₂S-intercalated 1T' MoS₂/carbon cloth as the working electrode, a saturated Ag/AgCl reference electrode, and a graphite counter electrode. The Ag/AgCl reference electrode was converted to the reversible hydrogen electrode (RHE) scale by calibration in a H₂-saturated electrolyte against a Pt electrode. Graphite was selected for the counter electrode instead of platinum to prevent potential platinum deposition on the working electrode. The graphite counter electrode was placed in one chamber of the H-type cell, which was separated from the other chamber by a Nafion membrane. The working electrode and reference electrode were positioned in the opposite chamber. To prevent contamination, a double bridge setup with Vycor glass junctions was used to position the reference electrode. For comparison, the electrochemical HER performance of commercially available Pt/C was also tested. In this case, Pt/C was drop-dried onto a glassy carbon electrode and covered with a Nafion film, following the standard procedure.



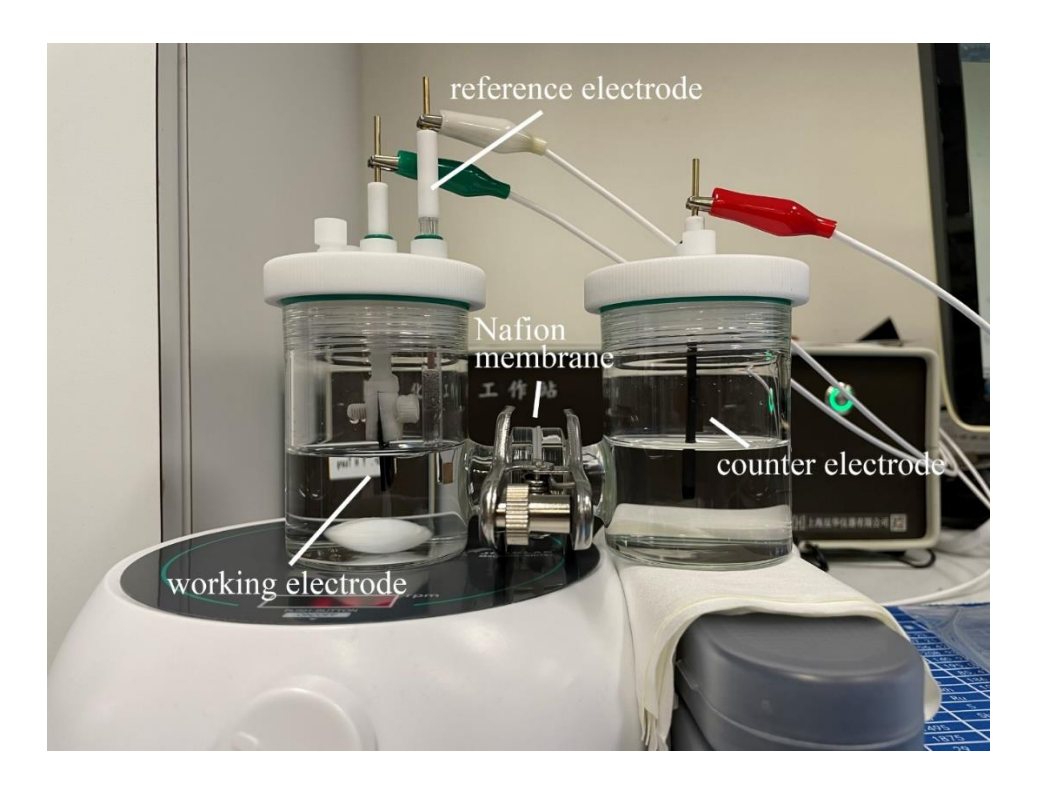


Figure 5.2: Photo of the electrochemical setup.

Figure 5.3a shows a photo of the blank carbon cloth and the carbon cloth with K₂S-intercalated 1T' MoS₂ grown on it, referred to as K₂S-intercalated 1T' MoS₂/CC for simplicity in this article. The size of K₂S-intercalated 1T' MoS₂/CC is scalable, with the only limitation being the diameter of furnace tube. The carbon cloth can be easily cut into any shape, and K₂S-intercalated 1T' MoS₂/CC with any wanted shape can be obtained. Figure 5.3a shows two square pieces of samples with size of 1.5 cm and 2 cm. The scalability and versatility of this method make it feasible for various applications. As depicted in the Scanning electron microscope (SEM) images (Figure 5.3b), the intercalated 1T' MoS₂ flakes are standing on the carbon cloth fibers, which are fully covered. The zoom-in SEM image, shown in Figure 5.3c, represents the 1T' MoS₂ flakes with random orientations and the size of over 50 μm.



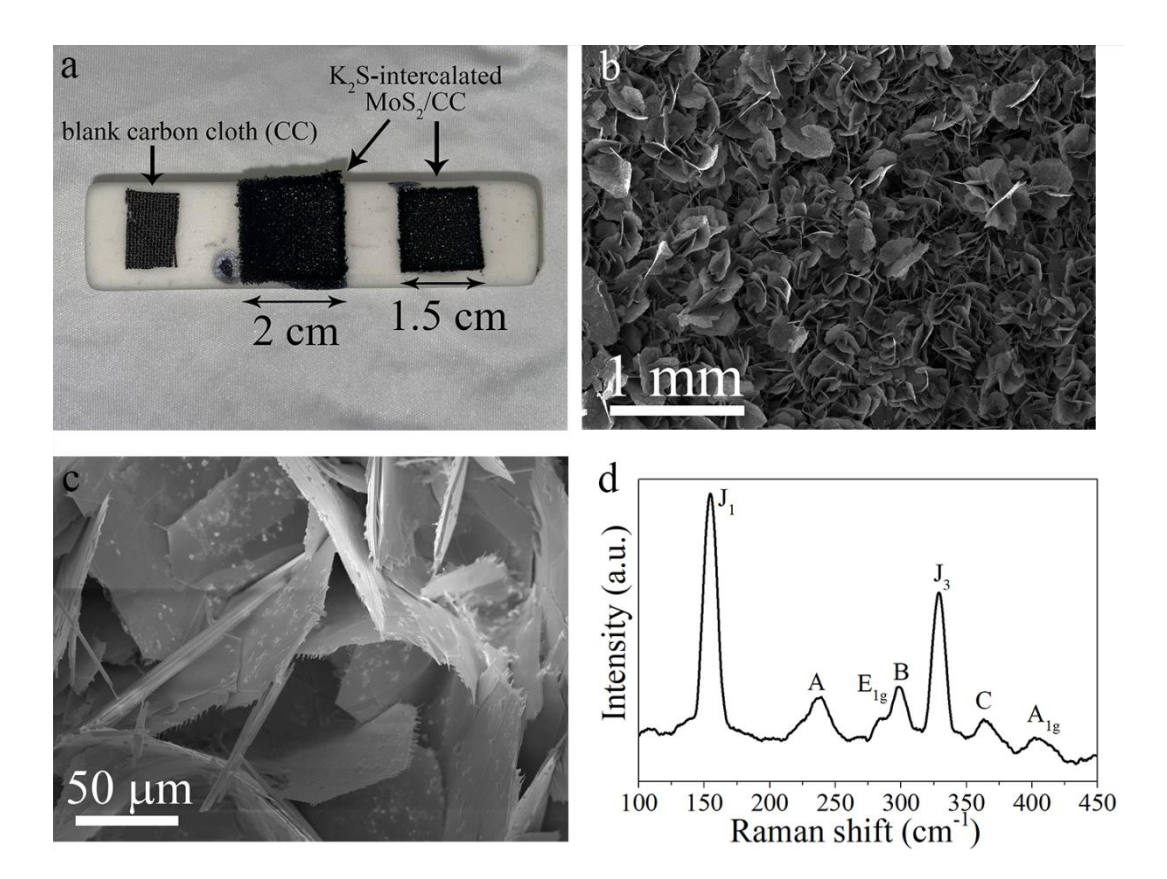


Figure 5.3: (a) Photo of blank carbon cloth and carbon cloth with K₂S-intercalated 1T' MoS₂ grown on. (b) SEM image of K₂S-intercalated 1T' MoS₂ grown on carbon cloth. (c) Zoom-in SEM image of K₂S-intercalated 1T' MoS₂ flakes grown on carbon cloth. (d) Raman spectrum of K₂S-intercalated 1T' MoS₂ grown on carbon cloth.

The Raman spectrum of sample is shown in Figure 5.3d, representing the characteristic 1T' MoS₂ peaks without the E_{2g} peak characteristic of the 2H phase. This confirms that the sample prepared by self-intercalation method is 1T'-phase pure. The distinct J₁ and J₂ peak characteristic of 1T' MoS₂ in Raman spectrum indicate the high crystal quality, without the presence of defect-related J₂ peak. Peak A, B, and C are related to intercalation.

5.3 HER Performance

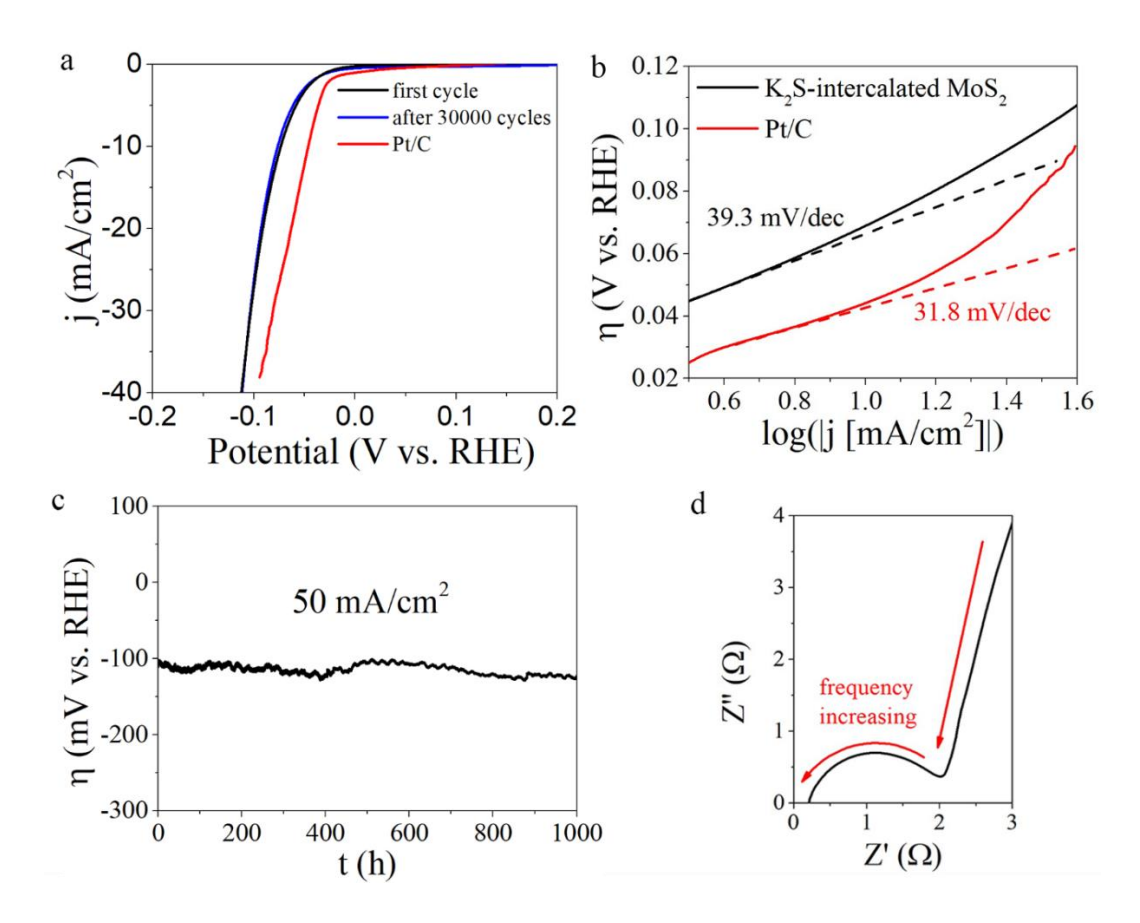


Figure 5.4: (a) The polarization curves (iR corrected) of K₂S-intercalated 1T' MoS₂ HER electrocatalyst before and after 30000 cycles, and commercial Pt/C HER electrocatalyst. (b) The corresponding Tafel slopes of K₂S-intercalated 1T' MoS₂ and commercial Pt/C HER electrocatalysts derived from a. (c) Overpotential vs. time curve of K₂S-intercalated 1T' MoS₂ HER electrocatalyst with constant current density of 50 mA/cm². (d) Nyquist plot of K₂S-intercalated 1T' MoS₂ electrocatalyst.

Unlike many previously reported 1T' TMD-based electrocatalysts, which are covered by Nafion film, the K₂S-intercalated 1T' MoS₂/CC can be directly immersed in 0.5 M H₂SO₄ electrolyte during the HER test, demonstrating stability in strong acid. The electrochemical HER performance of commercially available Pt/C was also tested for comparison. The polarization curves (iR-corrected) for both K₂S-intercalated 1T' MoS₂ and Pt/C are shown

in Figure 5.4a. The K₂S-intercalated 1T' MoS₂ exhibits a low onset potential of -73 mV at a current density of 10 mA/cm², with a corresponding Tafel slope of 39.3 mV/dec, as shown in Figure 5.4b. Importantly, the K₂S-intercalated 1T' MoS₂ demonstrates excellent long-term stability. Even after 30000 cyclic voltammetry (CV) cycles (overpotential range: -0.25~0.2 V vs. RHE), the polarization curve remains nearly unchanged (Figure 5.4a). The SEM image of the sample after 30000 cycles (Figure 5.5) shows that the K₂S-intercalated 1T' MoS₂ flakes still stand on the carbon cloth with no significant morphological change. Raman spectroscopy (Figure 5.6) further confirms that the 1T' phase is maintained after the long-term stability test.

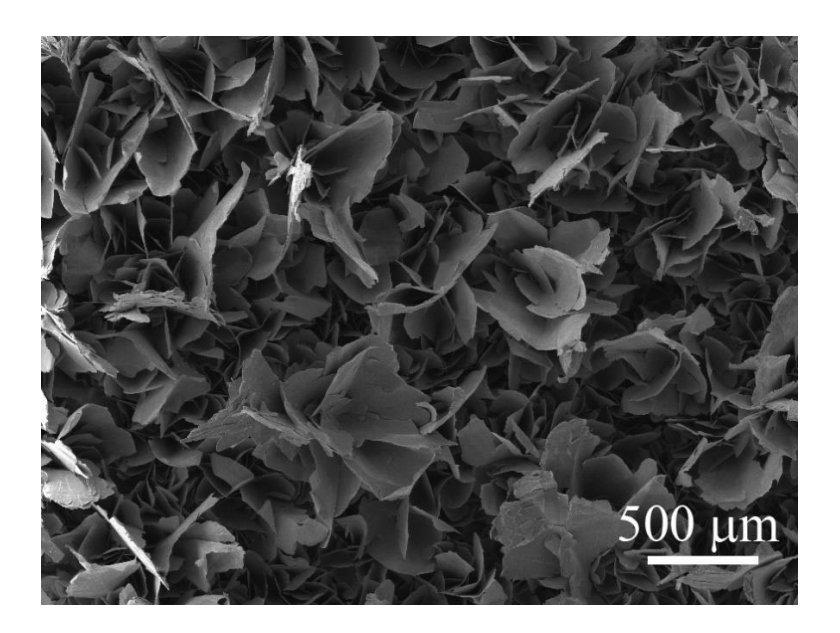


Figure 5.5: SEM image of K₂S-intercalated 1T' MoS₂/CC after 30000 cycles, used as HER electrocatalyst.

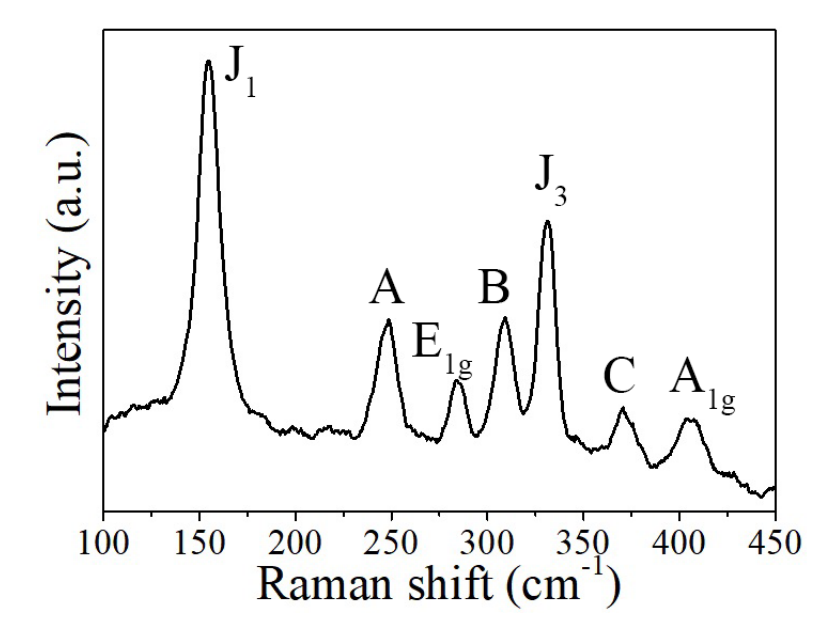


Figure 5.6: Raman spectrum of K₂S-intercalated 1T' MoS₂/CC after 30000 cycles, used as HER electrocatalyst.

To thoroughly evaluate the long-term stability, chronopotentiometric analysis was also conducted. In the same electrochemical configuration, the K₂S-intercalated 1T' MoS₂ was used as the HER electrocatalyst for 1000 hours at a constant current density of 50 mA/cm². The overpotential was continuously recorded, and the overpotential vs. time curve (Figure 5.4c) shows minimal fluctuation during this 1000-hour period. The observed zigzag fluctuations are due to the accumulation and release of hydrogen bubbles on the K₂S-intercalated 1T' MoS₂ surface, which momentarily block contact with the electrolyte. No signs of degradation were observed during the 1,000-hour stability test. Figure 5.4d presents the Nyquist plot of the K₂S-intercalated 1T' MoS₂ electrocatalyst, with a frequency range from 1 Hz to 10⁵ Hz. The curve shows a semicircular shape in the high-frequency region, corresponding to the kinetic control, while the right linear region at low frequency is dominated by mass transfer control. The charge transfer resistance (R_{ct}) is as low as 1.8 Ω, which is attributed to the highly HER-active metallic 1T' MoS₂.

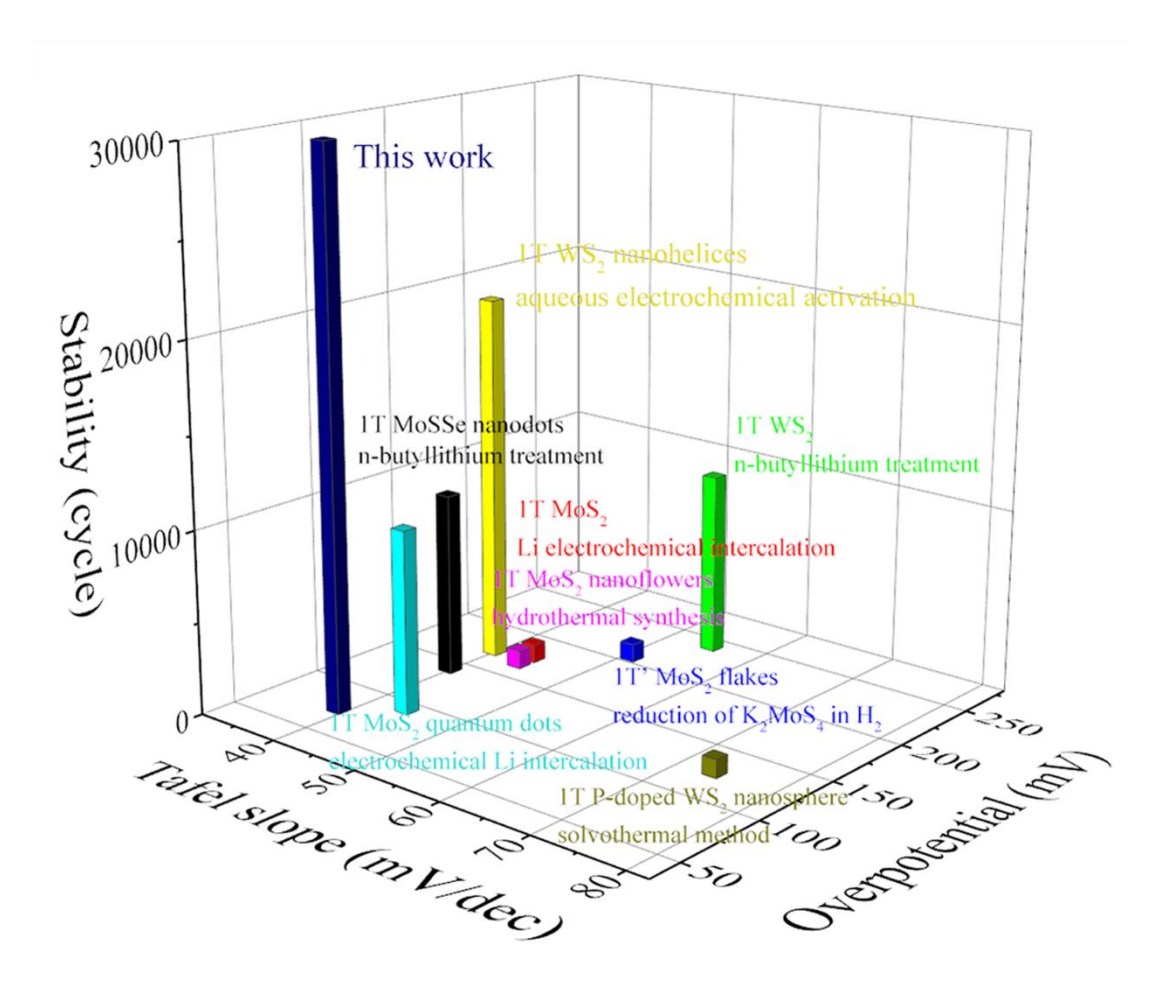


Figure 5.7: Comparison with best TMDs-based HER electrocatalysts in three perspectives (Tafel slope, overpotential, and stability). The details of all compared cases shown, including phase purity, electrode type, literature source, are listed in Table 5.1.

These results confirm that K₂S-intercalated 1T' MoS₂ exhibits excellent electrochemical HER performance (onset potential of -73 mV at 10 mA/cm² and a Tafel slope of 39.3 mV/dec), comparable to the best TMD-based and non-precious HER electrocatalysts. Notably, its exceptional stability—both over 1,000 hours at 50 mA/cm² and 30000 CV cycles—sets it apart from other electrocatalysts. A comparison of reported electrocatalysts for HER is provided in Table 5.1 and 5.2. Figure 5.7 compares the K₂S-intercalated 1T' MoS₂ with the best TMD-based HER electrocatalysts, evaluating three critical factors: Tafel slope, overpotential, and stability. This figure shows the name of material and synthesis method of each case. The previously reported TMD-based HER electrocatalysts usually

could not achieve both high HER efficiency and good stability at the same time. However, the comparison highlights that the K₂S-intercalated 1T' MoS₂ synthesized in this study exhibits exceptional HER performance, including stability and HER catalyst efficiency, which is the result of introduction of advanced self-intercalation synthesis method.

The excellent HER performance of the K₂S-intercalated 1T' MoS₂ is primarily attributed to its high phase purity. The two-dimensional 1T' MoS₂ flakes have catalytic active sites both at the edges and on the plane, while two-dimensional 2H MoS₂ flakes only have active sites at the edges.¹²⁴ The metallic 1T' phase also enhances electron transport, whereas the semiconducting 2H MoS₂ impedes it. As a result, the phase-pure 1T' MoS₂ synthesized in this work demonstrates a low onset potential and a low Tafel slope. Furthermore, the K₂S intercalation provides stability, preventing the phase transition from 1T' to 2H, a major limitation of pure 1T' MoS₂, which tends to degrade during HER. This intervention effectively overcomes the inherent low stability of the 1T' phase, leading to superb long-term stability in HER performance.

Table 5.1: The best TMDs-based HER electrocatalysts via phase engineering.

materials	preparation method	phase purity (%)	electrode	Tafel slope (mV/dec)	overpotential η (mV) at 10 mA/cm ²	stability	Ref.
1T MoS ₂ nanodots	n-butyllithium treatment	70	glassy	53	173	no data	96
1T MoSSe nanodots	n-butyllithium treatment	67	glassy	40	140	10000 cycles	



1T MoS ₂	Li electrochemical intercalation	53.7	mirror polished glassy carbon	44	175	1000 cycles; 20 mA/cm² for 5 h	186
1T WS ₂	n-butyllithium treatment	76	glass carbon	55	Ca. 240	10000 cycles; η = -0.3 V for 120 h	182
1T' MoS ₂	Lithium intercalation using lithium borohydrate	80	glassy carbon	40	Ca. 200	no data	187
1T/2H MoS ₂ flake	n-butyllithium treatment	70	Au pad	50	Ca. 210	no data	188
1T' WSe ₂	colloidal phase synthesis	not specified	carbon paper	150	300	no data	110
1T' MoS ₂ flakes	reduction of K ₂ MoS ₄ in H ₂	90	highly oriented pyrolytic graphite	51	205	1000 cycles	59



1T MoS ₂ quantum dots	electrochemical Li intercalation	92–97	carbon fiber paper	44	92	10000 cycles; 200 mA/cm ² for 80 h	189
2M WSe ₂ nanosheets	colloidal reaction	not specified	glassy carbon	71	104	10 mA/cm ² for 120 h	111
$1T \text{ MoS}_2$ with single-layer hollow structure	Bi ions absorption	not specified	glassy carbon	40	137	30 mA/cm ² for 36 h	190
1T MoSe ₂ — VSe ₂ —NbSe ₂ ternary alloy nanosheets	hot-injection colloidal reaction	60	glassy carbon	55	80	20 mA/cm ² for 120 h	75
1T MoS ₂	hydrothermal synthesis	80.5	carbon paper	44	165	1000 cycles	112
1T WS ₂ nanohelices	aqueous electrochemical activation	70	glassy carbon	40	170	20000 cycles	191
1T P-doped	solvothermal	82.88	carbon	73.73	125	190 mV	113

WS_2	method		fiber paper			for 10 h;	
nanosphere	combined with					1000	
	chemical vapor					cycles	
	deposition						
	K ₂ MoO ₄ , S,					30000	
	and H ₂ reaction					cycles;	
K ₂ S-intercalated	with restricted	100	carbon	39.3	73	50	This
1T' MoS ₂	reaction	100	cloth	37.3	73	mA/cm ²	work
	temperature at					for 1000	
	750 °C					hours	

 Table 5.2: Representative non-precious HER electrocatalysts.

materials	electrode	Tafel slope (mV/dec)	overpotential η (mV) at 10 mA/cm ²	stability	Ref.
CoP nanowire arrays	carbon cloth	51	67	5000 cycles	192
FeP nanowire array	Ti plate	38	57	90 mA/cm ² for 15 h	193
Fe _{0.5} Co _{0.5} P nanowire	carbon cloth	30	37	100 mA/cm ² for 100 h	194
se-MoS ₂ sheet arrays	carbon paper	56	104	10 mA/cm ² for 24 h	180
perpendicularly oriented	graphite	61	159	150 mV for 100 min	195

MoSe ₂ /graphene					
nanosheets					
CoS ₂ micro- and nanostructures	graphite	51.6	145	10 mA/cm ² for 40 h	196
molybdenum phosphosulfide film	Ti foil	50	64	1000 cycles	197
Ni _{0.9} Fe _{0.1} PS ₃ nanosheets	glassy carbon	73	72	no data	198
cobalt encapsulated by N, B codoped ultrathin carbon cages	glassy carbon	63.7	96	200 mV for 10 h	199
NiFe layered double hydroxide nanosheets	nickel foam	62.3	59	1.7 V for 100 h	200
Mott-Schottky heterojunction of semi-conductive MoS_2 nanoparticles/metallic CoS_2 nanotubes	carbon cloth	64.4	99.3	185.8 mV for 50 h	201
carbon-supported MoS _x nanocomposites	glassy carbon	50.03	184	1000 cycles	202
Fe/Mg-N ₄ /nitrogen-dope	glassy carbon	47.9	21	10 mA/cm ² for 80 h	203



d porous carbon					
iron-incorporated molybdenum oxide	Ni foam	71	17	200 mA/cm ² for 200 h	204
cobalt phosphide heterojunctions	carbon paper	106.54	97	50 mA/cm ² for 24 h	205
NiMo/Ni ₂ P heterojunction	Ni foam	29.45	15	5000 cycles; 500 mA/cm ² for 20 h	206
K ₂ S-intercalated 1T' MoS ₂	carbon cloth	39.3	73	30000 cycles; 50 mA/cm ² for 1000 hours	This work

5.4 Summary

In summary, K₂S-intercalated 1T' MoS₂ was directly grown on carbon cloth for HER application. The synthesis process follows the same principle of self-intercalation method demonstrated in Chapter 3. It is an easy low-cost one-step reaction method, suitable for mass-production. The samples possess excellent HER electrocatalyst performance with a low onset potential of -73 mV at the current density of 10 mA/cm² and low Tafel slope of 39.3 mV/dec, comparable with the best non-precious HER electrocatalysts including TMDs, due to the extreme high phase purity. Importantly, the K₂S intercalation brings much better HER stability (30000 cycles and 1000 hours with constant current density of 50 mA/cm²) compared with its counterparts. The excellent HER performance and long-term HER stability confirm that the 1T' MoS₂ prepared by proposed self-intercalation method retains



high HER catalysis activity, originating from intrinsic 1T' MoS₂ in-plane structure, and the intercalation significantly improves the catalysis stability. The proposed self-intercalation method paves the way to stabilize the system while retaining the intrinsic properties, which would be a promising structure engineering methodology.



Chapter 6

Summary and Future Works



Research about transition metal dichalcogenides (TMDs) is a very hot research topic. Compared with the well-studied thermodynamically stable 2H phase, the 1T' phase usually possesses novel properties. And the phase purity has a profound influence on practical application performance and properties such as conductivity. However, many TMDs of 1T' phase are metastable, which makes their applications unfeasible and unreliable. For example, the 1T'-phase MoS₂, one of the most typical TMDs, transforms to the 2H phase gradually over a short time or instantly over 97 °C and loss the favorable properties of 1T' phase.

This thesis demonstrates a mass-production-available method to stabilize the 1T' MoS₂ by K₂S intercalation and study the mechanism. The K₂S-intercalated 1T' MoS₂ has been directly synthesized in one step and shows stability against high temperature (750 °C) and aging exposed to air for more than one year. The characterization and theory calculation results prove that the K₂S locates between the 1T' MoS₂ layers and make metastable 1T' phase become very stable. The K₂S intercalation doesn't change 1T' MoS₂ in-plane structure and properties. It has been found that intercalated K₂S lowers the formation energy of 1T' phase and stabilizes the whole system. Phase purity has been achieved due to novel stabilization and synthesis process, while improving phase purity was a tricky problem in the past. In this thesis, it has been proved this method is versatile for various 1T' TMDs (such as MoSe₂, MoTe₂) and has achieved the intercalation of K₂S, K₂Se, K₂Te, Na₂S, Na₂Se, and Li₂S, as well as stabilization. This method eliminates the most significant disadvantage of metastable 1T' TMDs and enables fundamental research of pure phase 2D materials and practical applications. The fabricated K₂S-intercalated 1T' MoS₂ nanoflakes has been used as hydrogen evolution reaction (HER) electrocatalyst, representing overwhelming HER long-term stability compared with other TMDs electrocatalysts. This study will also benefit other research fields including superconductivity, devices contact, surface-enhanced Raman scattering, energy storage, supercapacitor, synaptic transistors etc.



6.1 Summary

6.1.1 Self-intercalation Method

A self-intercalation method for synthesizing intercalated 1T' TMDs has been demonstrated. By utilizing the structure similarity between intercalated 1T' phase structure and alkali metal molybdate, the direct synthesis of alkali-metal-chalcogenide-intercalated 1T' TMDs has been successfully achieved with controlled heating process. Using this approach, K₂S-intercalated 1T' MoS₂ was synthesized with nearly 100% phase purity and high crystal quality. Characterization results confirm that the material maintains the same in-plane structure as intrinsic 1T' MoS₂, with K₂S acting as an intercalant within the interlayer gap. This unique structure not only preserves the original properties of 1T' MoS₂ but also enhances the system's stability through intercalation. Importantly, the method utilizes inexpensive reagents, a simple tube furnace, and requires only a few hours of processing time, with no need for post-treatment. These features make it suitable for large-scale production, which is crucial for industrial and commercial applications. Moreover, the method is highly adaptable and can be applied to various TMDs. In addition to K₂S-intercalated 1T' MoS₂, Li₂S- and Na₂S-intercalated 1T' MoS₂ have also been synthesized, along with K2Se-intercalated 1T' MoSe2, Na2Se-intercalated 1T' MoSe2, and K₂Te-intercalated 1T' MoTe₂, demonstrating the versatility of the technique.

6.1.2 Stabilization by Self-intercalation

The TMDs intercalated by alkali metal chalcogenides has been synthesized via proposed self-intercalation method. The stability was evaluated, showing thermal stability over 750 °C and inert in air, water, ethanol, and even strong acid. It retains 1T' phase structure



after one-year aging test in air. The prepared intercalated 1T' TMDs represent excellent stability compared with the inherent 1T' TMDs, due to the stabilization by intercalation. The stabilization mechanism through alkali metal chalcogenides intercalation was demonstrated based on the theoretical calculations. It indicates that the intercalation leads to N-doping and bonding formation which lower the system energy, and thus stabilizing the whole system. Besides, the alkali metal chalcogenides are much less chemically active than alkali metals, which avoids oxidation of samples in air or other non-inert environments.

6.1.3 Durable K₂S-intercalated 1T' MoS₂ Electrocatalyst for Efficient Hydrogen Evolution Reaction

The K₂S-intercalated 1T' MoS₂ nanoflakes were grown on carbon cloth following the proposed self-intercalation method which employed a simple, low-cost, one-step reaction that is well-suited for mass production. The K₂S-intercalated 1T' MoS₂/carbon cloth was used as hydrogen evolution reaction catalyst directly in 0.5 M H₂SO₄ electrolyte, representing stability against strong acid. The resulting samples exhibit excellent hydrogen evolution reaction (HER) electrocatalytic performance, with a low onset potential of -73 mV at a current density of 10 mA/cm² and a low Tafel slope of 39.3 mV/dec, comparable to the best non-precious HER electrocatalysts, including other TMDs, due to their extremely high phase purity. Importantly, K₂S intercalation enhances the HER long-term stability, with the material maintaining performance over 30000 cycles and 1000 hours at a constant current density of 50 mA/cm², outperforming its counterparts. The remarkable HER performance and long-term stability confirm that the 1T' MoS₂ synthesized via the proposed self-intercalation method retains the high HER catalytic activity inherent to the intrinsic 1T' MoS₂ in-plane structure, while the intercalation significantly improves its catalytic stability.



This method not only stabilizes the system but also preserves its intrinsic properties, presenting a promising approach for structure engineering in catalysis.

6.2 Future Works

The successful synthesis of 1T' TMDs by self-intercalation method confirms that the synthesis precursor could be molybdate which can be grown in the form of thin film by sputtering deposition method. This method does not rely on the transition from 2H phase TMDs, which is the main route of current synthesis techniques. So, this proposed method provides a flexible manner to grow 1T' TMDs film on various kinds of surfaces. Therefore, it would be convenient to fabricate devices based on 1T' TMDs, while it highly depended on the exfoliation and transfer of 1T' TMDs in the past. In the future, with the combination of sputtering deposition and chemical vapor deposition method, the electronic devices with complex structures, such as heterojunctions, will be built to achieve advanced functions. By employing the anisotropic transport properties of 1T' phase originating from the low structure symmetry, synaptic devices, available for neural computation, will be constructed with the help of proposed combined deposition method, and tested.

In addition to synaptic devices, a topological field-effect (TFET) transistor based on van der Waals heterostructures of 1T' TMDs and two-dimensional dielectric layers is also possible to fabricate based on the 1T' TMDs thin film deposition technique developed by this thesis. It was found that a structural distortion leads to an intrinsic band inversion between the chalcogenide p-bands and the metal d-bands. Furthermore, spin-orbit coupling opens a gap which can be tuned by applying a vertical electric field or strain. This tunability of the gap enables the manipulation of electronic properties, making it possible to control the material's behavior for various applications. Unlike traditional field-effect transistors that



rely on carrier depletion to control the current, the TFET is predicted to rapidly switch off by an electric field-induced topological phase transition. In this configuration, the transition between topologically distinct phases—mediated by the applied electric field—controls the flow of current, offering faster switching speeds and potentially lower power consumption. The combination of the 1T' TMDs, which exhibits intrinsic metallic or semi-metallic behavior, and the 2D dielectric layers enables precise control over the topological phase, leading to a new class of high-performance, low-power transistors. This approach opens up exciting possibilities for the development of advanced electronic devices.

The electrocatalytically active 1T' TMDs also possesses a promising potential in Li-S battery application. Li-S batteries are based on conversion reactions that address the limitations of insertion-oxide cathodes and graphite anodes found in lithium-ion batteries (LIBs), enabling higher energy densities. 207-211 These batteries consist of sulfur cathodes and lithium-metal anodes. However, sulfur is electrically insulating, necessitating its incorporation onto a conducting host, typically made of porous carbon, to facilitate efficient charge transfer. It is reported that the Li-S batteries utilizing metallic 1T-phase molybdenum disulfide as conducting cathodes for hosting sulfur represented high performance, due to the improving the adsorption of lithium polysulfides, enhancing Li⁺ transport, accelerating electrochemical reaction kinetics, and providing superior electrocatalytic activity for conversion.²¹² polysulfide This inspires us that the metallic alkali-metal-chalcogenide-intercalated 1T' TMDs also have possibility to improve the Li-S batteries by acting as conducting cathodes for hosting sulfur, as the in-plane structure and properties are retained after intercalation. Moreover, the intercalation of alkali metal chalcogenides enables superior stability compared with Li-intercalated 1T' MoS₂, which could greatly improve the battery cycling stability, an essential parameter for batteries.



References

- 1 Yin, X. M. *et al.* Recent developments in 2D transition metal dichalcogenides: phase transition and applications of the (quasi-)metallic phases. *Chem. Soc. Rev.* **50**, 10087-10115 (2021). https://doi.org/10.1039/d1cs00236h
- 2 Alotaibi, F. *et al.* Scanning atmospheric plasma for ultrafast reduction of graphene oxide and fabrication of highly conductive graphene films and patterns. *Carbon* **127**, 113-121 (2018). https://doi.org/10.1016/j.carbon.2017.10.075
- 3 Candini, A. *et al.* Electroburning of few-layer graphene flakes, epitaxial graphene, and turbostratic graphene discs in air and under vacuum. *Beilstein J. Nanotechnol.* **6**, 711-719 (2015). https://doi.org/10.3762/bjnano.6.72
- 4 Chen, W. Q. *et al.* Controlled Nanopore Formation in Graphene/Graphene Oxide Nanosheets: Implication for Water Transport. *ACS Appl. Nano Mater.* **5**, 3811-3823 (2022). https://doi.org/10.1021/acsanm.1c04445
- 5 Farivar, F., Yap, P. L., Karunagaran, R. U. & Losic, D. Thermogravimetric Analysis (TGA) of Graphene Materials: Effect of Particle Size of Graphene, Graphene Oxide and Graphite on Thermal Parameters. *C-J. Carbon Res.* 7, 12 (2021). https://doi.org/10.3390/c7020041
- 6 Galvagno, E. *et al.* Present Status and Perspectives of Graphene and Graphene-related Materials in Cultural Heritage. *Adv. Funct. Mater.* **34**, 31 (2024). https://doi.org/10.1002/adfm.202313043
- 7 Huang, G. J. *et al.* Surface Functional Modification of Graphene and Graphene Oxide. *Acta Chim. Sin.* **74**, 789-799 (2016). https://doi.org/10.6023/a16070360
- 8 Luo, J. J. *et al.* Graphene Oxide "Surfactant"-Directed Tunable Concentration of Graphene Dispersion. *Small* **16**, 10 (2020). https://doi.org/10.1002/smll.202003426
- 9 Papageorgiou, D. G., Kinloch, I. A. & Young, R. J. Mechanical properties of graphene



- and graphene-based nanocomposites. *Prog. Mater. Sci.* **90**, 75-127 (2017). https://doi.org/10.1016/j.pmatsci.2017.07.004
- 10 Aftab, S. & Hegazy, H. H. Emerging Trends in 2D TMDs Photodetectors and Piezo-Phototronic Devices. *Small* **19**, 24 (2023). https://doi.org/10.1002/sml1.202205778
- 11 Aftab, S., Iqbal, M. Z. & Rim, Y. S. Recent Advances in Rolling 2D TMDs Nanosheets into 1D TMDs Nanotubes/Nanoscrolls. *Small* **19**, 22 (2023). https://doi.org/10.1002/smll.202205418
- 12 Chen, Z. X. *et al.* Phase-modulated quantum-sized TMDs for extreme saturable absorption. *Nano Research* **16**, 5803-5808 (2023). https://doi.org/10.1007/s12274-022-5119-3
- 13 Ebert, M. A., Schindler, S. T., Stewart, I. W. & Zhao, Y. Factorization connecting continuum & lattice TMDs. *J. High Energy Phys.*, 53 (2022). https://doi.org/10.1007/jhep04(2022)178
- 14 Hu, H. *et al.* Interface Effects in Metal-2D TMDs Systems: Advancing the Design and Development Electrocatalysts. *Adv. Sci.* **12**, 23 (2025). https://doi.org/10.1002/advs.202500226
- 15 Huang, H. *et al.* The fundamentals, progress, and perspectives of transition-metal dichalcogenides (TMDs) applied in advanced oxidation processes. *Chem. Eng. J.* **484**, 25 (2024). https://doi.org/10.1016/j.cej.2024.149595
- 16 Li, E. L. *et al.* Electronic properties of van der Waals heterostructures based on F-GaN-H stacking and TMDs single layer. *Vacuum* **206**, 10 (2022). https://doi.org/10.1016/j.vacuum.2022.111546
- 17 Liu, M. J. *et al.* Two-Dimensional Transition Metal Dichalcogenides (2D TMDs) Coupled With Zero-Dimensional Nanomaterials (0D NMs) for Advanced Photodetection. *Small Methods* **9**, 25 (2025). https://doi.org/10.1002/smtd.202401240
- 18 Radhakrishnan, J., Ratna, S. & Biswas, K. Metal oxide/2D layered TMDs composites



- for H2 evolution reaction via photocatalytic water splitting A mini review. *Inorg. Chem. Commun.* **145**, 9 (2022). https://doi.org/10.1016/j.inoche.2022.109971
- 19 Zeng, H. L., Dai, J. F., Yao, W., Xiao, D. & Cui, X. D. Valley polarization in MoS₂ monolayers by optical pumping. *Nat. Nanotechnol.* 7, 490-493 (2012). https://doi.org/10.1038/nnano.2012.95
- 20 Xu, X. D., Yao, W., Xiao, D. & Heinz, T. F. Spin and pseudospins in layered transition metal dichalcogenides. *Nat. Phys.* **10**, 343-350 (2014). https://doi.org/10.1038/nphys2942
- 21 Xia, F. N., Wang, H., Xiao, D., Dubey, M. & Ramasubramaniam, A. Two-dimensional material nanophotonics. *Nature Photonics* **8**, 899-907 (2014). https://doi.org/10.1038/nphoton.2014.271
- 22 Aftab, S., Hegazy, H. H. & Kabir, F. Emerging Trends in 2D Flexible Electronics. *Adv. Mater. Technol.* **8**, 16 (2023). https://doi.org/10.1002/admt.202201897
- 23 Kan, S. S. *et al.* Growth of vertical type InSe/TMDs heterostructures for efficient charge transfer and nonlinear optical performance. *Appl. Surf. Sci.* **656**, 12 (2024). https://doi.org/10.1016/j.apsusc.2024.159705
- 24 Katiyar, A. K. *et al.* Strain-Induced Bandgap Narrowing in Crumpled TMDs for NIR Light Detection. *Small* **21**, 12 (2025). https://doi.org/10.1002/smll.202411378
- Liu, Y. X. *et al.* Collaborative control of charge transfer and ultrafast transient behavior through coupling and interfacial engineering in MXene/TMDs heterostructures realize effective photoelectrochemical. *J. Power Sources* **641**, 16 (2025). https://doi.org/10.1016/j.jpowsour.2025.236826
- 26 Shahbaz, I., Tahir, M., Li, L. H. & Song, Y. L. Advancements in 2D transition metal dichalcogenides (TMDs) inks for printed optoelectronics: A comprehensive review. *Mater. Today* 77, 142-184 (2024). https://doi.org/10.1016/j.mattod.2024.06.008
- 27 Zhou, G. G. *et al.* Scalable electronic and optoelectronic devices based on 2D TMDs. *Mater. Futures* **3**, 29 (2024). https://doi.org/10.1088/2752-5724/ad7c6c



- 28 Jaramillo, T. F. *et al.* Identification of active edge sites for electrochemical H₂ evolution from MoS₂ nanocatalysts. *Science* **317**, 100-102 (2007). https://doi.org/10.1126/science.1141483
- 29 Zhang, J. *et al.* Unveiling Active Sites for the Hydrogen Evolution Reaction on Monolayer MoS₂. *Adv. Mater.* **29**, 7 (2017). https://doi.org/10.1002/adma.201701955
- 30 Chen, B. *et al.* In Situ Porousized MoS2 Nano Islands Enhance HER/OER Bifunctional Electrocatalysis. *Small* **19**, 13 (2023). https://doi.org/10.1002/smll.202207177
- 31 Li, Z. D. *et al.* Manipulating Coordination Structures of Mixed-Valence Copper Single Atoms on 1T-MoS2 for Efficient Hydrogen Evolution. *ACS Catal.*, 7687-7695 (2022). https://doi.org/10.1021/acscatal.2c00759
- 32 Loh, J. Y., Yap, F. M. & Ong, W. J. 2D/2D heterojunction interface: Engineering of 1T/2H MoS2 coupled with Ti3C2Tx heterostructured electrocatalysts for pH-universal hydrogen evolution. *J. Mater. Sci. Technol.* **179**, 86-97 (2024). https://doi.org/10.1016/j.jmst.2023.10.002
- 33 Ozgur, D. O. & Akti, F. Fabrication of 3D ordered mesoporous 1T-phase MoS2@C for electrochemical hydrogen evolution. *Int. J. Hydrog. Energy* **143**, 1144-1153 (2025). https://doi.org/10.1016/j.ijhydene.2025.01.072
- 34 Sharma, U., Karazhanov, S., Alonso-Vante, N. & Das, S. Metallic-phase of MoS2 as potential electrocatalyst for hydrogen production via water splitting: A brief review. *Curr. Opin. Electrochem.* **35**, 10 (2022). https://doi.org/10.1016/j.coelec.2022.101067
- 35 Sun, L. *et al.* Sulfur-Doped rGO Aerogel Enables the Anchoring of 1T/2H MoS2 for Durable Oxygen Reduction Reaction Catalyst Support. *ChemSusChem* **16**, 8 (2023). https://doi.org/10.1002/cssc.202201721
- 36 Zhao, L. *et al.* Stabilizing and Activating Active Sites: 1T-MoS2 Supported Pd Single Atoms for Efficient Hydrogen Evolution Reaction. *Small* **20**, 9 (2024). https://doi.org/10.1002/smll.202401537



- 37 Xu, Y. et al. Large-Gap Quantum Spin Hall Insulators in Tin Films. *Phys. Rev. Lett.* **111**, 5 (2013). https://doi.org/10.1103/PhysRevLett.111.136804
- 38 Ghosal, S. & Jana, D. Beyond T-graphene: Two-dimensional tetragonal allotropes and their potential applications. *Appl. Phys. Rev.* **9**, 29 (2022). https://doi.org/10.1063/5.0088275
- 39 Lu, Z. *et al.* Directed electron transport induced surface reconstruction of 2D NiFe-LDH/Stanene heterojunction catalysts for efficient oxygen evolution. *Appl. Catal. B-Environ. Energy* **353**, 9 (2024). https://doi.org/10.1016/j.apcatb.2024.124073
- 40 Lundgren, C., Kakanakova-Georgieva, A. & Gueorguiev, G. K. A perspective on thermal stability and mechanical properties of 2D Indium Bismide from ab initio molecular dynamics. *Nanotechnology* **33**, 10 (2022). https://doi.org/10.1088/1361-6528/ac6baf
- 41 Wang, M. K., Hu, Y., Pu, J. M., Zi, Y. & Huang, W. C. Emerging Xene-Based Single-Atom Catalysts: Theory, Synthesis, and Catalytic Applications. *Adv. Mater.* **36**, 36 (2024). https://doi.org/10.1002/adma.202303492
- 42 Zhao, C. X. et al. Coexistence of Robust Edge States and Superconductivity in Few-Layer Stanene. Phys. Rev. Lett. 128, 7 (2022). https://doi.org/10.1103/PhysRevLett.128.206802
- 43 Gruznev, D. V. *et al.* Two-Dimensional In-Sb Compound on Silicon Hall Insulator. *Nano Lett.* **18**, 4338-4345 (2018). https://doi.org/10.1021/acs.nanolett.8b01341
- 44 Shirodkar, S. N. & Waghmare, U. V. Emergence of Ferroelectricity at a Metal-Semiconductor Transition in a 1T Monolayer of MoS₂. *Phys. Rev. Lett.* **112**, 5 (2014). https://doi.org/10.1103/PhysRevLett.112.157601
- 45 Acerce, M., Voiry, D. & Chhowalla, M. Metallic 1T phase MoS₂ nanosheets as supercapacitor electrode materials. *Nat. Nanotechnol.* **10**, 313-318 (2015). https://doi.org/10.1038/nnano.2015.40
- 46 Hirunpinyopas, W. et al. Insights into binding mechanisms of size-selected graphene



binders for flexible and conductive porous carbon electrodes. *Electrochim. Acta* **403**, 13 (2022). https://doi.org/10.1016/j.electacta.2021.139696

- 47 Lin, J. Y., Yuan, Y., Wang, M., Yang, X. L. & Yang, G. M. Theoretical Studies on the Quantum Capacitance of Two-Dimensional Electrode Materials for Supercapacitors. *Nanomaterials* **13**, 24 (2023). https://doi.org/10.3390/nano13131932
- 48 Philip, A. & Kumar, A. R. Recent advancements and developments employing 2D-materials in enhancing the performance of electrochemical supercapacitors: A review. *Renew. Sust. Energ. Rev.* **182**, 21 (2023). https://doi.org/10.1016/j.rser.2023.113423
- 49 Rangnekar, S. V. *et al.* Electroluminescence from Megasonically Solution-Processed MoS2 Nanosheet Films. *ACS Nano* **17**, 17516-17526 (2023). https://doi.org/10.1021/acsnano.3c06034
- 50 Sheikh, Z. A. *et al.* Transition metal chalcogenides, MXene, and their hybrids: An emerging electrochemical capacitor electrodes. *J. Energy Storage* **71**, 18 (2023). https://doi.org/10.1016/j.est.2023.107997
- Nasir, M. Z. M., Mayorga-Martinez, C. C., Sofer, Z. & Pumera, M. Two-Dimensional 1T-Phase Transition Metal Dichalcogenides as Nanocarriers To Enhance and Stabilize Enzyme Activity for Electrochemical Pesticide Detection. *ACS Nano* 11, 5774-5784 (2017). https://doi.org/10.1021/acsnano.7b01364
- 52 Tao, L. et al. 1T' Transition Metal Telluride Atomic Layers for Plasmon-Free SERS at Femtomolar Levels. J. Am. Chem. Soc. 140, 8696-8704 (2018). https://doi.org/10.1021/jacs.8b02972
- 53 Kappera, R. *et al.* Phase-engineered low-resistance contacts for ultrathin MoS₂ transistors. *Nat. Mater.* **13**, 1128-1134 (2014). https://doi.org/10.1038/nmat4080
- 54 Cheng, Z. F. *et al.* Improving electron mobility in MoS2 field-effect transistors by optimizing the interface contact and enhancing the channel conductance through local structural phase transition. *J. Mater. Chem. C* 12, 2794-2802 (2024).



https://doi.org/10.1039/d3tc04605b

- 55 Gong, M. Y. *et al.* Unraveling the Role of Interfacial Interactions in Electrical Contacts of Atomically Thin Transition-Metal Dichalcogenides. *ACS Nano* **19**, 4718-4730 (2025). https://doi.org/10.1021/acsnano.4c15341
- 56 Khaustov, V. O. *et al.* Heterocontact-Triggered 1H to 1T' Phase Transition in CVD-Grown Monolayer MoTe2: Implications for Low Contact Resistance Electronic Devices. *ACS Appl. Nano Mater.* 7, 18094-18105 (2023). https://doi.org/10.1021/acsanm.3c01314
- 57 Li, H. *et al.* Ideal electrodes for monolayer boron phosphide and their device performance. *Appl. Surf. Sci.* **655**, 9 (2024). https://doi.org/10.1016/j.apsusc.2024.159525
 58 Okada, M. *et al.* Large-Scale 1T'-Phase Tungsten Disulfide Atomic Layers Grown by Gas-Source Chemical Vapor Deposition. *ACS Nano* **16**, 13069-13081 (2022). https://doi.org/10.1021/acsnano.2c05699
- 59 Liu, L. N. *et al.* Phase-selective synthesis of 1T' MoS₂ monolayers and heterophase bilayers. *Nat. Mater.* **17**, 1108-+ (2018). https://doi.org/10.1038/s41563-018-0187-1
- 60 Qi, Y. P. *et al.* Superconductivity in Weyl semimetal candidate MoTe₂. *Nat. Commun.* 7, 7 (2016). https://doi.org/10.1038/ncomms11038
- 61 Zhang, F. *et al.* Electric-field induced structural transition in vertical MoTe₂- and Mo_{1-x}W_xTe₂-based resistive memories. *Nat. Mater.* **18**, 55-+ (2019). https://doi.org/10.1038/s41563-018-0234-y
- 62 Wypych, F. & Schollhorn, R. 1T-MoS₂, A NEW METALLIC MODIFICATION OF MOLYBDENUM-DISULFIDE. *J. Chem. Soc.-Chem. Commun.*, 1386-1388 (1992). https://doi.org/10.1039/c39920001386
- 63 Voiry, D., Mohite, A. & Chhowalla, M. Phase engineering of transition metal dichalcogenides. *Chem. Soc. Rev.* **44**, 2702-2712 (2015). https://doi.org/10.1039/c5cs00151j 64 Joseph, S. *et al.* A review of the synthesis, properties, and applications of 2D transition



- metal dichalcogenides and their heterostructures. *Mater. Chem. Phys.* **297**, 17 (2023). https://doi.org/10.1016/j.matchemphys.2023.127332
- 65 Li, J. L., Liu, X. X., Feng, Y. & Yin, J. H. Recent progress in polymer/two-dimensional nanosheets composites with novel performances. *Prog. Polym. Sci.* **126**, 51 (2022). https://doi.org/10.1016/j.progpolymsci.2022.101505
- 66 Mondal, A. & Vomiero, A. 2D Transition Metal Dichalcogenides-Based Electrocatalysts for Hydrogen Evolution Reaction. *Adv. Funct. Mater.* **32**, 28 (2022). https://doi.org/10.1002/adfm.202208994
- 67 Regan, E. C. *et al.* Emerging exciton physics in transition metal dichalcogenide heterobilayers. *Nat. Rev. Mater.* 7, 778-795 (2022). https://doi.org/10.1038/s41578-022-00440-1
- 68 Wang, X. *et al.* Vacancy Defects in 2D Transition Metal Dichalcogenide Electrocatalysts: From Aggregated to Atomic Configuration. *Adv. Mater.* **35**, 47 (2023). https://doi.org/10.1002/adma.202206576
- 69 Wang, X. *et al.* Single-Atom Engineering to Ignite 2D Transition Metal Dichalcogenide Based Catalysis: Fundamentals, Progress, and Beyond. *Chem. Rev.* **122**, 1273-1348 (2022). https://doi.org/10.1021/acs.chemrev.1c00505
- 70 Yang, R. J. et al. 2D Transition Metal Dichalcogenides for Photocatalysis. *Angew. Chem.-Int. Edit.* **62**, 29 (2023). https://doi.org/10.1002/anie.202218016
- 71 Yuan, D. *et al.* Atomically Thin Materials for Next-Generation Rechargeable Batteries. *Chem. Rev.* **122**, 957-999 (2022). https://doi.org/10.1021/acs.chemrev.1c00636
- 72 Sokolikova, M. S. & Mattevi, C. Direct synthesis of metastable phases of 2D transition metal dichalcogenides. *Chem. Soc. Rev.* **49**, 3952-3980 (2020). https://doi.org/10.1039/d0cs00143k
- 73 Jin, M. J. *et al.* Boosting Charge Transport and Catalytic Performance in MoS2 by Zn2+ Intercalation Engineering for Lithium-Sulfur Batteries. *ACS Nano* **18**, 2017-2029



(2024). https://doi.org/10.1021/acsnano.3c08395

- 74 Kirubasankar, B. *et al.* Atomic and structural modifications of two-dimensional transition metal dichalcogenides for various advanced applications. *Chem. Sci.* **13**, 7707-7738 (2022). https://doi.org/10.1039/d2sc01398c
- 75 Kwon, I. S. *et al.* MoSe₂-VSe₂-NbSe₂ Ternary Alloy Nanosheets to Boost Electrocatalytic Hydrogen Evolution Reaction. *Adv. Mater.* **34**, 9 (2022). https://doi.org/10.1002/adma.202205524
- 76 Li, Z. J. *et al.* 1T' -transition metal dichalcogenide monolayers stabilized on 4H-Au nanowires for ultrasensitive SERS detection. *Nat. Mater.* **23**, 18 (2024). https://doi.org/10.1038/s41563-024-01860-w
- 77 Liu, Z. Q. *et al.* General Bottom-Up Colloidal Synthesis of Nano-MonolayerTransition-Metal Dichalcogenides with High 1T'-Phase Purity. *J. Am. Chem. Soc.* **144**, 4863-4873 (2022). https://doi.org/10.1021/jacs.1c12379
- 78 Lai, Z. C. *et al.* Metastable 1T' -phase group VIB transition metal dichalcogenide crystals. *Nat. Mater.* **20**, 1113-+ (2021). https://doi.org/10.1038/s41563-021-00971-y
- 79 Cho, S. H. Y. *et al.* Direct Observation of the Topological Surface State in the Topological Superconductor 2M-WS2. *Nano Lett.* **22**, 8827-8834 (2022). https://doi.org/10.1021/acs.nanolett.2c02372
- 80 Dong, Q. *et al.* Record-High Superconductivity in Transition Metal Dichalcogenides Emerged in Compressed 2H-TaS2. *Adv. Mater.* **34**, 7 (2022). https://doi.org/10.1002/adma.202103168
- 81 Martins, L. G. P. *et al.* Electronic Band Tuning and Multivalley Raman Scattering in Monolayer Transition Metal Dichalcogenides at High Pressures. *ACS Nano* **16**, 8064-8075 (2022). https://doi.org/10.1021/acsnano.2c01065
- 82 Tian, C. *et al.* Dimensionality switching and superconductivity transition in dense 1T-HfSe2. *Phys. Rev. B* **105**, 6 (2022). https://doi.org/10.1103/PhysRevB.105.L180506



- 83 Wang, X. R. *et al.* Interfacial ferroelectricity in rhombohedral-stacked bilayer transition metal dichalcogenides. *Nat. Nanotechnol.* 17, 367-+ (2022). https://doi.org/10.1038/s41565-021-01059-z
- 84 Cho, S. *et al.* Phase patterning for ohmic homojunction contact in MoTe₂. *Science* **349**, 625-628 (2015). https://doi.org/10.1126/science.aab3175
- 85 An, K. Y. *et al.* Wafer-Scale 2H-MoS2 Monolayer for High Surface-enhanced Raman Scattering Performance: Charge-Transfer Coupled with Molecule Resonance. *Adv. Mater. Technol.* 7, 8 (2022). https://doi.org/10.1002/admt.202200217
- 86 Chen, Y., Hu, Y. L. & Li, G. K. A Review on Non-Noble Metal Substrates for Surface-Enhanced Raman Scattering Detection. *Chemosensors* 11, 22 (2023). https://doi.org/10.3390/chemosensors11080427
- 87 Ekoya, B. G. M. *et al.* 2H Tantalum Disulfide Nanosheets as Substrates for Ultrasensitive SERS-Based Sensing. *ACS Appl. Nano Mater.* **5**, 8 (2022). https://doi.org/10.1021/acsanm.2c01105
- 88 Tang, X. *et al.* Exploring and Engineering 2D Transition Metal Dichalcogenides toward Ultimate SERS Performance. *Adv. Mater.* **36**, 22 (2024). https://doi.org/10.1002/adma.202312348
- 89 You, Q. Z. *et al.* Resonance Photoluminescence Enhancement of Monolayer MoS2 via a Plasmonic Nanowire Dimer Optical Antenna. *ACS Appl. Mater. Interfaces* **14**, 23756-23764 (2022). https://doi.org/10.1021/acsami.2c02684
- 90 Li, Y. H. *et al.* Piezoelectric 1T Phase MoSe₂ Nanoflowers and Crystallographically Textured Electrodes for Enhanced Low-Temperature Zinc-Ion Storage. *Adv. Mater.* **35**, 15 (2023). https://doi.org/10.1002/adma.202208615
- 91 Aghamohammadi, H., Eslami-Farsani, R. & Castillo-Martinez, E. Recent trends in the development of MXenes and MXene-based composites as anode materials for Li-ion batteries. *J. Energy Storage* 47, 32 (2022). https://doi.org/10.1016/j.est.2021.103572



- 92 Ali, M. *et al.* 2D-TMDs based electrode material for supercapacitor applications. *Int. J. Energy Res.* **46**, 22336-22364 (2022). https://doi.org/10.1002/er.8698
- 93 Kumar, Y. R., Deshmukh, K., Kovárík, T. & Pasha, S. K. K. A systematic review on 2D materials for volatile organic compound sensing. *Coord. Chem. Rev.* **461**, 58 (2022). https://doi.org/10.1016/j.ccr.2022.214502
- 94 Sahoo, B. B. *et al.* A state-of-art review on 2D material-boosted metal oxide nanoparticle electrodes: Supercapacitor applications. *J. Energy Storage* **65**, 18 (2023). https://doi.org/10.1016/j.est.2023.107335
- 95 Yun, Q. B. *et al.* Recent Progress on Phase Engineering of Nanomaterials. *Chem. Rev.* **123**, 13489-13692 (2023). https://doi.org/10.1021/acs.chemrev.3c00459
- 96 Tan, C. L. *et al.* Preparation of High-Percentage 1T-Phase Transition Metal Dichalcogenide Nanodots for Electrochemical Hydrogen Evolution. *Adv. Mater.* **30**, 9 (2018). https://doi.org/10.1002/adma.201705509
- 97 Chang, K. et al. Targeted Synthesis of 2H-and 1T-Phase MoS₂ Monolayers for Catalytic Hydrogen Evolution. Adv. Mater. **28**, 10033-10041 (2016). https://doi.org/10.1002/adma.201603765
- 98 Zhu, J. D. *et al.* Ion Gated Synaptic Transistors Based on 2D van der Waals Crystals with Tunable Diffusive Dynamics. *Adv. Mater.* **30**, 11 (2018). https://doi.org/10.1002/adma.201800195
- 99 Zhu, X. J., Li, D., Liang, X. G. & Lu, W. D. Ionic modulation and ionic coupling effects in MoS₂ devices for neuromorphic computing. *Nat. Mater.* **18**, 141-148 (2019). https://doi.org/10.1038/s41563-018-0248-5
- 100 Chen, J. *et al.* Performance Limits and Advancements in Single 2D Transition Metal Dichalcogenide Transistor. *Nano-Micro Lett.* **16**, 55 (2024). https://doi.org/10.1007/s40820-024-01461-x
- 101 Khan, R. et al. 2D MoTe2 memristors for energy-efficient artificial synapses and



neuromorphic applications. *Nanoscale* **17**, 13174-13206 (2025). https://doi.org/10.1039/d5nr01509j

102 Kwon, M. J. *et al.* Optoelectronic Synapse Behaviors of HfS2 Grown via Molten Salt Flux Method. *Electron. Mater. Lett.* **20**, 559-570 (2024). https://doi.org/10.1007/s13391-024-00494-z

103 Li, S. Y. *et al.* In-sensor neuromorphic computing using perovskites and transition metal dichalcogenides. *J. Phys-Mater.* 7, 33 (2024). https://doi.org/10.1088/2515-7639/ad5251

104 Obaidulla, S. M., Supina, A., Kamal, S., Khan, Y. & Kralj, M. van der Waals 2D transition metal dichalcogenide/organic hybridized heterostructures: recent breakthroughs and emerging prospects of the device. *Nanoscale Horiz.* **9**, 44-92 (2023). https://doi.org/10.1039/d3nh00310h

105 Ren, J. W., Shen, H. Z., Liu, Z. Y., Xu, M. & Li, D. H. Artificial Synapses Based on WSe2 Homojunction via Vacancy Migration. *ACS Appl. Mater. Interfaces* **14**, 21141-21149 (2022). https://doi.org/10.1021/acsami.2c01162

106 Zou, T. Y., Jiang, C. P., Xu, W. T. & Noh, Y. Y. Neuromorphic Device Based on Solution-Processed WSe2 Nanoflake Synaptic Transistors. *IEEE Electron Device Lett.* **46**, 765-768 (2025). https://doi.org/10.1109/led.2025.3554009

107 Sun, L. F. *et al.* Layer-Dependent Chemically Induced Phase Transition of Two-Dimensional MoS₂. *Nano Lett.* **18**, 3435-3440 (2018). https://doi.org/10.1021/acs.nanolett.8b00452

108 Li, Y., Duerloo, K. A. N., Wauson, K. & Reed, E. J. Structural semiconductor-to-semimetal phase transition in two-dimensional materials induced by electrostatic gating. *Nat. Commun.* 7, 8 (2016). https://doi.org/10.1038/ncomms10671

109 Wang, Z. Q. *et al.* Synthesizing 1T-1H Two-Phase Mo_{1-x}W_xS₂ Monolayers by Chemical Vapor Deposition. *ACS Nano* **12**, 1571-1579 (2018).



https://doi.org/10.1021/acsnano.7b08149

- 110 Sokolikova, M. S., Sherrell, P. C., Palczynski, P., Bemmer, V. L. & Mattevi, C. Direct solution-phase synthesis of 1T ' WSe₂ nanosheets. *Nat. Commun.* **10**, 8 (2019). https://doi.org/10.1038/s41467-019-08594-3
- 111 Kwon, I. S. *et al.* 2H-2M Phase Control of WSe₂ Nanosheets by Se Enrichment Toward Enhanced Electrocatalytic Hydrogen Evolution Reaction. *Adv. Mater.*, 11 (2023). https://doi.org/10.1002/adma.202307867
- 112 Li, X. T. *et al.* Pseudo metallic (1T) molybdenum disulfide for efficient photo/electrocatalytic water splitting. *Appl. Catal. B-Environ.* **307**, 12 (2022). https://doi.org/10.1016/j.apcatb.2022.121156
- 113 Sun, L. *et al.* 1T-Phase Enriched P doped WS₂ nanosphere for highly efficient electrochemical hydrogen evolution reaction. *Chem. Eng. J.* **429**, 9 (2022). https://doi.org/10.1016/j.cej.2021.132187
- 114 Wypych, F., Solenthaler, C., Prins, R. & Weber, T. Electron diffraction study of intercalation compounds derived from 1T-MoS₂. *J. Solid State Chem.* **144**, 430-436 (1999). https://doi.org/10.1006/jssc.1999.8193
- 115 Yu, Y. F. *et al.* High phase-purity 1T'-MoS₂- and 1T'-MoSe₂- layered crystals. *Nat. Chem.* **10**, 638-643 (2018). https://doi.org/10.1038/s41557-018-0035-6
- 116 Guo, C. G. *et al.* High-quality single-layer nanosheets of MS₂ (M = Mo, Nb, Ta, Ti) directly exfoliated from AMS₂ (A = Li, Na, K) crystals. *J. Mater. Chem. C* 5, 5977-5983 (2017). https://doi.org/10.1039/c7tc00838d
- 117 Benavente, E., Santa Ana, M. A., Mendizábal, F. & González, G. Intercalation chemistry of molybdenum disulfide. *Coord. Chem. Rev.* **224**, 87-109 (2002). https://doi.org/10.1016/s0010-8545(01)00392-7
- 118 Dungey, K. E., Curtis, M. D. & Penner-Hahn, J. E. Structural characterization and thermal stability of MoS₂ intercalation compounds. *Chem. Mat.* **10**, 2152-2161 (1998).



https://doi.org/10.1021/cm980034u

- 119 Liu, F. *et al.* Phase Engineering and Alkali Cation Stabilization for 1T Molybdenum Dichalcogenides Monolayers. *Adv. Funct. Mater.* **32**, 13 (2022). https://doi.org/10.1002/adfm.202204601
- 120 Park, S. *et al.* Phase Engineering of Transition Metal Dichalcogenides with Unprecedentedly High Phase Purity, Stability, and Scalability via Molten-Metal-Assisted Intercalation. *Adv. Mater.* **32**, 11 (2020). https://doi.org/10.1002/adma.202001889
- 121 Zhang, R. Y. *et al.* Superconductivity in Potassium-Doped Metallic Polymorphs of MoS₂. *Nano Lett.* **16**, 629-636 (2016). https://doi.org/10.1021/acs.nanolett.5b04361
- 122 Park, S. *et al.* Phase Engineering of Transition Metal Dichalcogenides with Unprecedentedly High Phase Purity, Stability, and Scalability via Molten-Metal-Assisted Intercalation. *Adv. Mater.* **32** (2020). https://doi.org/10.1002/adma.202001889
- 123 Tan, S. J. R. *et al.* Chemical Stabilization of 1T ' Phase Transition Metal Dichalcogenides with Giant Optical Kerr Nonlinearity. *J. Am. Chem. Soc.* **139**, 2504-2511 (2017). https://doi.org/10.1021/jacs.6b13238
- 124 Lin, L. X. *et al.* Engineered 2D Transition Metal Dichalcogenides-A Vision of Viable Hydrogen Evolution Reaction Catalysis. *Adv. Energy Mater.* **10**, 24 (2020). https://doi.org/10.1002/aenm.201903870
- 125 Duerloo, K. A. N., Li, Y. & Reed, E. J. Structural phase transitions in two-dimensional Mo- and W-dichalcogenide monolayers. *Nat. Commun.* 5, 9 (2014). https://doi.org/10.1038/ncomms5214
- 126 Nayak, A. P. *et al.* Pressure-induced semiconducting to metallic transition in multilayered molybdenum disulphide. *Nat. Commun.* **5**, 9 (2014). https://doi.org/10.1038/ncomms4731
- 127 Suzuki, R. *et al.* Valley-dependent spin polarization in bulk MoS₂ with broken inversion symmetry. *Nat. Nanotechnol.* **9**, 611-617 (2014). https://doi.org/10.1038/nnano.2014.148



- 128 Shi, J. et al. 3R MoS₂ with Broken Inversion Symmetry: A Promising Ultrathin Nonlinear Optical Device. Adv. Mater. 29, 9 (2017). https://doi.org/10.1002/adma.201701486
- 129 Zeng, Z. X. S. *et al.* Controlled Vapor Growth and Nonlinear Optical Applications of Large-Area 3R Phase WS₂ and WSe₂ Atomic Layers. *Adv. Funct. Mater.* **29**, 8 (2019). https://doi.org/10.1002/adfm.201806874
- 130 Lin, Y. C., Dumcencon, D. O., Huang, Y. S. & Suenaga, K. Atomic mechanism of the semiconducting-to-metallic phase transition in single-layered MoS₂. *Nat. Nanotechnol.* **9**, 391-396 (2014). https://doi.org/10.1038/nnano.2014.64
- 131 Singh, A., Shirodkar, S. N. & Waghmare, U. V. 1H and 1T polymorphs, structural transitions and anomalous properties of (Mo,W)(S,Se)₂ monolayers: first-principles analysis. 2D Mater. **2**, 12 (2015). https://doi.org/10.1088/2053-1583/2/3/035013
- 132 Bruyer, E. *et al.* Possibility of combining ferroelectricity and Rashba-like spin splitting in monolayers of the 1T-type transition-metal dichalcogenides MX₂ (M = Mo, W; X = S, Se, Te). *Phys. Rev. B* **94**, 6 (2016). https://doi.org/10.1103/PhysRevB.94.195402
- 133 Park, J. C. *et al.* Phase-Engineered Synthesis of Centimeter-Scale 1T ' and 2H-Molybdenum Ditelluride Thin Films. *ACS Nano* **9**, 6548-6554 (2015). https://doi.org/10.1021/acsnano.5b02511
- 134 Sandoval, S. J., Yang, D., Frindt, R. F. & Irwin, J. C. RAMAN-STUDY AND LATTICE-DYNAMICS OF SINGLE MOLECULAR LAYERS OF MOS₂. *Phys. Rev. B* 44, 3955-3962 (1991). https://doi.org/10.1103/PhysRevB.44.3955
- 135 Eda, G. *et al.* Coherent Atomic and Electronic Heterostructures of Single-Layer MoS₂. *ACS Nano* **6**, 7311-7317 (2012). https://doi.org/10.1021/nn302422x
- 136 Qian, X. F., Liu, J. W., Fu, L. & Li, J. Quantum spin Hall effect in two-dimensional transition metal dichalcogenides. *Science* **346**, 1344-1347 (2014). https://doi.org/10.1126/science.1256815



- 137 Kadantsev, E. S. & Hawrylak, P. Electronic structure of a single MoS₂ monolayer. *Solid State Commun.* **152**, 909-913 (2012). https://doi.org/10.1016/j.ssc.2012.02.005
- 138 Hu, T., Li, R. & Dong, J. M. A new (2 x 1) dimerized structure of monolayer 1T-molybdenum disulfide, studied from first principles calculations. *J. Chem. Phys.* **139**, 7 (2013). https://doi.org/10.1063/1.4827082
- 139 Wang, H. *et al.* Integrated Circuits Based on Bilayer MoS₂ Transistors. *Nano Lett.* **12**, 4674-4680 (2012). https://doi.org/10.1021/nl302015v
- 140 Yu, W. J. *et al.* Vertically stacked multi-heterostructures of layered materials for logic transistors and complementary inverters. *Nat. Mater.* **12**, 246-252 (2013). https://doi.org/10.1038/nmat3518
- 141 Wachter, S., Polyushkin, D. K., Bethge, O. & Mueller, T. A microprocessor based on a two-dimensional semiconductor. *Nat. Commun.* **8**, 6 (2017). https://doi.org/10.1038/ncomms14948
- 142 Marin, J. F. G., Unuchek, D., Watanabe, K., Taniguchi, T. & Kis, A. MoS₂ photodetectors integrated with photonic circuits. *Npj 2d Materials and Applications* **3** (2019). https://doi.org/10.1038/s41699-019-0096-4
- 143 Peyskens, F., Chakraborty, C., Muneeb, M., Van Thourhout, D. & Englund, D. Integration of single photon emitters in 2D layered materials with a silicon nitride photonic chip. *Nat. Commun.* **10** (2019). https://doi.org/10.1038/s41467-019-12421-0
- 144 Goossens, S. *et al.* Broadband image sensor array based on graphene-CMOS integration. *Nature Photonics* **11**, 366-371 (2017). https://doi.org/10.1038/nphoton.2017.75
- 145 Mennel, L. *et al.* Ultrafast machine vision with 2D material neural network image sensors. *Nature* **579**, 62-+ (2020). https://doi.org/10.1038/s41586-020-2038-x
- 146 Kamarauskas, M. *et al.* Photovoltaic effect-driven IR response of heterojunctions obtained by direct CVD synthesis of MoS₂ nanolayers on crystalline silicon. *Nanotechnology* **31** (2020). https://doi.org/10.1088/1361-6528/ab98c0



147 Velusamy, D. B. *et al.* MXenes for Plasmonic Photodetection. *Adv. Mater.* **31** (2019). https://doi.org/10.1002/adma.201807658

148 Lai, Z. C. *et al.* Salt-Assisted 2H-to-1T ' Phase Transformation of Transition Metal Dichalcogenides. *Adv. Mater.* **34**, 7 (2022). https://doi.org/10.1002/adma.202201194
149 Whittingham, M. S. CHEMISTRY OF INTERCALATION COMPOUNDS - METAL GUESTS IN CHALCOGENIDE HOSTS. *Prog. Solid State Chem.* **12**, 41-99 (1978). https://doi.org/10.1016/0079-6786(78)90003-1

150 Ma, Y. G. *et al.* Reversible Semiconducting-to-Metallic Phase Transition in Chemical Vapor Deposition Grown Mono layer WSe₂ and Applications for Devices. *ACS Nano* **9**, 7383-7391 (2015). https://doi.org/10.1021/acsnano.5b02399

151 Zeng, Z. Y. *et al.* Single-Layer Semiconducting Nanosheets: High-Yield Preparation and Device Fabrication. *Angew. Chem.-Int. Edit.* **50**, 11093-11097 (2011). https://doi.org/10.1002/anie.201106004

152 Schollhorn, R. & Lerf, A. REDOX REACTIONS OF LAYERED TRANSITION-METAL DISULFIDES IN ALKALI-HALIDE MELTS. *Journal of the Less-Common Metals* **42**, 89-100 (1975). https://doi.org/10.1016/0022-5088(75)90023-5

153 Kim, S. *et al.* Long-Range Lattice Engineering of MoTe₂ by a 2D Electride. *Nano Lett.* 17, 3363-3368 (2017). https://doi.org/10.1021/acs.nanolett.6b05199

154 Cordovan, A., Blanchard, P., Lancelot, C., Fremy, G. & Lamonier, C. Probing the Nature of the Active Phase of Molybdenum-Supported Catalysts for the Direct Synthesis of Methylmercaptan from Syngas and H₂S. *ACS Catal.* **5**, 2966-2981 (2015). https://doi.org/10.1021/cs502031f

155 Wang, Z. Y., Li, R. L., Su, C. L. & Loh, K. P. Intercalated phases of transition metal dichalcogenides. *Smartmat* 1 (2020). https://doi.org/10.1002/smm2.1013

156 Somoano, R. B., Hadek, V. & Rembaum, A. ALKALI-METAL INTERCALATES OF MOLYBDENUM DISULFIDE. *J. Chem. Phys.* **58**, 697-701 (1973).



https://doi.org/10.1063/1.1679256

157 Papageorgopoulos, C. A. & Jaegermann, W. LI INTERCALATION ACROSS AND ALONG THE VAN-DER-WAALS SURFACES OF MoS₂(0001). *Surf. Sci.* **338**, 83-93 (1995). https://doi.org/10.1016/0039-6028(95)00544-7

158Zhang, L. Z. *et al.* Metal telluride nanosheets by scalable solid lithiation and exfoliation. *Nature* **628**, 15 (2024). https://doi.org/10.1038/s41586-024-07209-2

159 Zheng, J. *et al.* High yield exfoliation of two-dimensional chalcogenides using sodium naphthalenide. *Nat. Commun.* **5**, 7 (2014). https://doi.org/10.1038/ncomms3995

160 Sun, X. L., Wang, Z. G., Li, Z. J. & Fu, Y. Q. Origin of Structural Transformation in Mono- and Bi-Layered Molybdenum Disulfide. *Sci Rep* **6**, 9 (2016). https://doi.org/10.1038/srep26666

161 Li, F. X. *et al.* In Situ Study of K⁺ Electrochemical Intercalating into MoS₂ Flakes. *J. Phys. Chem. C* **123**, 5067-5072 (2019). https://doi.org/10.1021/acs.jpcc.8b09898

162 Wang, C. *et al.* Monolayer atomic crystal molecular superlattices. *Nature* **555**, 231-+ (2018). https://doi.org/10.1038/nature25774

163 Hor, Y. S. *et al.* Superconductivity in Cu_xBi₂Se₃ and its Implications for Pairing in the Undoped Topological Insulator. *Phys. Rev. Lett.* **104**, 4 (2010). https://doi.org/10.1103/PhysRevLett.104.057001

164 Zhao, X. X. et al. Engineering covalently bonded 2D layered materials by self-intercalation. *Nature* **581**, 171-+ (2020). https://doi.org/10.1038/s41586-020-2241-9

165 Cordovan, A., Blanchard, P., Lancelot, C., Frémy, G. & Lamonier, C. Probing the Nature of the Active Phase of Molybdenum-Supported Catalysts for the Direct Synthesis of Methylmercaptan from Syngas and H₂S. *ACS Catal.* **5**, 2966-2981 (2015). https://doi.org/10.1021/cs502031f

166 Jenjeti, R. N., Kumar, R., Sellam, A. & Sampath, S. High Stability of 1T-Phase MoS_{2x}Se_{2(1-x)} Monolayers Under Ambient Conditions. *J. Phys. Chem. C* **125**, 8407-8417



(2021). https://doi.org/10.1021/acs.jpcc.1c00212

167 Cai, L. *et al.* Vacancy-Induced Ferromagnetism of MoS₂ Nanosheets. *J. Am. Chem. Soc.* **137**, 2622-2627 (2015). https://doi.org/10.1021/ja5120908

168 Liu, L. N. *et al.* Phase-selective synthesis of 1T' MoS₂ monolayers and heterophase bilayers. *Nat. Mater.* **17**, 1108-1114 (2018). https://doi.org/10.1038/s41563-018-0187-1

169 Lai, Z. C. *et al.* Salt-Assisted 2H-to-1T' Phase Transformation of Transition Metal Dichalcogenides. *Adv. Mater.* **34**, 7 (2022). https://doi.org/10.1002/adma.202201194

170 Xu, J. *et al.* Sandwiched cathodes kinetically boosted by few-layered catalytic 1T-MoSe₂ nanosheets for high-rate and long-cycling lithium-sulfur batteries. *EcoMat* **5**, 13 (2023). https://doi.org/10.1002/eom2.12329

171 Zhou, L. *et al.* Synthesis of High-Quality Large-Area Homogenous 1T' MoTe₂ from Chemical Vapor Deposition. *Adv. Mater.* **28**, 9526-+ (2016). https://doi.org/10.1002/adma.201602687

172 Fang, Y. Q. *et al.* Structure Re-determination and Superconductivity Observation of Bulk 1T MoS₂. *Angew. Chem.-Int. Edit.* **57**, 1232-1235 (2018). https://doi.org/10.1002/anie.201710512

173 Kresse, G. & Joubert, D. From ultrasoft pseudopotentials to the projector augmented-wave method. *Phys. Rev. B* **59**, 1758-1775 (1999). https://doi.org/10.1103/PhysRevB.59.1758

174 Kresse, G. & Furthmuller, J. Efficient iterative schemes for ab initio total-energy calculations using a plane-wave basis set. *Phys. Rev. B* **54**, 11169-11186 (1996). https://doi.org/10.1103/PhysRevB.54.11169

175 Perdew, J. P., Burke, K. & Ernzerhof, M. Generalized gradient approximation made simple. *Phys. Rev. Lett.* 77, 3865-3868 (1996). https://doi.org/10.1103/PhysRevLett.77.3865 176 Grimme, S., Antony, J., Ehrlich, S. & Krieg, H. A consistent and accurate ab initio parametrization of density functional dispersion correction (DFT-D) for the 94 elements



H-Pu. J. Chem. Phys. 132, 19 (2010). https://doi.org/10.1063/1.3382344

177 West, C. D. The Crystal Structures of Some Alkali Hydrosulfides and Monosulfides. *Z. Für Krist. - Cryst. Mater.* **88**, 97-115 (1934).

178 Zeng, J., Lu, M., Liu, H. W., Jiang, H. & Xie, X. C. Realistic flat-band model based on degenerate p-orbitals in two-dimensional ionic materials. *Sci. Bull.* **66**, 765-770 (2021). https://doi.org/10.1016/j.scib.2021.01.006

179 Zhang, K. L. *et al.* Molybdenum Selenide Electrocatalysts for Electrochemical Hydrogen Evolution Reaction. *ChemElectroChem* **6**, 3530-3548 (2019). https://doi.org/10.1002/celc.201900448

180 Hu, J. *et al.* Engineering stepped edge surface structures of MoS₂ sheet stacks to accelerate the hydrogen evolution reaction. *Energy Environ. Sci.* **10**, 593-603 (2017). https://doi.org/10.1039/c6ee03629e

181 Deng, S. J. *et al.* Directional Construction of Vertical Nitrogen-Doped 1T-2H MoSe₂/Graphene Shell/Core Nanoflake Arrays for Efficient Hydrogen Evolution Reaction. *Adv. Mater.* **29**, 8 (2017). https://doi.org/10.1002/adma.201700748

182 Voiry, D. *et al.* Enhanced catalytic activity in strained chemically exfoliated WS₂ nanosheets for hydrogen evolution. *Nat. Mater.* **12**, 850-855 (2013). https://doi.org/10.1038/nmat3700

183 Liu, Z. Q. *et al.* Colloidal synthesis of 1T' phase dominated WS₂ towards endurable electrocatalysis. *Nano Energy* **50**, 176-181 (2018). https://doi.org/10.1016/j.nanoen.2018.05.019

184 Dong, G. F. *et al.* Insight into the electrochemical activation of carbon-based cathodes for hydrogen evolution reaction. *J. Mater. Chem. A* **3**, 13080-13086 (2015). https://doi.org/10.1039/c5ta02551f

185 Ji, S. G., Kim, H., Park, C., Kim, W. & Choi, C. H. Underestimation of Platinum Electrocatalysis Induced by Carbon Monoxide Evolved from Graphite Counter Electrodes.



ACS Catal. 10, 10773-10783 (2020). https://doi.org/10.1021/acscatal.0c01783

186 Wang, H. T. *et al.* Electrochemical tuning of vertically aligned MoS₂ nanofilms and its application in improving hydrogen evolution reaction. *Proc. Natl. Acad. Sci. U. S. A.* **110**, 19701-19706 (2013). https://doi.org/10.1073/pnas.1316792110

187 Voiry, D. *et al.* Conducting MoS₂ Nanosheets as Catalysts for Hydrogen Evolution Reaction. *Nano Lett.* **13**, 6222-6227 (2013). https://doi.org/10.1021/nl403661s

188 Voiry, D. *et al.* The role of electronic coupling between substrate and 2D MoS₂ nanosheets in electrocatalytic production of hydrogen. *Nat. Mater.* **15**, 1003-1009 (2016). https://doi.org/10.1038/nmat4660

189 Chen, W. S. *et al.* Quantum Dots of 1T Phase Transitional Metal Dichalcogenides Generated via Electrochemical Li Intercalation. *ACS Nano* **12**, 308-316 (2018). https://doi.org/10.1021/acsnano.7b06364

190 Li, B. J. *et al.* Engineering Single-Layer Hollow Structure of Transition Metal Dichalcogenides with High 1T-Phase Purity for Hydrogen Evolution Reaction. *Adv. Mater.*, 10 (2023). https://doi.org/10.1002/adma.202303285

191 Wang, L. L. *et al.* Enhancing catalytic activity of tungsten disulfide through topology. *Appl. Catal. B-Environ.* **256**, 7 (2019). https://doi.org/10.1016/j.apcatb.2019.117802

192 Tian, J. Q., Liu, Q., Asiri, A. M. & Sun, X. P. Self-Supported Nanoporous Cobalt Phosphide Nanowire Arrays: An Efficient 3D Hydrogen-Evolving Cathode over the Wide Range of pH 0-14. *J. Am. Chem. Soc.* **136**, 7587-7590 (2014). https://doi.org/10.1021/ja503372r

193 Jiang, P. *et al.* A Cost-Effective 3D Hydrogen Evolution Cathode with High Catalytic Activity: FeP Nanowire Array as the Active Phase. *Angew. Chem.-Int. Edit.* **53**, 12855-12859 (2014). https://doi.org/10.1002/anie.201406848

194 Tang, C. *et al.* Ternary Fe_xCo_{1-x}P Nanowire Array as a Robust Hydrogen Evolution Reaction Electrocatalyst with Pt-like Activity: Experimental and Theoretical Insight. *Nano*



Lett. 16, 6617-6621 (2016). https://doi.org/10.1021/acs.nanolett.6b03332

195 Mao, S. *et al.* Perpendicularly Oriented MoSe₂/Graphene Nanosheets as Advanced Electrocatalysts for Hydrogen Evolution. *Small* 11, 414-419 (2015). https://doi.org/10.1002/smll.201401598

196 Faber, M. S. *et al.* High-Performance Electrocatalysis Using Metallic Cobalt Pyrite (CoS₂) Micro- and Nanostructures. *J. Am. Chem. Soc.* **136**, 10053-10061 (2014). https://doi.org/10.1021/ja504099w

197 Kibsgaard, J. & Jaramillo, T. F. Molybdenum Phosphosulfide: An Active, Acid-Stable, Earth-Abundant Catalyst for the Hydrogen Evolution Reaction. *Angew. Chem.-Int. Edit.* **53**, 14433-14437 (2014). https://doi.org/10.1002/anie.201408222

198 Song, B. *et al.* Tuning Mixed Nickel Iron Phosphosulfide Nanosheet Electrocatalysts for Enhanced Hydrogen and Oxygen Evolution. *ACS Catal.* 7, 8549-8557 (2017). https://doi.org/10.1021/acscatal.7b02575

199 Zhang, H. B. *et al.* Active Sites Implanted Carbon Cages in Core Shell Architecture: Highly Active and Durable Electrocatalyst for Hydrogen Evolution Reaction. *ACS Nano* **10**, 684-694 (2016). https://doi.org/10.1021/acsnano.5b05728

200 Qiu, Z., Tai, C. W., Niklasson, G. A. & Edvinsson, T. Direct observation of active catalyst surface phases and the effect of dynamic self-optimization in NiFe-layered double hydroxides for alkaline water splitting. *Energy Environ. Sci.* **12**, 572-581 (2019). https://doi.org/10.1039/c8ee03282c

201 Doan, T. L. L. *et al.* Advanced Mott-Schottky heterojunction of semi-conductive MoS₂ nanoparticles/metallic CoS₂ nanotubes as an efficient multifunctional catalyst for urea-water electrolysis. *Appl. Catal. B-Environ. Energy* **342**, 17 (2024). https://doi.org/10.1016/j.apcatb.2023.123295

202 Liu, Q. M. et al. Ultrafast synthesis of amorphous molybdenum sulfide by magnetic induction heating for hydrogen evolution reaction. Appl. Catal. B-Environ. Energy 342, 11



(2024). https://doi.org/10.1016/j.apcatb.2023.123399

203 Nivetha, R. *et al.* Highly Immobilized Bimetallic Fe/M-N₄ (M- Mg or Zn) Conductive Metal-Organic Frameworks on Nitrogen-Doped Porous Carbon for Efficient Electrocatalytic Hydrogen Evolution and Oxygen Reduction Reactions. *Small Struct.*, 14 (2023). https://doi.org/10.1002/sstr.202300355

204 Sun, J. P., Qin, S. Y., Zhao, Z., Zhang, Z. S. & Meng, X. C. Rapid carbothermal shocking fabrication of iron-incorporated molybdenum oxide with heterogeneous spin states for enhanced overall water/seawater splitting. *Mater. Horizons*, 13 (2023). https://doi.org/10.1039/d3mh01757e

205 Cao, X. F. *et al.* Interfacial Electron Potential Well Facilitates the Design of Cobalt Phosphide Heterojunctions for Hydrogen Evolution. *Small*, 9 (2023). https://doi.org/10.1002/smll.202306113

206 Yang, Y. F. *et al.* Hierarchical Ohmic Contact Interface Engineering for Efficient Hydrazine-Assisted Hydrogen Evolution Reaction. *Adv. Mater.*, 12 (2023). https://doi.org/10.1002/adma.202307979

207 Peled, E., Gorenshtein, A., Segal, M. & Sternberg, Y. RECHARGEABLE LITHIUM SULFUR BATTERY. *J. Power Sources* **26**, 269-271 (1989). https://doi.org/10.1016/0378-7753(89)80133-8

208 Bhargav, A., He, J. R., Gupta, A. & Manthiram, A. Lithium-Sulfur Batteries: Attaining the Critical Metrics. *Joule* 4, 285-291 (2020). https://doi.org/10.1016/j.joule.2020.01.001 209 Liu, Y. T., Liu, S., Li, G. R. & Gao, X. P. Strategy of Enhancing the Volumetric Energy Density for Lithium-Sulfur Batteries. *Adv. Mater.* 33, 23 (2021). https://doi.org/10.1002/adma.202003955

210 Zhao, C. *et al.* A high-energy and long-cycling lithium-sulfur pouch cell via a macroporous catalytic cathode with double-end binding sites. *Nat. Nanotechnol.* **16**, 166-+ (2021). https://doi.org/10.1038/s41565-020-00797-w



211 Pang, Q., Liang, X., Kwok, C. Y. & Nazar, L. F. Advances in lithium-sulfur batteries based on multifunctional cathodes and electrolytes. *Nat. Energy* **1**, 11 (2016). https://doi.org/10.1038/nenergy.2016.132

212 Li, Z. N. *et al.* Lithiated metallic molybdenum disulfide nanosheets for high-performance lithium-sulfur batteries. *Nat. Energy* **8**, 84-93 (2023). https://doi.org/10.1038/s41560-022-01175-7